Characterization of the infection process in rice bacterial blight by *Xanthomonas oryzae pv. oryzae*

Inaugural-Dissertation

zur Erlangung des Doktorgrades
der Mathematisch-Naturwissenschaftlichen Fakultät
der Heinrich-Heine-Universität Düsseldorf

vorgelegt von

M.Sc. Nora Rachel Zöllner
aus Ahlen

Düsseldorf, September 2025

aus dem Institut für Molekulare Physiologie
der Heinrich-Heine-Universität Düsseldorf

Gedruckt mit der Genehmigung der
Mathematisch-Naturwissenschaftlichen Fakultät der
Heinrich-Heine-Universität Düsseldorf

Berichterstatter:
1. Prof. Dr. Wolf B. Frommer
2. Prof. Dr. Michael Feldbrügge
3. Prof. Dr. Scott C. Peck

Tag der mündlichen Prüfung: 2. April 2026

A Word of Gratitude

I completed this doctoral thesis as part of my work at the Institute for Molecular Physiology, Heinrich Heine University Düsseldorf. I would like to express my sincere gratitude to Professor Dr. Wolf Frommer. He gave me the opportunity to join the project and work in his group. I thank him for his trust in me and for allowing me the freedom to express my scientific creativity. His guidance and encouragement have shaped my professional and personal development tremendously.

I would also like to thank Professor Dr. Michael Feldbrügge for supervising my thesis, not only as a TAC member but also as spokesperson of the collaborative research consortium MibiNet. In this context, I would like to thank the DFG for financing and enabling my doctoral studies. My thanks also go to all the partners in MibiNet, especially Jacob Sharkey, for hi excellent cooperation within the CRC. Together, we successfully completed several conferences, project meetings, and retreats.

I am deeply grateful to Dr. Eliza Loo for her excellent guidance on my projects, as well as for the open and inspiring scientific discussions and journal clubs.

I would like to thank my colleagues in the working group for being part of this journey with me. Special thanks go to Susanne Paradies for her wonderful and loyal companionship. We experienced more than most together, but you taught me how to shake it off, and somehow, we always made it through. Your resilience is a lesson I will carry forward. Thanks also to Anastaija Plett, Diana Weidauer, Hiroko Saito, Laura Redzich, Michael Wudick, and Nicoline Gappel-Schmidt. You have gone from being colleagues to friends. I have deep respect and heartfelt gratitude for what it means to do this work.

Along with all those who have encouraged and accompanied me, my gratitude is also directed to my family. My parents have always stood by me unconditionally. They have had my back and been there through thick and thin. My grandmother has always welcomed me with open arms and an open door. My sisters never cared about science, only about me. When the monsters turned into trees, I was looking at all of you.

To my partner, Leonhardt: thank you for convincing me that none of it was accidental and for being there through all of it, even from hotel rooms and office desks far away. From the early days in the golden cage to the fences in botanical gardens, you were there. When I moved on, you followed. Can I go where you go? Yes, you did. Your partnership anchored me in ways that words cannot fully express. Thank you.

Abstract

Bacterial blight (BB) of rice, caused by the bacterium *Xanthomonas oryzae pv. oryzae* (*Xoo*), is one of the most destructive plant diseases worldwide. Bacterial Blight is responsible for major losses in the production of the staple crop. The pathogen colonizes the xylem vasculature, a nutrient-scarce environment with continuous sap flow. Therefore, the pathogen manipulates the host metabolism to secure access to carbon resources. One key strategy for achieving this is the deployment of transcription activator-like (TAL) effectors, which induce the expression of clade III *SWEET sucrose transporters* in rice. Hijacking of SWEETs leads to sucrose efflux into the apoplasm. This pathogen-induced reallocation of carbohydrate flux creates a nutrient source that supports the proliferation of *Xoo* and the development of disease. This thesis examines the mechanisms by which *Xoo* acquires and metabolizes host-derived sucrose. A conserved *sux* gene cluster was identified that mediates sucrose uptake and utilization. Functional, structural, and kinetic analyses revealed that SuxB is a GH13-4 sucrose hydrolase with high catalytic efficiency. Evidence for a secreted isoform indicate that SuxB is targeted to both the intracellular and extracellular space, which may expand hydrolytic capacity or support cooperative bacterial growth. These findings establish the *sux* cluster as a central determinant of sucrose acquisition and connect TAL effector–mediated host manipulation directly to pathogen metabolism. Dual transcriptomic analyses show a parallel increase of *SWEET* and *sux* transcripts, indicating that bacterial sucrose uptake is temporally coordinated with host sucrose efflux. Additionally, the ability of *Xoo* to colonize the xylem against the direction of sap flow was investigated using hydrodynamic modeling, microfluidic devices, and adapted infection assays. Finally, novel Matryoshka-based biosensors for sucrose and glucose were developed which provide tools for monitoring sugar dynamics in host–pathogen interactions. By connecting host sucrose release to bacterial metabolic capacity and colonization dynamics, this thesis provides mechanistic insight into the *Xoo* infection process and establishes a framework for resistance strategies targeting pathogen access to host sugars.

Table of contents

1 Introduction **1**

2 A critical role of *sux* cistron-mediated sucrose uptake for virulence of the rice blight pathogen *Xanthomonas oryzae pv. oryzae* **13**

2.1 Introduction 15

2.2 Methods 17

2.3 Results 22

2.4 Discussion 32

3 Sucrose uptake and metabolism via dual-localized SuxB **41**

3.1 Introduction 42

3.2 Methods 44

3.3 Results and discussion 52

3.4 Conclusions and outlook 60

4 Infection against the xylem stream **65**

4.1 Hydrodynamic modeling of *Xoo* swimming motility 66

4.2 Motility of *Xoo* in microfluidic chambers 67

4.3 The role of xylem flow for *Xoo* infection 69

5 Unraveling the host-pathogen interaction between rice and *Xoo* with dualRNAseq **71**

5.1 Introduction 72

5.2 Methods 73

5.3 Results 75

5.4 Discussion 80

6 Evidence for rapid hydrolysis of shoot-derived sucrose using an ultrasensitive ratiometric Matryoshka-type MGlucoMeter sensor **81**

6.1 Introduction 83

6.2 Material and methods 84

6.3 Results and discussion 89

7 Ratiometric Matryoshka MSucMeter sensors for sucrose **103**

7.1 Summary 104

8 Outlook **107**

References **I**

Appendix **XXI**

CHAPTER 1

Introduction

Bacterial Blight of rice

Bacterial blight, caused by the bacterial pathogen *Xanthomonas oryzae pv. oryzae* (*Xoo*), is a disease of major economic and social importance [1, 2]. The bacterium was first observed in Japan in 1884 [3, 4] and was later found in other places, such as the Philippines (1918) or China (1957). Today, *Xoo* occurs in nearly all rice-growing regions, although virulence varies geographically [4]. Due to its presence in various locations, the bacterium has undergone several name changes, from *Pseudomonas oryzae* to *Xanthomonas oryzae*, then *Xanthomonas campestris pv. oryzae*, and finally *Xanthomonas oryzae pv. oryzae*.

Visible symptoms of the disease appear roughly six days after infection. Necrotic lesions develop along the midvein, typically progressing from the leaf tip toward the base, and eventually cause complete necrosis of the leaf. Meanwhile, the bacterial exudates ooze out of the infected leaf, and these droplets can infect new tissue or spread to neighboring plants [1, 3, 4]. Distribution of inoculum can occur via animal movement and with environmental drivers such as winds and tropical storms, which are typical for rice growing regions. Residual inoculum can also persist in harvest debris and plant material from previous seasons, allowing disease recurrence in subsequent seasons [1–3]. While the disease cycle of *Xoo* has been broadly described, the mechanisms underlying systemic spread and colonization of the host remain incompletely understood.

Xoo is a rod-shaped bacterium belonging to the Gram-negative Xanthomonadaceae family that infects the xylem vasculature of rice. *Xoo* measures approximately 0.8–1.0 x 1.7 μm, and is motile with a monotrichous, polar flagellum of 6–8 μm [5, 6]. During infection, *Xoo* switches from a solitary to a biofilm community lifestyle [7]. Colonies have a strong yellow appearance. They are shiny and mucoid due to the extracellular polysaccharide xanthan gum [8].

In this study, the Philippine strain PXO99^A was used. Philippine strains are classified into eleven races based on pathogenicity and resistance, with PXO99^A being a race 6 strain that carries a natural resistance to the mitosis inhibitor azacitidine (A in PXO99^A) [9]. The avirulent strain PXO99^{A}ME2 derived from a mutation of PXO99^A, lacking the transcription activator-like effector (TALE) *PthXo1* [10]. PXO99^{A}ME2 is often used as a control strain as virulent *Xoo* strains secrete key TALEs such as *PthXo1* into the host which activate the transcription of *SWEET sucrose transporters* [11, 12]. Hijacked SWEETs then release sucrose toward the pathogen.

The interaction of rice and *Xoo* has become a central model for studying how pathogens manipulate host sugar transport [4]. Although the TALE–SWEET inter-

action has been studied most intensively in rice, comparable strategies are emerging in various host–pathogen systems, including bacterial, fungal, and oomycete infections [12]. Redirecting host carbohydrate flux is a widespread mechanism by which pathogens obtain nutrients and influence host responses [13]. Consequently, insights from the *Xoo*–rice pathosystem are informative for understanding sugar dynamics in plant–pathogen interactions more broadly.

The role of sugars in plant-pathogen interactions

In higher plants, photosynthesis produces sugars and oxygen from light, water and carbon dioxide [14]. Source and sink tissues are established by the differential allocation of sugars and maintained through symplasmic and apoplasmic transport to distribute assimilates across all organs [15]. Because source tissues present strong defense mechanisms, pathogens often exploit sink tissues or induce transcriptional reprogramming of the host to establish pathogen-induced sink tissues [13, 16, 17]. This highlights the metabolic competition between hosts and pathogens. The role of sugars during infection is discussed in two models [13]. One model hypothesizes that pathogens exploit plant carbohydrates as a nutrient source, facilitating pathogen growth and colonization. The second model considers sugars as signaling molecules that trigger host immune responses. These models are not mutually exclusive; evidence supports both hypotheses, indicating that infection outcomes depend on the dynamics between sugar consumption and sugar-mediated signaling [13].

Depletion of apoplasmic sugars by host sugar transporters

Recent studies across diverse pathosystems have revealed a common host immune strategy: activation of sugar transporters to reduce apoplamic sugar availability and limit pathogen access to host carbon resources. In *Arabidopsis thaliana*, treatment with the bacterial peptide of flagellin, flg22, induces transcription of the *sugar transporter At*stp13 [18]. Comparable host sugar transporter inductions upon pathogen recognition have been observed in other pathosystems. Examples include increased *Zm*sut1 transcription during *Ustilago maydis* infection of the monocot *Zea mays* [19], activation of *At*stp4 during interaction with the fungal biotroph *Erysiphe cichoracearum* [20], and *At*stp13 induction during Arabidopsis infection by the necrotrophic fungus *Botrytis cinerea* [21]. In rice, however, whether comparable sugar retrieval mechanisms operate during Bacterial Blight remains an open question.

Activation of plant immunity triggered by the conserved bacterial flagellin peptide flg22 describes one layer of plant immunity. Plant immunity is activated either by pattern-triggered immunity (PTI), initiated upon recognition of conserved microbial, such as flg22, and damage-associated molecular patterns (MAMPs/DAMPs), or by effector-triggered immunity (ETI). In flg22-treated *Atstp13* mutants, the accumulation of extracellular hexoses indicates that *At*STP13 directly mediates sugar uptake in response to MAMP perception. Yamada et al. demonstrates that recognition of flg22 by the FLS2–BAK1 receptor complex leads to phosphorylation of the C-terminal domain of *At*STP13 by the BAK1 receptor kinase, thereby providing a mechanistic explanation for the regulation of this sugar transporter [18].

Recent studies have shown that PTI induces sugar transporters such as *At*STP13 to deplete apoplasmic sugars and limit pathogen access to host carbon resources [18]. Consistently, the increased proliferation of the T3SS-deficient ΔhrpC strain in stp1/stp13 plants indicates that STP1- and STP13-mediated sugar retrieval contributes to restricting the growth of *Pseudomonas syringae* [18]. This effect occurs independently of effector-mediated suppression of host immunity, highlighting that sugar uptake itself constitutes a mechanistic component of PTI [18]. In addition, sugars can act as signaling molecules, triggering immune responses such as cell wall fortification, the production of reactive oxygen species (ROS), and the synthesis of pathogenesis-related proteins [17]. Exogenous sucrose application enhances resistance against both *Magnaporthe oryzae* and *P. syringae* [17, 22], and sugar accumulation in leaves correlates with increased expression of defense genes [23].

Sucrolytic enzymes and uptake systems in plant pathogens

In order to secure host sugars during infection, pathogens have developed a variety of strategies such as the secretion of invertases and other sucrolytic enzymes early on in the infection [24]. Enzymes from the glycoside hydrolase family 32, which break down sucrose into hexoses, are found in many plant-pathogenic fungi [17, 25, 26], but also other pathogens such as *Xanthomonas* or *Phytophthora* species release invertases and cell wall–degrading enzymes into host tissues [16, 17, 27]. The abundance of these sucrolytic enzymes and hexose transporters represent the role of hexoses as often preferred carbon source [26]. Further, the preference for hexoses is highlighted by transcriptome analysis of *Puccinia striiformis* during infection, which detected hexose, but not sucrose transporters [28, 29]. How *Xoo* secures sugars has only recently begun to be understood (see Chapter 2).

Although sugars released by extracellular hydrolysis can facilitate the growth of pathogens, the breakdown products can also serve as damage-associated molecular patterns (DAMPs) that trigger PTI [30]. Thus, sucrolytic enzymes and their products represent a delicate balance: they provide nutrients to the pathogens while risking immune recognition by the hosts. Interestingly, this trade-off is more critical for biotrophic pathogens, which rely on maintaining host cell viability. As an alternative strategy to secreting sucrolytic enzymes, the corn smut fungus *Ustilago maydis* expresses a high-affinity sucrose transporter, *Um*Srt1, after colonization [31]. By directly importing sucrose, the pathogen avoids extracellular hydrolysis, therefore DAMP-triggered PTI and counteracts host starvation defense.

Another example for the evolutionary importance of sugar and sugar uptake during infections can be seen in the interaction between *Phytophthora sojae* and soybean. *P. sojae* secretes the glucanase enzyme *Ps*XEG1 into host tissue to gain access to nutrients, where the host releases the inhibitor protein *Gm*GIP1 quenching glucanase activity. To overcome this inhibition, *P. sojae* evolved a structural paralog, *Ps*XLP1. Although catalytically inactive, the paralog *Ps*XLP1 binds *Gm*GIP1 with higher affinity, acting as a decoy that sequesters the inhibitor [16]. This example demonstrates the evolutionary arms race and links sugar acquisition strategies with host defense mechanisms.

The role of sugars in Bacterial Blight

Similar to the previously described pathosystems, in the interaction between rice and *Xoo*, competition for sugars is a decisive factor in determining disease outcome. Within three days post-infection (see also Chapter 5), *Xoo* activates its type III secretion system (T3SS), which secretes bacterial effectors directly from the cytosol of the pathogen into the cytosol of the host. Among the secreted effectors are transcription activator-like effectors (TALEs). TALEs translocate into the plant cell nucleus, where they bind to effector binding elements (EBEs) in the promoters of effector genes, such as *SWEETs*. *PthXo1* TALE binding leads to transcription and subsequent translation of SWEET11a in the infected cells. The resulting increase in sucrose efflux via SWEETs leads to an artificial pathogen-induced sink at the infection site, directing sucrose towards the pathogen. Both T3SS activity and TALE-mediated induction of *SWEET* genes are essential for *Xoo* virulence and disease development.

Rice encodes 21 *SWEET* genes, distributed across all four phylogenetic clades [32]. Members of clades I, II, and IV predominantly transport hexoses, whereas clade III

SWEETs (*Os*SWEET11a, *Os*SWEET12, *Os*SWEET13, *Os*SWEET14, *Os*SWEET15) primarily mediate sucrose transport. For *Xoo* infection, only clade III members are relevant [32, 33]. The functions of *Os*SWEET11a and *Os*SWEET13 as recessive blight resistance loci were even established before the SWEET family was identified [10, 34]. Later studies demonstrated that *Os*SWEET14 is also targeted by *Xoo* [35]. In contrast, *Os*SWEET12 and *Os*SWEET15 can support infection when artificially activated by designer TALEs, but have not been detected as natural *Xoo* targets to date [33]. While glucose-transporting SWEETs, such as *Vv*SWEET4, are relevant for *Botrytis cinerea* infections of *Vitis vinifera* [36], activation of glucose-transporting SWEETs in rice does not promote Bacterial Blight disease [33, 37]. Because glucose-uptake-deficient *Xoo* mutants can still colonize and proliferate in rice [33, 37], the findings indicate that sucrose released by clade III *Os*SWEETs represents a critical and accessible carbon source for *Xoo* distinct from glucose.

Molecular studies on sucrose utilization by phytopathogens began only in the last two decades with *Erwinia amylovora* [38, 39]. In *E. amylovora*, sucrose is imported via a sucrose-specific phosphotransferase system (PTS) [38]. In *Xoo*, however, early work detected PTS activity only for glucose import [37], indicating that sucrose acquisition follows an alternative mechanism in *Xanthomonas* species. Kim et al. [39] identified sucrose transporters in *Xanthomonas axonopodis pv. glycines* (*Xag*) and *Xanthomonas campestris pv. campestris* (*Xcc*) with approximately 20 % sequence identity to the plant sucrose transporter SUC1. The authors also discovered a sucrose hydrolase (SUH) in *Xag* whose deletion abolished growth on sucrose [39]. The lack of SUH activity toward sucrose-6-phosphate further argued against PTS-dependent sucrose import. Additionally, Blanvillain et al. [40] observed that TonB-dependent receptors (TBDRs) are common in *Xanthomonas* species and bacteria that utilize complex carbon sources. They identified a TBDR required for pathogenicity in *Xcc*, encoded in an operon alongside a sucrose hydrolase, orthologous to SUH of *Xag*. The authors renamed this operon *sux* for sucrose utilization in *Xanthomonas* [40]. We recently demonstrated that the *sux* cluster mediates sucrose uptake in *Xoo* (see Chapter 2) [41]. Host-pathogen dualRNA-seq revealed spatio-temporal co-expression of *sux* genes with *OsSWEET11a* (see Chapter 5), linking bacterial sucrose acquisition to host sucrose efflux. Structural analysis of a sucrose hydrolase in *Xoo* (SuxB) confirmed exclusive sucrose hydrolase activity [41], mirroring that of SUH in *Xag*, and substantiating PTS-independent sucrose import in *Xanthomonas*.

The xylem as a battleground

The xylem represents a highly specialized yet challenging niche for plant pathogens. Only a few pathogens have evolved to thrive there, but those that have are among the most destructive in agriculture [42]. Examples include *Ralstonia solanacearum*, *Xanthomonas oryzae pv. oryzae*, *Erwinia amylovora*, *Pseudomonas syringae*, and *Xylella fastidiosa* [4, 38, 42, 43]. Once inside the vessels, the pathogens often produce large amounts of extracellular polysaccharides (EPS) eventually resulting in biofilms, which can occlude water transport, contributing to the wilting symptoms that are characteristic of many xylem diseases [4, 38, 42, 43]. Xylem colonization therefore offers both advantages and challenges. Reduced microbial competition is an advantage of this niche, but the fast-moving stream of xylem sap creates mechanical stress, can disrupt communication between bacterial cells and dilutes nutrients [43–46]. How *Xoo* manages to migrate against the flow of xylem sap remains an unresolved question (addressed in Chapter 4).

Entry into the xylem during Bacterial Blight

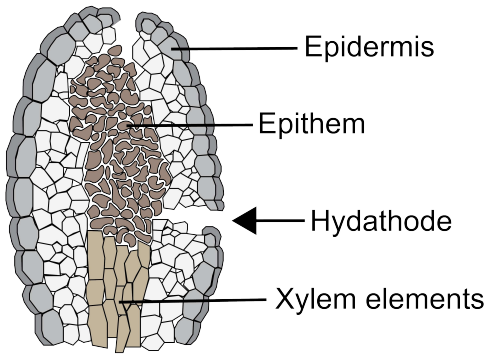

Figure 1.1: Schematic drawing of a rice leaf hydathode highlighting the distinct tissues at the entry point for *Xoo* and potential bacterial routes (dashed lines).

Xoo is a vascular pathogen that gains access to rice leaves primarily through wounds and natural openings such as hydathodes [47]. Hydathodes are pores located along the leaf margins, where they connect directly to the xylem vessels through the epithem, a loose layer of metabolically active parenchyma cells (Figure 1.1). This anatomical connection allows rapid transition from local colonization to systemic spread through the vascular system. Current models propose that leaf infections begin when *Xoo* enters via the hydathodes and multiplies in the epithem [42]. In contrast to *Xcc*, *Xoo* does not kill parenchyma cells, which may explain the activity of *Xa3/Xa26* and *Xa27* resistance genes in the rice leaf blade [42]. In general, immune responses at hydathodes play an important role in restricting bacterial entry and early colonization [48]. To date, little is known how *Xoo* undergoes the hosts defense response, since *Xoo* cells move from the epithem into the xylem vessels, from where they spread systemically through the host.

Guttation fluid may provide an alternative entry path into the leaf. At night, when transpiration is low, water exudes from the hydathodes in a process called guttation. In the morning, this fluid can be reabsorbed by the plant, which poses a risk of introducing microorganisms directly into the vasculature [49]. An experimental study by Kajetan Linkert (B.Sc. thesis, see Appendix) demonstrated that rice guttation droplets inoculated with fluorescent beads were reabsorbed and moved up to 1.2 cm into the leaf. The data indicate that guttation reuptake could introduce bacteria into the leaf tissue, potentially circumventing early immune detection.

Interestingly, in order to cause Bacterial Blight in the leaves, the tissue must be infected through an entry point above ground. Kresek is a severe form of Bacterial Blight that causes complete wilting and death of seedlings. In this case, *Xoo* colonizes the root xylem but does not progress beyond the shoot–root junction [50]. These observations support the conclusion that leaf Bacterial Blight in rice originates exclusively from leaf infections.

The role of EPS for xylem infections

Within the xylem, *Xoo* and other xylem pathogens encounter two primary challenges: nutrient limitation and high sap flow rates. Cell wall–degrading enzymes can release sugars from host cell walls [51], but these sugars are likely diluted and rapidly transported away by the xylem stream. To reduce sugar loss and maintain position within the flowing sap, planktonic cells initiate biofilm formation through secretion of EPS [24, 52]. EPS anchors bacterial cells to vessel walls and shield them from shear forces [53]. When EPS develops into a biofilm, the film matrix retains nutrients, quorum-sensing molecules, metabolic byproducts, and extracellular enzymes [53, 54]. EPS production also marks the transition point from planktonic cell state to colony state. Eventually, cells that are released from the outer biofilm layers disperse from the colonies and colonize new vessel segments [53].

As biofilms mature, they can occlude xylem elements and reduce local sap flow promoting disease development [4]. In rice leaves, xylem sap typically flows from the base toward the tip; however, Bacterial Blight lesions often expand in the opposite direction, from the tip toward the base [3]. Local vessel obstruction could generate micro-environments with reduced flow, enabling *Xoo* to migrate against the bulk flow. In addition to biofilm formation, *Xoo* may further reduce xylem flow through effector-mediated host manipulation. For example, the effector XopD, although recognized by the plant immune system, still benefits the pathogen. XopD recognition leads to an accumulation of host abscisic acid (ABA), which causes stomata closure [55,

56]. This immune response limits entry points for new pathogens and increases water availability. Still, it creates a condition that is beneficial for *Xoo*, by reducing transpiration and xylem sap flow [56].

Microfluidics for studying xylem colonization

Xylem infections are challenging to study due to the structural complexity of the vascular system, difficulty in controlling biophysical conditions *in planta*, and strong lignification of xylem elements, which causes intense autofluorescence during imaging [46]. Over the past two decades, microfluidic chips have been increasingly applied in microbiology to investigate microbial pathogenesis factors in controlled environments, such as chemotaxis, motility and bacterial attachment to surfaces [57–60]. These developments in microfluidic chip design provide a conceptual and methodological foundation for the approaches presented in Chapter 4, where xylem-mimicking devices are employed to investigate *Xoo* colonization dynamics.

Recent chip designs can reproduce key xylem parameters, including variable sap flow rates, transient occlusions, embolism formation or surface modification. Attachment chips incorporate bacterial surface adhesions enabling quantitative studies of adhesion dynamics [60]. Attachment to surfaces is a key virulence factor of non-flagellated *Xylella fastidiosa* cells, which move in the xylem via type IV pili-mediated twitching motility [61, 62].

In *Xoo*, the roles of motility, attachment, and chemotaxis in xylem colonization remain poorly understood [4]. Transcriptome analysis of *Xcc*-infected hydathodes revealed repression of chemotaxis and motility genes [58], similar to chemotaxis attraction of *Xoo* to guttation fluid from susceptible hosts, which is repressed once the bacterium reaches the hydathode [63, 64]. Microfluidic data could gain insights into the details of the infection beyond descriptive assays and generate mechanistic predictions. For example, experimental results have informed models that highlight the importance of both attachment and detachment/dispersal from biofilms during infection [65]. In addition, motility chip designs have provided insight into bacterial positioning within flow streams and have informed predictive models linking motility patterns to cell body morphology and flagellar architecture [66].

Motivation and open questions

In 2020, rice served as the primary staple for more than half of the world's population, feeding over four billion people [1, 2]. Rice provides more than 18 % of the calories consumed worldwide [67]. Current projections indicate further increases in rice consumption, stressing that global food security depends on this crop, and highlighting the urgent need to understand and control devastating diseases such as Bacterial Blight.
A global study of major food crops estimated that rice production in the Indo-Gangetic Plain suffers an average yield loss of about 40 % due to pests and pathogens [68]. Within this burden, Bacterial Blight, caused by *Xoo*, is the most significant contributor. Savary et al. attributed an 8.5 % loss of rice yield in the Indo-Gangetic Plain specifically to Bacterial Blight [68]. These losses threaten all social strata. In 2019, the Healthy Crops consortium estimated annual monetary losses of 3.6 billion dollars, along with existential threats to livelihoods of 600 million small-scale farmers and their families (www.healthycrops.org). These considerations provide the rationale for this thesis, which addresses the molecular basis of rice–*Xoo* interactions with a particular focus on sugar transport and metabolism as key determinants of disease outcome.

Over the past decade, significant progress has been made in dissecting the interaction between rice and *Xoo* [2]. Identifying SWEETs in Bacterial Blight as targets for both T3Es and resistance engineering has elevated research to a new level [69]. Yet, the infection process remains incompletely understood.
Editing sucrose-releasing SWEETs has allowed researchers of the Healthy Crops consortium to achieve resistance against *Xoo*. Still, it is not clear why the pathogen relies so strongly on sucrose. Understanding this dependency could point the way toward resistance strategies that work better and last longer. Why do sucrose-transporting SWEETs promote disease, whereas glucose-transporting SWEETs do not? By what mechanism does *Xoo* access and utilize host-derived sucrose within infected tissues? Resolving these questions is critical, as it would provide a mechanistic foundation for optimizing and extending SWEET-based resistance strategies.
In other pathosystems, hosts frequently reimport apoplastically released sugars, predominantly hexoses, to restrict pathogen access. If rice employs a similar defense, how does *Xoo* overcome it? Moreover, while most plant–pathogen interactions rely on hexose availability, virulence in *Xoo* uniquely depends on sucrose.
Looking further at hydathode infections, little experimental evidence explains the role of guttation reuptake in early infection. Once the bacterium reaches the xylem,

another puzzle arises: how does *Xoo* spread against the acropetal water stream, given that Bacterial Blight progresses basipetally?

This dissertation addresses key open questions about sugar uptake (Chapter 2) and its role during infection (Chapters 3 and 5) and xylem colonization (Chapter 4) by *Xoo* in rice, providing insights that may guide the development of improved resistance strategies. In Chapters 6 and 7, newly developed sugar sensors are presented, which offer tools to study the dynamics of sugar competition during host–pathogen interactions.

CHAPTER **2**

A critical role of sux cistron-mediated sucrose uptake for virulence of the rice blight pathogen *Xanthomonas oryzae pv. oryzae*[1]

1: This chapter is based on the article: A critical role of *sux* cistron-mediated sucrose uptake for virulence of the rice blight pathogen *Xanthomonas oryzae pv. oryzae* by **Nora R. Zoellner**, Juying Long, Congfeng Song, Jacob Sharkey, Michael M. Wudick, Eliza P.I. Loo, Mayuri Sadoine, Violetta Applegate, Astrid Höppner, Sander H.J. Smits, Bing Yang and Wolf B. Frommer; it was published at biorxiv [41] and submitted to PNAS Nexus.

Contributions of Nora R. Zöllner: Conceived and designed experiments with BY and WBF. Performed experiments, including the generation of mutant lines; growth, EPS, biofilm, and motility assays; heterologous expression, purification, and kinetic analysis of SuxB; performed qRT-PCR and transcriptome profiling; infection experiments in collaboration with LJ and CS. Analyzed PCA and volcano plots with JS. Interpreted crystallization results with VA, AH, and SHJS. cDNA library preparation and sequencing were carried out at Novogene. Co-wrote the manuscript with WBF.

Abstract

The virulence of *Xanthomonas oryzae pv. oryzae*, the causal agent of bacterial blight (BB) of rice, critically depends on the activation of SWEET sucrose uniporters of the host. To date, the role of SWEET-released sucrose for virulence remains unclear. We here identified the *sux* locus of *Xoo*, consisting of a LacI-type repressor (SuxR), an outer membrane TonB-like porin (SuxA), an inner membrane MFS H^+-symporter (SuxC), and a cytosolic sucrose hydrolase (SuxB). Structural and functional analyses demonstrate that SuxB has exclusive sucrose hydrolase activity. Mutant analyses show that the transporter SuxC and the sucrose hydrolase are necessary for growth of bacteria on sucrose, while SuxA is not essential, likely due to the ability of other porins to transport sucrose across the outer membrane. Consistent with a role of SuxR as a sucrose repressor, transcriptome studies show sucrose-dependent regulation of the *suxA/suxB* genes. Besides a role of sucrose for reproduction, we found that sucrose promotes motility, EPS production, biofilm formation, and virulence. Notably, the SuxC sucrose H^+-symporter and the sucrose hydrolase SuxB were required for full virulence of *Xoo* on indica and japonica rice varieties. Our findings indicate that pathogen-induced sucrose efflux via SWEETs provides sucrose to *Xoo*, that *Xoo* uses the *sux* gene cluster to acquire and utilize sucrose, and that sucrose promotes bacterial fitness and xylem colonization.

Significance statement

Understanding disease mechanisms is critical for developing strategies to protect plants against infections. Bacterial blight, a major threat to global rice production, is caused by *Xanthomonas oryzae pv. oryzae* strains that hijack rice SWEET sucrose uniporters. *Xanthomonas oryzae pv. oryzae* deploys a set of molecular 'keys', TAL effectors, to trigger host sucrose release. Sugars could serve as nutrients for the bacteria or prime host defense. Here, we provide evidence that the pathogen's ability to attack and grow depends on sucrose uptake. We explore how crucial virulence functions, such as motility, EPS production, and biofilm formation, depend on the activity of the sucrose utilization system, supporting a key role of sucrose for the nutrition of the bacteria in the xylem.

2.1 Introduction

Pathogens cause major crop losses, with massive economic and food security impacts. Bacterial blight (BB) is one of the major causes of rice yield losses, especially in Asia. Recent BB outbreaks in Tanzania and Madagascar and spread across East Africa led to substantial yield losses particularly affecting small-scale food producers [1]. The causal agent of BB is the gram-negative bacterium *Xanthomonas oryzae pv. oryzae* (*Xoo*) [4]. From the phyllosphere, *Xoo* invades the water-conducting xylem vessels by entering via wounds or hydathodes [7, 47]. Within the xylem, *Xoo* moves in the xylem stream, then adheres to host cell walls, undergoing a transition from planktonic to sessile states from which new planktonic cells disperse and generate a progressive infection even against the xylem stream [7, 47]. These transitions have to be timed precisely for effective infection. The regulatory networks driving infections of *Xoo* are highly complex, including light and quorum sensing, the secondary messengers c-di-GMP, and alternative sigma factors such as σ^{54} [70, 71]. The regulatory network coordinates motility, biofilm formation, and virulence [24, 72, 73].

The xylem provides a niche with reduced microbial competition but presents major challenges, e.g., the rapid xylem flow [44, 46]. Swimming against the stream is likely highly energy-intensive. The production of extracellular polysaccharides (EPS) and biofilm, required for withstanding the physical forces of the xylem flow, requires carbon skeletons and energy [74]. Biofilm can protect against at least the loss of quorum-sensing molecules and metabolites, secreted in the newly forming colonies, fostering bacterial communication and reproduction [53, 74, 75]. The high demand for carbon skeletons and energy poses major challenges since carbohydrate levels in the xylem sap are scarce, likely restricting bacterial virulence and growth [38, 45, 76, 77]. Freeze-dried guttation fluid, a proxy for xylem sap, failed to support *Xoo* growth, except when sucrose was added [78]. *Xoo* metabolizes hexoses via the Entner-Doudoroff pathway, producing only one ATP compared to two ATP for the Embden-Meyerhof pathway, thus limiting ATP production from the low sugar available in the xylem sap [79, 80].

We hypothesize that *Xoo* utilizes sucrose as the major carbon and energy source during the infection. After adhering to the xylem walls, *Xoo* produces a type 3 secretion system (T3SS) to inject bacterial type III effectors (T3E) into the xylem parenchyma that induce *SWEET* sucrose uniporter genes [11, 12]. As a consequence, SWEETs likely sequester sucrose, making it available to *Xoo* [81, 82]. All pathogenic *Xoo* strains studied to date rely on activation of at least one of three sucrose uniporters [33, 69, 83]. In contrast, glucose-transporting SWEETs do not support *Xoo* infection when artificially induced, and glucose uptake-deficient *Xoo* mutants remain able

to colonize the xylem [33, 37]. There are two hypotheses regarding the role of *SWEET* induction for pathogen resistance: host priming and pathogen feeding [13]. For *Colletotrichum higginsianum* infections, *SWEET* induction may lead to an overaccumulation of sugars in the extracellular space, and high extracellular sugar levels have been implicated in defense priming via the salicylic acid pathway [23]. In line with the priming hypothesis, sucrose supplementation led to increased resistance to blast [22]. However, in the case of BB, the induction of *SWEETs* appears to be the basis of susceptibility, not increased resistance; resistance was increased when the bacteria could not induce a *SWEET*. The most parsimonious hypothesis for the role in BB is thus that carbohydrate levels in the xylem limit bacterial reproduction and virulence, and that sucrose released from the xylem parenchyma via SWEETs provides sucrose to the pathogen. The genomes of *Xanthomonads* showed an enrichment of transport systems that make use of TonB-like porins (TBDR)[40]. Analysis of 76 TBDR mutants in*Xanthomonas campestris pv. campestris* (*Xcc*) identified the *TBDR XCC3358* gene as relevant for sucrose uptake. Deletion of the *TBDR XCC3358* gene caused delayed infection development [40]. In *Xanthomonas axonopodis pv. glycines* (*Xag*) and *Xanthomonas axonopodis pv. manihotis* (*Xam*), mutations of respective sucrose utilization (*sux*) loci resulted in no or only moderate delay in symptom development, respectively [39, 84]. To explore the role of sucrose for the virulence of *Xoo*, we tried to identify sucrose uptake systems. Here, we analyzed the *sux* cistron of *Xoo*, encoding a LacI-type repressor, an outer membrane TonB-like porin, an inner membrane MFS-family sucrose/H^+, and a putative cytosolic amylosucrase. Transcriptomics were used to characterize the four genes in the *sux* operon. Structural, biochemical, and genetic analyses of the *sux* genes show that the *sux* locus is necessary for sucrose utilization in *Xoo* and plays critical roles for swimming, swarming, EPS production, and biofilm formation. Most importantly, the *sux* gene functions are critically required for virulence in japonica and indica varieties of rice. Sucrose-induced transcriptional regulation indicated that sucrose and its metabolic downstream products promote vital bacterial functions during xylem colonization, in particular after *SWEET* induction, as indicated by the presence of the *LacI-type repressor* gene in the cluster. We surmise that a better understanding of how host-derived sugars serve as nutrients for pathogens will help to develop innovative and long-term strategies against pathogen infection for BB, cassava, and cotton blight, but possibly also against other pathogens.

2.2 Methods

Bacterial strains, plasmids, and DNA constructs

One Shot TOP10 *Escherichia coli* cells (ThermoFisher, C404006) were cultivated at 37 °C in LB (5 g/L yeast extract, 10 g/L tryptone, 10 g/L NaCl, pH 7). When required, kanamycin (50 µg/mL) was added for selection. *Xanthomonas oryzae pv. oryzae* strain PXO99^{A} was grown at 28°C in optimized nutrient broth (NB) (1 g/L yeast extract, 3 g/L beef extract, 5 g/L peptone, pH 7, 1.5 % w/v agar). When necessary, medium was supplemented with sugar (30 mM sucrose or 30 mM glucose) or antibiotics (25 μg/mL kanamycin or 50 μg/mL spectinomycin). Standard DNA techniques were used for *E. coli* and recombinant DNA manipulations as previously described [85].

Construction of *sux* mutants in PXO99^{A}

Homologous recombination was used to generate *Xoo* mutant lines. Genomic DNA (gDNA) of PXO99^{A} was extracted using the DNeasy Blood& Tissue kit (Qiagen, 69506). Flanking regions of roughly 200 bp up- and downstream of the gene of interest were amplified from gDNA using restriction digest cloning. The flanking sites were cloned in-frame around a spectinomycin cassette into the suicide vector pK18sB in *E. coli* cells. pK18sB was a gift from Gredd Beckham and Christopher Johnson [86]. Electrocompetent PXO99^{A} was transformed with 500 ng of plasmid DNA via electroporation for 5 sec at 2.5 kV and 200 Ω in a 0.1 cm MicroPulser cuvette (Bio Rad, 1652089). After recovery in Recovery Medium For Expression (Sigma, CMR001-8X12ML), sucrose-tolerant, spectinomycin-resistant and kanamycin-sensitive colonies were selected in multiple rounds of re-plating.

Bacterial growth studies of PXO99^{A} and mutant strains

Bacterial growth studies of PXO99^{A}, Δ*sux*, Δ*suxR*, Δ*suxC*, Δ*suxA*, and Δ*suxB* were initiated at a starting OD_{600} of 0.1-0.2 using a mid-logarithmic pre-inoculum. Cultures were grown in 12-well, flat-bottom, transparent plates in a plate reader (Tecan Spark) at 28°C and 200 rpm of constant shaking. *Xoo* was grown in NB, NB + 30 mM sucrose, and NB + 30 mM glucose. OD_{600} was measured every 30 minutes over a course of 24 hours.

Total RNA isolation and transcriptome analysis

100 mL media (NB, NB + 30 mM sucrose, and NB + 30 mM glucose) were inoculated in Erlenmeyer flasks with a mid-logarithmic pre-inoculum of PXO99^{A} to OD_{600} of 0.1-0.2. Cultures were incubated on an orbital shaker at 28 °C and 200 rpm. OD_{600} was measured every two hours over a period of 8 hours. Additionally, triplicates of 2 mL samples were taken and total RNA was extracted using the TRIzol Max Bacterial RNA Isolation kit (ThermoFisher, 16096020) followed by Direct-zol RNA Miniprep kit (Zymo, R2051). Complementary DNA (cDNA) library prep for Illumina sequencing was performed on pooled triplicates of total RNA by Novogene (UK, Cambridge). For qRT-PCR, total RNA was transcribed into cDNA using the Maxima H kit (ThermoFisher, M1682). 2 ng of cDNA were used as template. The $2^{-\Delta\Delta}$ct method was performed and Δct values are presented in the analysis with gyrA as housekeeping gene [87].

Differential expression analysis and visualization

Raw gene counts were quantified by Novogene with FeatureCounts (82) and normalized to counts per million (CPM) using EdgeR. Principal component analysis (PCA) was completed with the prcomp() function of the stats R package. The final PCA plot was generated in R with ggplot2. Overlap of treatment groups is visualized by overlaying the PCA plot with convex hulls using the chull() function of the grDevices package (83). Differential expression was visualized using a modified version of the volcano3D package (84). Gene length-corrected trimmed mean of M-values was calculated for each sample using raw gene counts as input (85). P-values and fold changes were determined at each time point by comparing three media types (NB, NB + glucose, and NB + sucrose). P-values, fold changes, and z-scaled expression values were input into the polar-xy() and polar-p() functions of the volcano3D package, producing polar coordinate tables formatted for the volcano3D plot. The RNAseq data and R scripts used in these visualizations are deposited in the DataPlant ARC published alongside this paper.

Crystallization, data collection and structure refinement for SuxB-apo and SuxB in complex with glucose

Initial screening for crystallization conditions was performed at 12 °C in sitting drop plates using vapor diffusion method and commercially available screens. Crystals

were optimized and appeared at 0.25 M potassium sodium tartrate and 32.5 – 37.5 (w/v) % PEG 3350 as precipitant. Before crystals were harvested for data collection, 1 μL ethylene glycol was added to the crystallization drops and these were overlaid with mineral oil as a cryoprotection protocol before they were flash frozen in liquid nitrogen. A complete data set for the SuxB apo structure was collected at the ESRF (Grenoble, France), beam line ID23-2, at 100 K. Data were auto-processed with EDNA-proc and together with an AlphaFold3 model of SuxB used in molecular replacement for solving the structure (phaser-MR, ccp4 suite). The SuxB structure was further built and refined using iterative cycles of manual building in COOT and automated refinement processes using PHENIX Refine. Data collection and refinement statistics can be found in Supplementary Table 2.3. Crystallization of SuxB in complex with glucose was performed as described above, but cryoprotection procedure was slightly different: Before crystals were harvested, 1 μL of a saturated sucrose solution was added to the crystallization drops before they were overlaid with mineral oil and flash frozen in liquid nitrogen. A complete data set for the SuxB complex structure was collected at the EMBL, beam line P13 (DESY, Hamburg, Germany) and auto-processed with autoPROC. Molecular replacement with phaser-MR was performed using the refined structure of apo SuxB. Model building and refinement were performed as described above, additionally in two of the three chains of SuxB within the asymmetric unit could be manually be fitted to one fructose molecule in the additional density at the active site.

Monitoring bacterial colony morphology

To assess phenotypic characteristics, 3 μL of cultures from deletion strains or wildtype PXO99^{A} were spotted onto solid NB agar with or without 30 mM sucrose. Photos were captured 3 days after incubation at 28 °C.

Analysis of biofilm formation

Biofilm formation was evaluated using a 'hanging droplet' assay. After culturing *Xoo* on solid NB media with 30 mM sucrose, plates were inverted so that the agar was on top. Plates were left to stand for 30 minutes. The presence or absence of hanging biofilm droplets was observed and photographed.

Motility assays

Xoo was grown in NB media in Erlenmeyer flasks to mid-logarithmic phase before dilution to a starting OD_{600} of 0.1. 2 μL of the dilution were dropped onto 0.6 % agar plates with 30 mM sucrose for swarming assays, and onto 0.3 % agar plates with 30 mM sucrose for swimming motility assays. Motility areas were measured 3 days after incubation at 28 °C.

Analysis of EPS production

Xoo was grown in NB medium in Erlenmeyer flasks to mid-logarithmic phase before dilution to a starting OD_{600} 0.1-0.2 in NB media with 0 mM sucrose, 30 mM sucrose or 30 mM glucose. Cells were grown for 24 hours at 28 °C on an orbital shaker at 200 rpm in 24 well-plates, medium without *Xoo* served as control for background subtraction. Plates were removed from the shaker and kept standing still for 24 hours before quantifying EPS using crystal violet (CV) staining. Medium was removed and wells were washed with dist. water. 0.1 % CV (certified by the Biological Stain Commission, Sigma) was added to the wells and incubated for 10 minutes before rinsing with water. Finally, bound CV was solubilized in ethanol. Plates were photographed before CV quantification in a spectrophotometer (emission at 570 nm).

Disease assays in rice leaves

Oryza sativa ssp. japonica cv. Kitaake and *cv. Nipponbare*, as well as *Oryza sativa ssp. indica cv. IR24* were grown in a plant growth chamber (12 h light, 28 °C; 12 h dark, 25 °C, 80 % humidity). Four-week-old rice plants were inoculated with bacterial suspensions in sterile distilled water at approximately OD_{600} 0.5 using leaf tip-clipping. Lesion lengths were quantified 12 DAI as described [88].

Building the phylogenic tree of the *sux* gene cluster

Sequences were aligned using MAFFT and curated with BMGE to remove poorly aligned regions. A maximum likelihood phylogenetic tree was inferred with PhyML, using the GTR substitution model. The tree was rendered and displayed in Newick format with 10000 replicates for bootstrapping and visualization using www.ngphylogeny.fr [89].

Statistics

Statistics were performed using the OriginLab Stats Adviser (OriginPro 2024b).

2.3 Results

Identification of a sucrose utilization gene cluster

To investigate whether and how *Xanthomonas oryzae pv. oryzae* (*Xoo*) can acquire sucrose, and to identify potential sucrose uptake and metabolic systems, we performed RNAseq on the Asian *Xoo* strain PXO99^{A}. Cultures were grown *in vitro* in media supplemented with sucrose, glucose, or without additional carbon source, and samples were collected over an eight-hour time course. To assess transcriptomic changes and identify treatment-specific differences, we performed principal component analysis (PCA). PCA identified distinct temporal (PC1, 39.4 %) and treatment-specific (PC2, 20.1 %) clustering. At 2 hours, the samples of sucrose, glucose, and without additional carbon sources clustered. At the four-hour timepoint, transcriptomes of the three media treatments diverged. Transcriptomes of samples grown without additional carbon sources became increasingly dissimilar from samples grown in sugar-supplemented media over time (Figure 2.1).

We identified 192 differentially expressed genes (DEGs) in sucrose-treated samples compared to no sucrose (p-value <0.05 and log2-fold change >2). Among the DEGs, 134 had decreased and 58 had increased steady-state transcript levels (Figure 2.1b). The DEGs with increased transcripts were chaperones (*groE*, *clpB* and *htpG*), enzymes (*NADH-oxidoreductase*), membrane proteins such as *cytochrome B*, and an *outer membrane ß-barrel transporter* of the TonB family. Of particular interest regarding the acquisition of host-derived sucrose were two genes encoding an *amylosucrase* (PXO02416, RS19450, hereafter named *suxB*) and an *outer membrane ß-barrel TonB-family transporter* (PXO02415, RS19445, hereafter named *suxA*), both encoded in an operon encoding two proteins. To validate the sucrose-mediated induction of *suxAB* transcripts observed in the *in vitro* RNAseq data, bacterial growth assays were performed under various carbon supply conditions. The wildtype (PXO99^{A}) exhibited minimal growth in the absence of an external carbon source, reflecting a base growth, whereas supplementation with sucrose or glucose elevated proliferation rates by 1.5-fold each (Figure 2.2a). The coordinated induction in *amylosucrase* transcripts and the associated *outer membrane transporter* led us to hypothesize that *Xoo* evolved a distinct uptake mechanism for sucrose. SuxB showed 81 % protein identity to SuxB$_{Xcc}$ in the *sux* genes from *Xanthomonas campestris pv. campestris* [40]. Further analysis of the locus revealed a cistron composed of four genes including a *LacI-type repressor* (*suxR*) and an *inner membrane transporter* belonging to the major facilitator superfamily (MFS), likely functioning as a H^+-symporter (*suxC*) (Figure 2.1c; Supplementary Table 2.1). Notably, sucrose-induced DEGs from

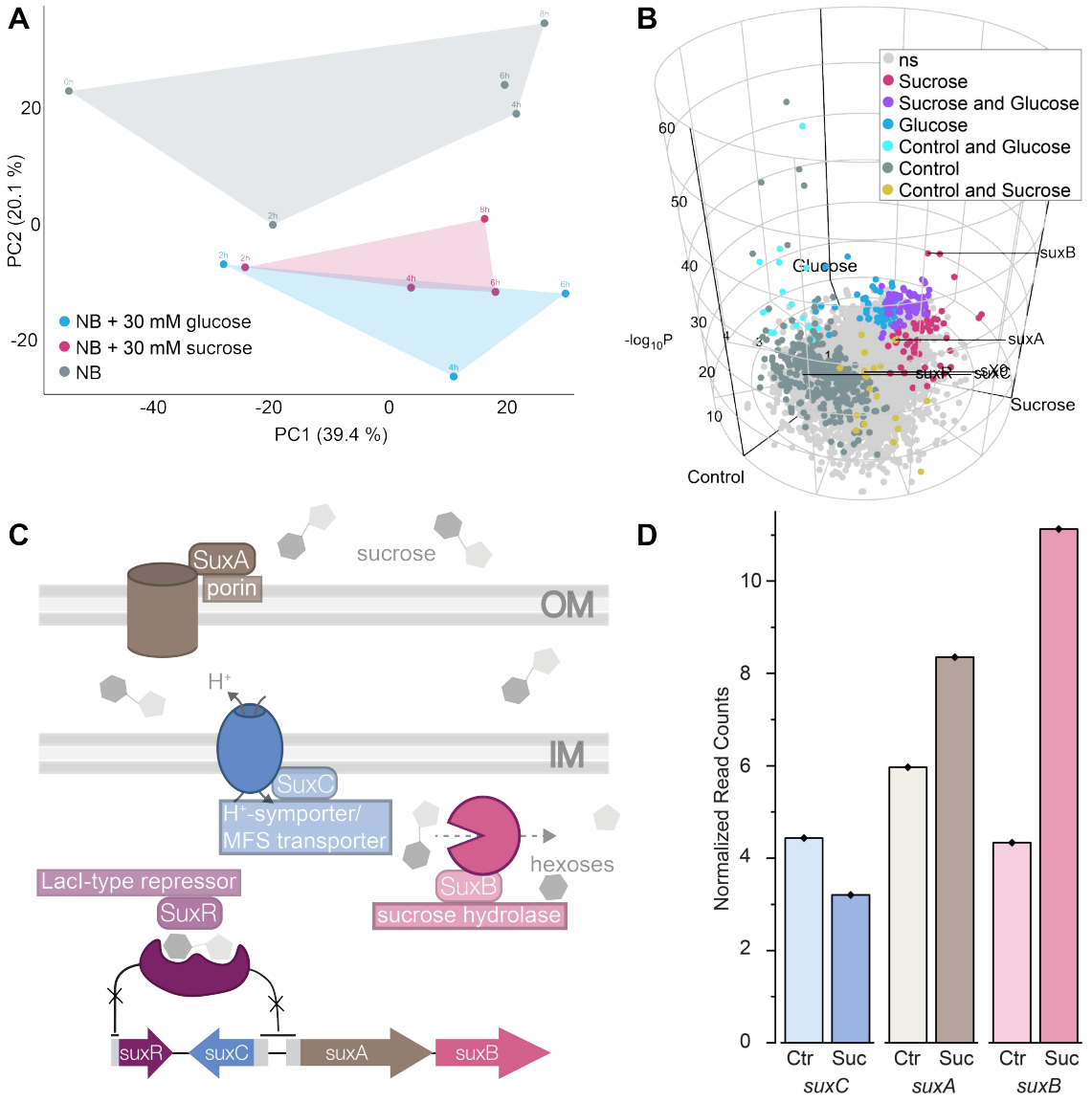

Figure 2.1: Identification of *sux* cluster in *Xoo* by RNAseq. PXO99^{A} cells were grown in NB media with and without supplementation of sugar and were sampled over eight hours for an *in vitro* RNAseq analysis. **A)** The first two principal components explaining the variance between *Xoo* grown in NB (grey), NB + sucrose (pink), and NB + glucose (blue). **B)** RNAseq data of *Xoo* grown for 4 hours in the three media types, where the abundance of each gene is assigned radial coordinates and color based on which treatment has more abundant RNA. The z-axis is the $-\log_{10}$ p-value with a significant $p < 0.01$. **C)** Proposed model of the *sux* cluster-encoded sucrose uptake system in *Xoo*, including a schematic representation of the gene cluster. SuxA (brown): β-barrel outer membrane porin; SuxC (blue): major facilitator superfamily (MFS)-type sucrose/H^+-symporter; SuxB (pink): cytosolic sucrose hydrolase; SuxR (purple): LacI-type transcriptional repressor. **D)** RNAseq read counts for *suxC* (blue), *suxA* (brown), and *suxB* (pink) after 6 hours of growth in media without additional sugar (Ctr) or supplemented with 30 mM sucrose (Suc). Values were normalized to the 0 h time point and the condition without additional sugar.

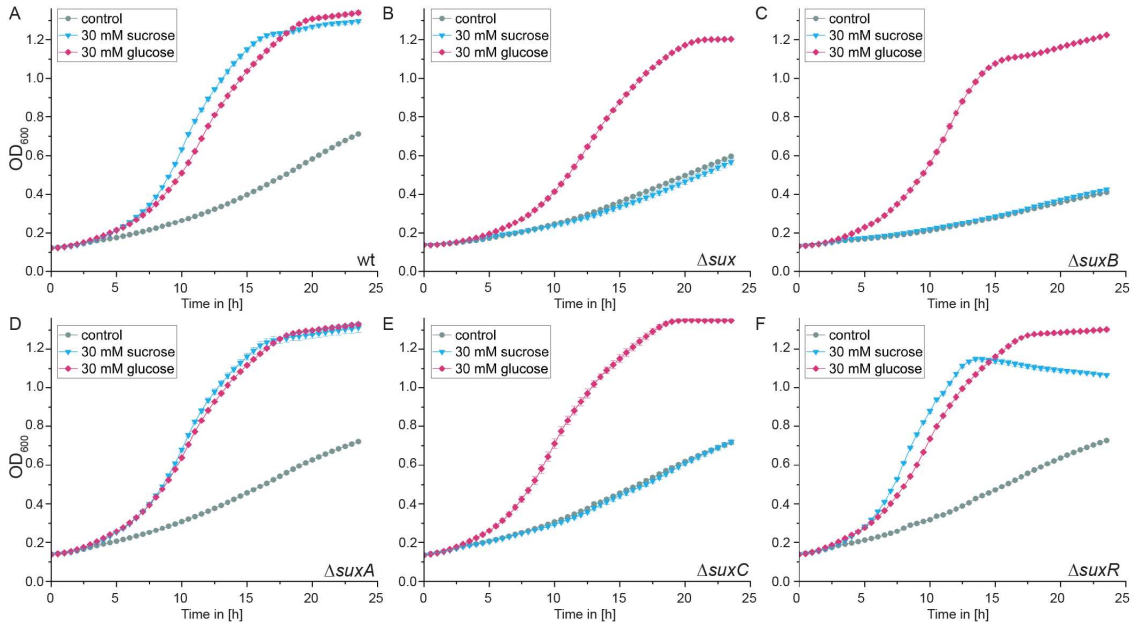

Figure 2.2: Effect of mutations in *sux* genes on bacterial growth. Growth curves of **A)** wildtype, **B)** Δ*sux*, **C)** Δ*suxR*, **D)** Δ*suxC*, **E)** Δ*suxA* and **F)** Δ*suxB* in NB media (grey), supplemented with 30 mM sucrose (blue) or 30 mM glucose (pink). Mean of 3 technical replicates is shown with whiskers for ± SEM.

RNAseq included cytochrome B and NADH-oxidoreductases, both involved in the generation of the proton motive force (PMF), required for example for H^+-symport and thus concentrative sucrose uptake (Supplementary Table 2.2).
Analysis of *sux* gene clusters across 17 *Xanthomonads* revealed sequence identity >85 %. All 17 species, representing the African and Asian continents, with vascular and non-vascular lifestyles retained the *sux* cistron in the same organization (Supplementary Figure 2.7). The cistron thus is a strong candidate for sucrose uptake and metabolism in *Xoo*. Temporal dynamics of transcriptional changes hypothesize a response of *Xoo* to sucrose, represented by the increase of *suxA* and *suxB* transcripts (Figure 2.1d). The induction was sucrose-specific, as *sux* transcript levels remained unresponsive to glucose supplementation or showed a decrease (Supplementary Figure 2.8). Changes in *suxR* transcripts were not observed. The conservation of the *sux* operon indicated a likely evolutionary importance, potentially unveiling a universal host-derived sucrose utilization mechanism in *Xanthomonads*.

SuxB is a sucrose hydrolase

Using KEGG classification, SuxB was a member of family 13 of glycoside hydrolases and was classified as an amylosucrase (E.C. 2.4. 1.4), which either functions as

a glycosyltransferase for synthesizing amylose-like polymers from sucrose or as a sucrose hydrolase. To differentiate between the activities, SuxB was crystallized in its apo state with a resolution of 2.4 Å (Figure 2.3a). Independently produced crystals were soaked with sucrose, but likely due to hydrolytic activity, we identified a glucose molecule in the binding pocket of SuxB (resolution 2.95 Å, (Figure 2.3b). COOT was used to dock sucrose into the binding site based on the position of glucose (Supplementary Figure 2.9). Structural analysis revealed a $(\beta/\alpha)_8$-barrel shape, which distinguishes SuxB from classical invertases with β-propellers linked to C-terminal β-sandwich structure [90, 91]. SuxB lacks three arginine residues that are crucial for the glucosyltransferase activity of amylosucrases [91], indicating that SuxB is a sucrose hydrolase (GH13-4, E.C.3.2.1.48). The SuxB fold from *Xoo* is structurally similar to the sucrose hydrolase SUH_{Xag} from *Xanthomonas axonopodis pv. glycines* [91], with an average RMSD of around 0.6 over circa 535 Cα atoms. In both, the apo and the glucose-complex structure, the asymmetric unit contains three SuxB molecules. When comparing the individual chains within the apo structure, all three SuxB molecules show identical arrangement with their corresponding chains with RMSD values ranging from 0.15 (over 590 Cα atoms, chains A) to 0.23 (over 582 Cα atoms, chains C). The structures differ only slightly for the conformations of the loops in the B and B' domains. When using the Cα atoms of the residues His224 and Ser437 as reference points for describing the high degree of flexibility of the loops 'shielding' the active site (i.e. ∼ aa 221-225, loop between Bα3 and Bβ3; and ∼ aa 435-442, loop between B'β1 and B'β2) it becomes obvious: the distance between these two amino acids amount to 10.2 Å in chain A, to 7.7 Å in chain B and 7.5 Å in chain C in SuxB-apo (Figure 2.3c). Beyond that, parts of these loops are described to not be visible in the electron density of the deposited structures of homologous proteins [91], which also indicates high flexibility in these parts. The accessibility of the active site was evaluated by analyzing the electrostatic surfaces which show the widest opening in chain A and the closest access in chain B in the apo structures. Compared with the SUH_{Xag} structures [91], glucose in SuxB occupied the same position as the glucosyl moiety and the glucose molecule in SUH-E322Q-sucrose (pdb 3CZK) and SUH-glucose (pdb 3CZG) within the active site, with hydrogen bonds to the SuxB active site residues Asp137, His180, Ser281, Glu322, Asp392 and Arg515 (Figure 2.3b). In contrast to the apo structure, all three chains in the SuxB-glucose complex appear to be more 'rigid' or stabilized by the interaction with the glucose, since the loops of the above-described B and B' domains adopt a more similar conformation.

AI prediction models support the hypothesis that SuxB recognizes sucrose and

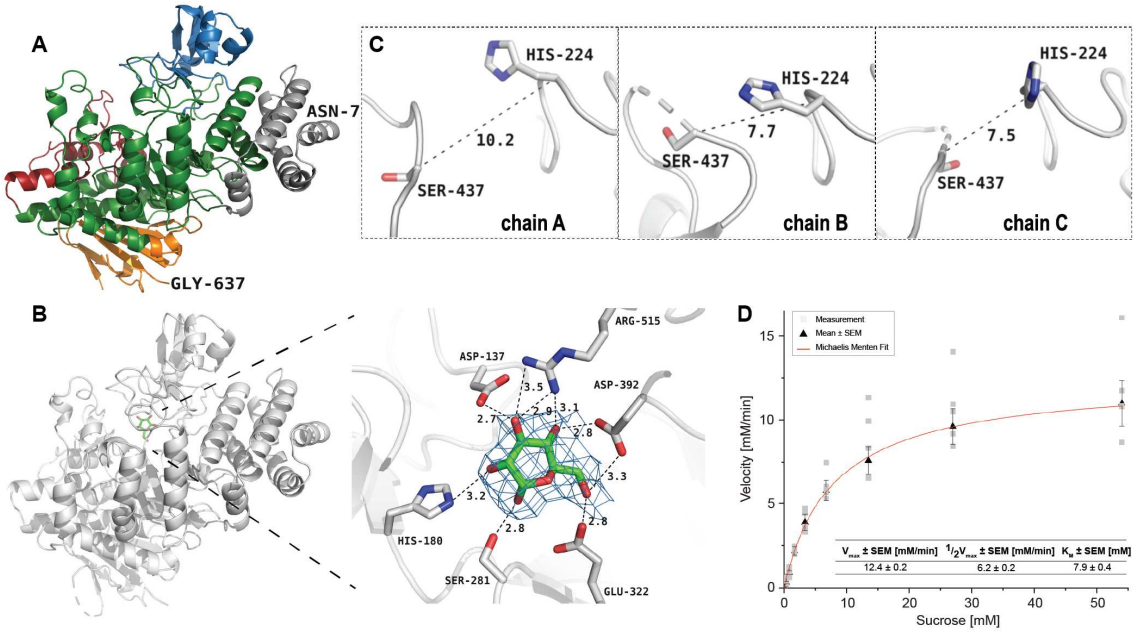

Figure 2.3: Characterization of *Xoo* sucrose hydrolase SuxB. A) Domains N, A, B, B', and C are presented as cartoons accordingly to SUH (Kim et al., 2008) with domain N colored in grey, domain A in green, B in blue, B' in red, and domain C in orange. For clarity, the N- and C-terminal residues Asn7 and Gly637 are labeled. **B)** The dashed box indicates the region of the flexible loops from domains B and B', which are zoomed in. **C)** Overall structure of SuxB in complex with the hydrolase product glucose (left panel) and zoomed in on the active site (right panel). Highlighted are the active site residues that interact with the sugar molecule. The electron density around the bound glucose is contoured at 1 σ. In **A)** and **C)** only chain A is presented. Additional data in supplementary Figure 2.9. **D)** Michaelis-Menten curve of SuxB. Sucrose hydrolysis quantification via DNS assay on 0.1 μg/μL His-tag-purified enzyme in 20 mM MOPS, pH 7, at 28°C. (1/2) Vmax = (half) maximum rate of reaction, K_M = Michaelis constant.

estimate the K_M to 5.5 mM and K_{cat} to 73.4 s^{-1} [92]. To directly test for sucrose hydrolase activity, SuxB was expressed in *E. coli*. Colorimetric DNS (dinitrosalicylic acid) assays detected reduced sugars when sucrose was added (Figure 2.3d). Further analysis revealed Michaelis-Menten kinetics with a K_M of 7.9 mM, similar to the predicted K_M (Figure 2.3d). The identification of SuxB as a sucrose hydrolase strongly supports the hypothesis that the *sux* gene cluster is involved in sucrose utilization by *Xoo*.

De-repression of *sux* genes by sucrose

The transcriptional regulator SuxR exhibits two conserved functional domains from the LacI family of bacterial regulatory proteins including an N-terminal helix-turn-helix DNA binding domain, and a C-terminal ligand binding domain [93]. DNA binding motifs of SuxR were predicted using RegPrecise 3.0 and identified potential

target regions in *PsuxC* and *PsuxAB* (Supplementary Figure 2.10) [94]. Consequently, we hypothesized that the ligand binding domain undergoes a conformational rearrangement upon sugar binding, which allosterically alters the affinity of the regulator to the DNA binding site. Motif analysis indicated that in the absence of sucrose, SuxR acts as a negative regulator (repressor) of the *sux* gene cluster. Regulation of SuxR might be mediated via the sigma factor σ^{54} (RpoN2). Promoter regions of *suxR* and *suxC* showed binding motifs for σ^{54}, although imperfect for suxR [70, 95, 96] (Supplementary Figure 2.10). In *Xoo*, motility, biofilm formation, EPS production, and virulence are controlled by the sigma factor σ^{54} (RpoN2). Based on the presence of the *LacI-type repressor suxR* in the cluster, and the 'induction' or derepression of *sux* genes by sucrose (Figure 2.1d), we surmise that *in vivo*, the transcription activator-like effector (TALe)-induced SWEET activity will trigger release of sucrose that leads to derepression of the *sux* genes.

sux gene functions are necessary for sucrose uptake

To evaluate whether the *sux* genes are required for sucrose utilization, deletion mutants were generated, either removing the whole *sux* gene cluster or deleting individual ORF encoding sequences. Deletion of the entire *sux* cluster (Δsux) abolished sucrose-dependent growth to base levels, while growth rates with or without glucose supplementation remained unaffected (Figure 2.2b). Potential redundancies within the genome of the functions were tested using mutants for the individual genes in the cluster (Supplementary Figure 2.10). The sucrose hydrolase SuxB was essential for sucrose utilization as indicated by a reduction in growth kinetics to base levels (Figure 2.2c). The overall ability of the $\Delta suxB$ mutant was unaffected, as indicated by having comparable growth rates as wildtype controls on media supplemented with glucose (Figure 2.2c). SuxB is located downstream of SuxA, which is likely the porin responsible for the first step in sucrose uptake across the outer membrane (Figure 2.1c). In contrast to the effect of $\Delta suxB$ on sucrose utilization, $\Delta suxA$ mutants did not show differences in growth kinetics when grown with sucrose or glucose (Figure 2.2d). The well-established redundancy and overlapping substrate specificities of outer membrane porins or compensation might be possible explanations for the maintenance of sucrose transport across the outer membrane in the deletion mutant [40, 97, 98]. Similar to $\Delta suxB$, the MFS transporter mutant $\Delta suxC$ was unable to grow on media supplemented with sucrose but was characterized by similar growth rates as the wildtype in the presence of glucose (Figure 2.2e). We did not expect that $\Delta suxR$ would impair sucrose utilization.

Consistent with this hypothesis, Δ*suxR* was apparently unaffected and grew similar as wildtype (Figure 2.2f). In summary, the results of the growth analysis of individual cluster components supported our hypothesis that sucrose uptake is facilitated by the *sux* cluster. Key players for sucrose uptake are *suxC* and *suxB*. Notably, glucose can act as an alternative carbon source to sucrose at least *in vitro*.

Sucrose is necessary for EPS production and biofilm formation

Sucrose can be acquired via the *sux* gene cluster and serves as a carbon and energy source for reproduction. Carbon skeletons and energy are also required for biofilm production and to energize motility. Colony morphology can reveal deficiencies in EPS production and motility features. Phenotypic comparison with the wildtype revealed smaller colony diameters for Δ*sux*, Δ*suxC*, and Δ*suxB* on media containing sucrose (Supplementary Figure 2.11). Colony size on media without sucrose showed no difference from wildtype. Notably, Δ*sux*, Δ*suxC*, and Δ*suxB* mutants appeared drier and flatter compared to wildtype on sucrose-supplemented media (Supplementary Figure 2.11). Δ*suxA*, lacking the outer membrane porin, did not show obvious deficiencies, as observed in the growth assays above (Figure 2.3d). Supplementation with glucose rescued the morphology defects to wildtype levels (Supplementary Figure 2.11). We hypothesize that *sux*-mediated uptake and metabolization by SuxB provides glucose as a precursor for EPS biosynthesis and biofilm formation. 'Hanging drop' assays on inverted plates containing sucrose showed that wildtype colonies slowly followed gravity in the form of a hanging drop, which eventually disintegrated, while Δ*sux* colonies stayed relatively flat (Figure 2.4a). Quantification of EPS by crystal violet staining showed a significant reduction in crystal violet staining between Δ*sux* and wildtype cultures (Figure 2.4b,c). The qualitative and quantitative data support the hypothesis that sucrose utilization in *Xoo* via the *sux* cluster is necessary for EPS production and biofilm formation, key factors required for virulence.

sux gene functions are necessary for swimming and swarming

We hypothesize that sucrose may also provide the energy required for motility during the progressive infection of the xylem against the stream direction. The energy demand for motility is primarily provided by PMF [99]. *Xoo* transitions from planktonic to sessile lifestyle, marked by a shift from swimming to swarming. Swimming and swarming of Δ*sux* was significantly reduced relative to wildtype

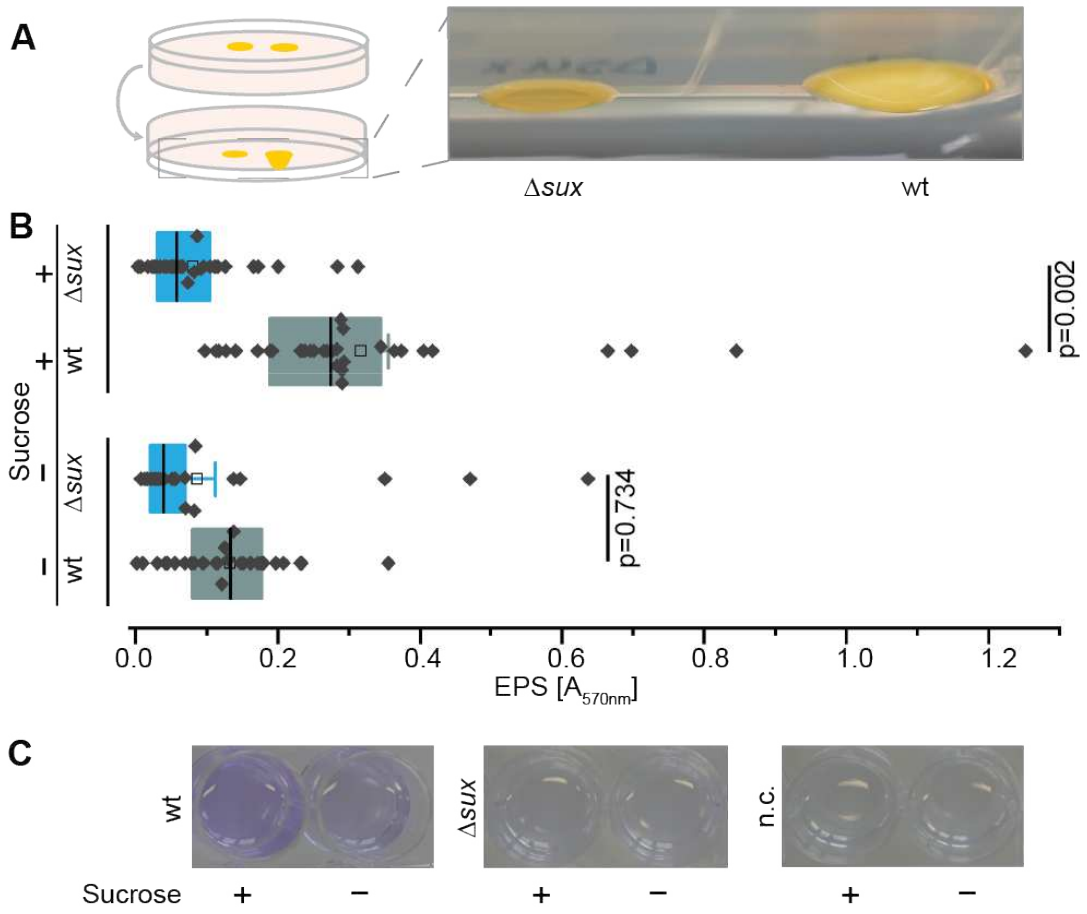

Figure 2.4: Effect of *sux* genes on EPS production and biofilm formation. **A)** Qualitative analysis of biofilm formation by inverted plates following the hanging droplet assay. Supplementary Figure 2.11 shows effects on glucose-supplemented media. **B)** Quantification of crystal violet from wildtype and Δ*sux* cells in NB media ± 30 mM sucrose supply. Boxes range from 25th to 75th percentiles with median values shown as center lines and mean values as empty boxes with whiskers ± SEM. Significance between two groups was calculated using unpaired two-tailed Student's t-test with 95 % confidence. **C)** Crystal violet staining of wildtype, Δ*sux* and negative control (no cells) in NB media ± 30 mM sucrose supply.

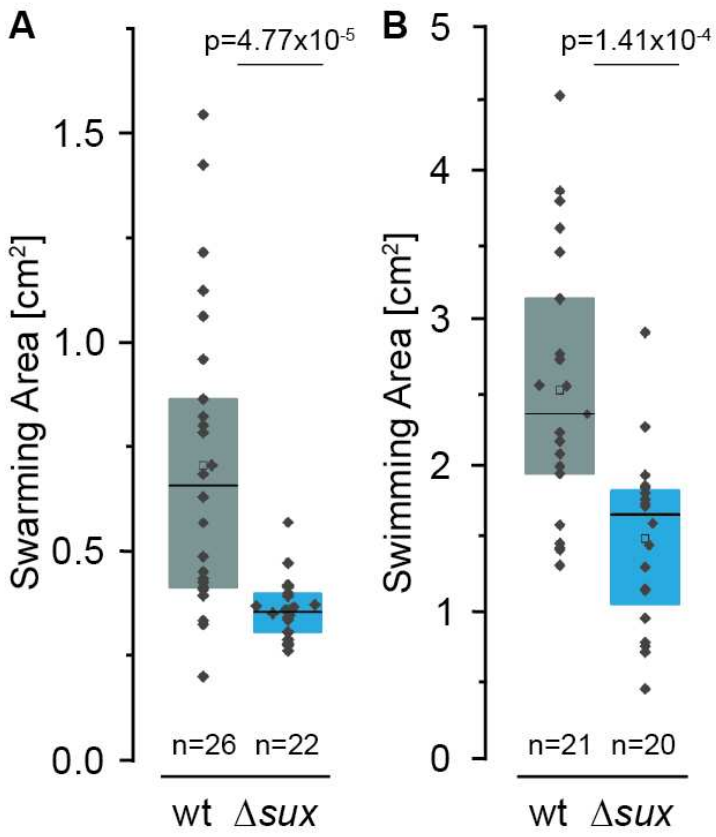

Figure 2.5: Role of *sux* genes in *Xoo* motility. Quantification of **A)** swarming area on 0.6 % agar plates and B) swimming area on 0.3 % agar plates of Δ*sux* mutants (blue) compared to wildtype (grey). Boxes range from 25th to 75th percentiles with median values shown as center lines and mean values as empty boxes with whiskers ± SEM. Significance between two groups was calculated using unpaired two-tailed Student's t-test with 95 % confidence.

(Figure 2.5a,b). Together, our findings indicated that *sux*-mediated sucrose uptake drives motility in *Xoo*, likely by increased PMF generation.

Sux proteins are required for full pathogenicity

While the *in vitro* studies support a role of the *sux* gene cluster for sucrose uptake and virulence factor activity, a key question was whether the *sux* genes are also critical for successful infection of rice. To test for roles in virulence, three diverse rice cultivars, *Oryza sativa* ssp. *japonica cv. Nipponbare*, *cv. Kitaake*, and *Oryza sativa* ssp. *indica cv. IR24* were infected with the *sux* mutants using clipping assays [88]. Notably, virulence was significantly decreased in all three rice varieties (Figure 2.6a-d). Analyses of the contribution of the individual *sux* genes showed that while Δ*suxA* was only slightly impaired, possibly due to TBDR redundancy, Δ*suxC* and Δ*suxB*

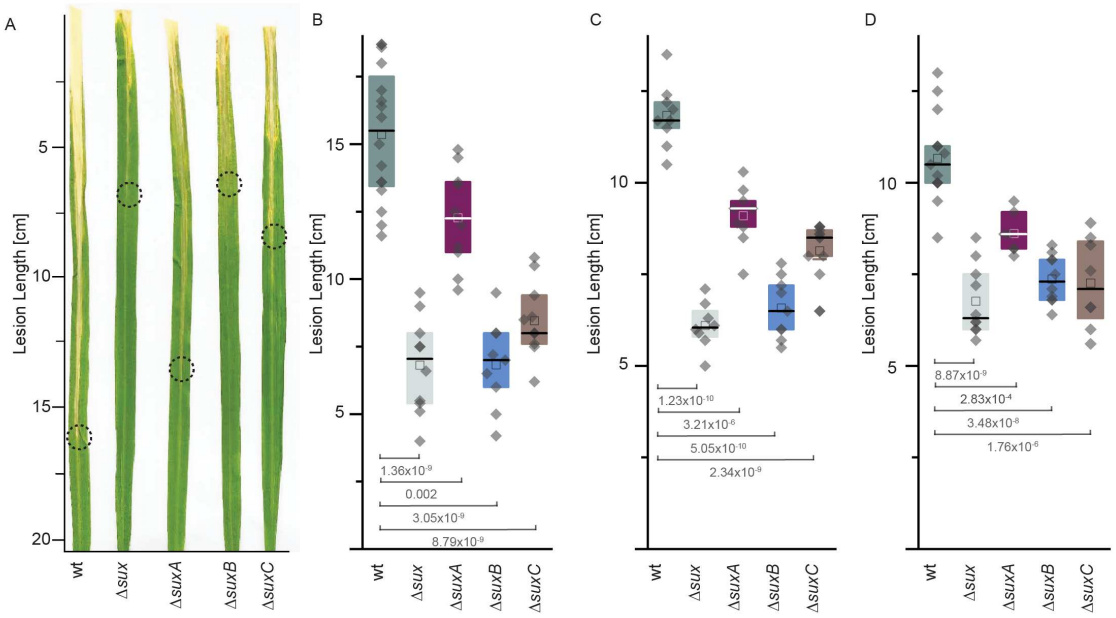

Figure 2.6: Impact of *sux* genes on *Xoo* virulence in rice bacterial blight. **A)** Representative leaf phenotypes in rice cultivar *Nipponbare* 12 days after infection with PXO99^{A} and *sux* mutants. **B-D)** Quantification of lesion length in rice cultivar **B)** *Nipponbare* (n=9-12), **C)** *Kitaake* (n=8-13), and **D)** *IR24* (n=7-15). Boxes range from 25th to 75th percentiles with median values shown as center lines and mean values as empty boxes with whiskers ± 1 SEM. Significance between two groups was calculated using unpaired two-tailed Student's t-test with 95 % confidence.

mutants exhibited significantly reduced virulence (Figure 2.6a-d). Thus, the *sux* genes of *Xoo* play more critical roles for virulence than in *Xanthomonas axonopodis pv. glycines*, for which *suxB* mutation showed only moderate effects on virulence in soybean, or *Xanthomonas campestris pv. campestris*, where *sux* mutations only lead to a delay in symptom development on Arabidopsis [39, 40]. Notably, the *sux* genes of *Xanthomonas axonopodis pv. manihotis* were not required for virulence in cassava [84]. In summary, the *sux* genes of *Xoo* play a pivotal role in full virulence, linking *Xoo*-mediated transcription of the host *SWEET* transporters to SuxR-mediated derepression of a suite of *sux* genes crucial for uptake and utilization of sucrose, required for carbon and energy supply, as well as motility and adhesion.

2.4 Discussion

The dependency of *Xoo* virulence on TALe-mediated induction of a subfamily of sucrose-transporting *SWEETs* by *Xoo*, together with the uniport mechanism of SWEETs, and the low abundance of sucrose in the xylem of uninfected rice may intimate that the ability of *Xoo* to colonize the xylem depends critically on sucrose supply. Here, we identified the *sux* cistron as an essential cluster of genes required for sucrose uptake and utilization in *Xoo*. Importantly, the *sux* gene cluster is required for virulence, and *sux* mutants can cause only low levels of disease, indicating that sucrose is a key limiting factor for successful colonization.

Xoo likely uses carbon sources other than sucrose while living outside a plant, as well as in early stages of infection of the plant, when sucrose is not present and the *sux* genes are repressed. We hypothesize that upon release of sucrose due to induction of *SWEETs*, *sux* genes are derepressed, enabling the bacteria to acquire and metabolize sucrose. The key components of the cistron include a LacI-type repressor SuxR, and sucrose induction of the *sux* genes supports a sucrose-dependent derepression of the genes. As a γ-proteobacterium, *Xoo* has to take up nutrients across the outer and inner membranes. The porin-like SuxA likely mediates uptake across the outer membrane. However, Δ*suxA* mutants could still grow on media with sucrose, and virulence was only partially inhibited. Other porins either compensate or can mediate sufficient uptake of sucrose across the outer membrane [40]. In contrast, the MFS-family transporter SuxC, which likely functions as a secondary active H^+-symporter on the inner membrane, was essential for growth on sucrose-containing media and showed a similar reduction in virulence as mutants carrying deletions of the complete gene cluster. At the same time, sucrose triggers an increase in transcripts for proteins involved in generating the PMF, namely Cytochrome B and NADH-oxidoreductases, required for H^+-symport and thus concentrative sucrose uptake.

The fourth gene in the *sux* gene cluster, *suxB*, encodes a protein annotated as amylosucrase, so an enzyme that can hydrolytically cleave sucrose and synthesize amylose-like polymers from sucrose. Analysis of crystal structures supports the hypothesis for hydrolysis activity based on the apo-, glucose-bound, as well as modelled sucrose-bound structures. The active site of SuxB is similar to in the SUH protein from *Xag*, and the binding site for the fructosyl and glucosyl moieties corresponds to the +1 and –1 subsites, respectively [100]. Three arginine residues were crucial for glucosyltransferase activity of amylosucrases of *Neisseria* [39]. Mutant forms of the sucrose hydrolase from *Xag* failed to restore glucosyltransferase activity [91]. The arginine residues are not conserved in SuxB from *Xoo*, strongly supporting a sole function as sucrose hydrolase. Kinetic analysis shows that SuxB has a K_M of 7.9.

If we assume that the K_M is indicative of the sucrose levels, and given the potential dilution by the xylem flow, the value appears relatively high, at least in early phases where single *Xoo* cells inject TALes to trigger sucrose efflux. H^+-symport by SuxC may enable concentrative sucrose uptake at very low supply levels. The phenotypical analysis of the mutants demonstrates that sucrose utilization is critical for growth as well as motility, EPS production, and biofilm formation. In summary, the data support a role of the *sux* gene cluster as the key uptake and utilization system for *Xoo*. Notably, the mutation of the *sux* gene cluster leads to a significant reduction in virulence. Natural infections are initiated by a single or a few bacterial cells that multiply and cause disease. In contrast, virulence assays using the clipping method rely on high bacterial titers for inoculation, which may not reflect natural infection dynamics [101]. The residual virulence observed in this study may therefore not be relevant under natural conditions. Nevertheless, the $PXO99^A$ strain lacking the TALe *PthXo1*, which induces *SWEET11a*, is avirulent [10]. While *sux* mutants exhibit substantially reduced virulence, their ability to sustain a low level of pathogenicity indicates that alternative carbon sources might compensate. SWEET-derived sucrose may also be hydrolyzed in part by secreted host cell wall invertases, e.g., *OsCIN1, OsCIN4,* and *OsCIN7*, for which transcript levels increase during *Xoo* infection [102].

Potential relevance of the role of nutrient supply beyond BB

γ-proteobacteria, a class of the proteobacteria to which *Xanthomonads* belong, includes many important pathogens, e.g. *Yersinia*, *Escherichia* or *Legionella*, that cause disease in animals and humans; or the genus *Xanthomonas*, comprising many pathogenic bacteria causing disease on a wide spectrum of plants and *Pseudomonas*, which can infect animals and plants or be beneficial [103]. Notably, many bacterial genera, including γ-proteobacteria, can cause disease in animals and plants, e.g., *Salmonella*, *Shigella*, *Enterobacter*, *Enterococcus*, *Pantoea*, *Burkholderia*, *Rhizobium* or *Pseudomonas*. *Xanthomonads* are predominantly known as plant pathogens causing diverse diseases across a wide range of plants and including major crop diseases. There are indications that *Xanthomonas* has been found in human blood and nosocomial patients have been found. The identification of disease mechanisms and fundamental dependencies of *Xanthomonads* may have relevance beyond a single species, such as *Xoo* here, but possibly across multiple species and possibly other genera within the γ-proteobacteria. Notably, the TALe-mediated induction of *SWEETs*, found originally in *Xoo*, also appears also to be important for cotton and cassava blight [84, 104]. We surmise that pathogens infect hosts primarily to gain

access to the host's nutrient pool as an essential prerequisite for reproduction, as well as a source of energy for virulence-related functions. Genome editing has enabled the development of resistant varieties, and regulatory pipelines have been implemented to assess performance and transgene/foreign DNA elimination by segregation in accordance with national biosafety standards [2]. Such tools lay the groundwork for future crop protection strategies. Combined with a comparative characterization of the metabolic functions that relate to virulence may provide new ways to protect hosts from infections or cure diseases.

Supplementary

Table 2.1: Genes in the *sux* locus of PXO99[A]

Locus ID	Protein ID	Gene name	Protein name	Putative function
PXO_02412	ACD60701.1	*suxR*	SuxR	LacI type HDH* domain transcriptional regulator
PXO_02413	ACD60702.1	*suxC*	SuxC	Inner membrane MFS**-type sugar transporter
PXO_02415	ACD60703.1	*suxA*	SuxA	TonB-dependent receptor, β-barrel outer membrane transporter
PXO_02416	ACD60704.1	*suxB*	SuxB	amylosucrase, sucrose hydrolase***

* Helix-Turn-Helix

** Major Facilitator Superfamily

*** Glycoside Hydrolase Family 13

Table 2.2: RNAseq PMF candidates.

Gene ID	Gene ID (RS)	log2Fold Change	p-value	padj	Gene description
PXO03768	PXORS02020	2.53	0.041	0.995	NADH oxidase
PXO01688	PXORS14615	2.92	0.025	0.995	Cytochrome b

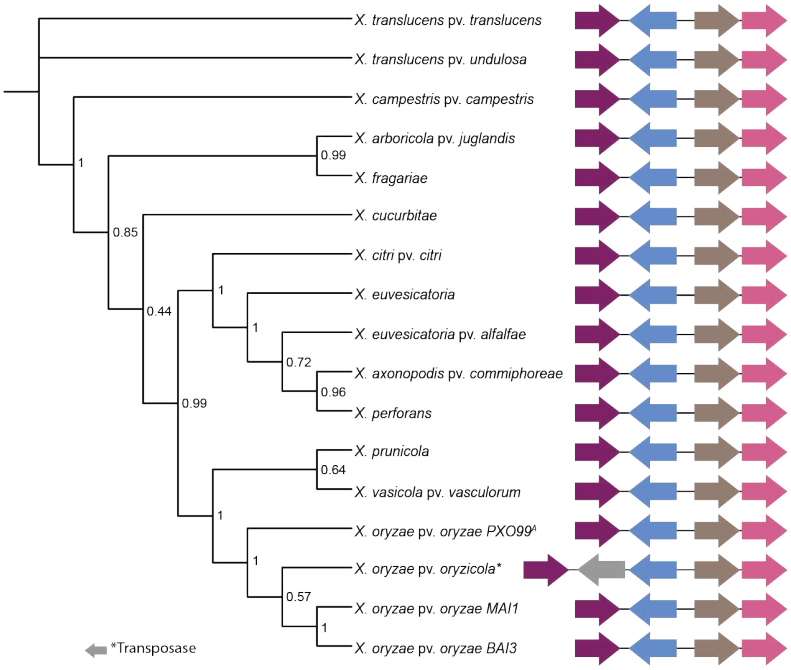

Figure 2.7: Phylogenetic tree of *sux* cluster in *Xanthomonas* species. Homologous genes based on *Xoo* PXO99^{A}'s *sux* cluster. The analysis spans 17 *Xanthomonas* species from strains of the African and Asian continents with vascular and non-vascular lifestyles. Depiction of conserved cluster structure with *suxR* (purple), *suxC* (blue), *suxA* (brown), and *suxB* (pink), as well as an identified transposase gene (grey) in *Xoc*. Phylogenetic confidence given by bootstrap values at nodes.

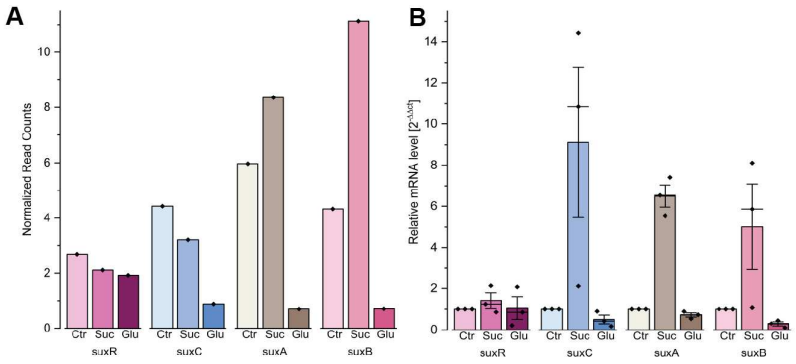

Figure 2.8: Transcriptomic analysis of the *sux* cluster. Transcriptomic analysis of all *sux* gene mRNA levels. Cells were grown in NB media without added sugar (Ctr) or with 30 mM sucrose (Suc) or glucose (Glu). **A)** Read counts from the 6h time point of the RNAseq data set were normalized to the untreated condition and 0h time point. The trends were compared to **B)** qRT-PCR results of the 6h time point. Normalization based on $2^{-\Delta\Delta}$ct method by [87]. Display of three data points from two independent experiments. Bar height represents mean, horizontal line represents median, error bars display ± SEM.

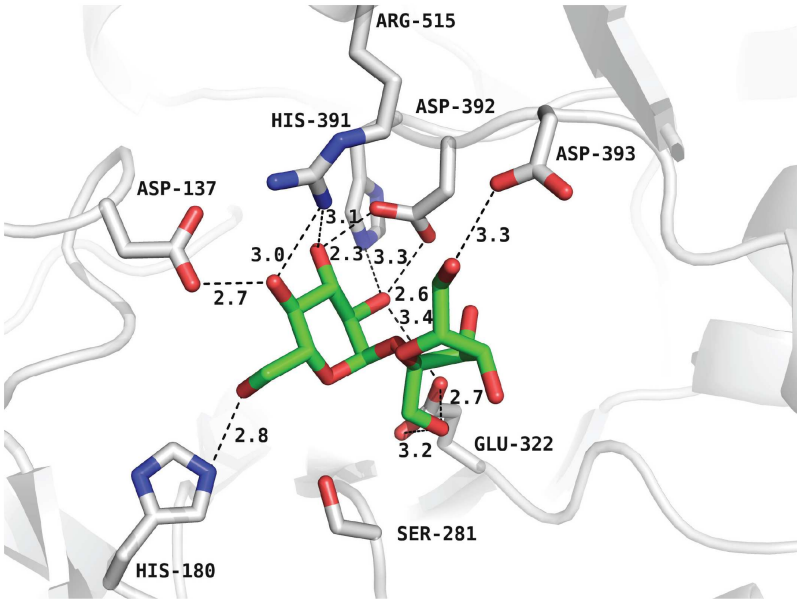

Figure 2.9: Sucrose binding site of SuxB (glucose-bound structure PDB: 9R9L). Zoom in to the active site of SuxB with a sucrose molecule fitted in manually using COOT and the position of the glucose molecule as anker point. The glucose moiety is bound via interactions with the side chains of Asp137, His180, His391, Asp392 and Arg515, whereas the fructose moiety interacts with Glu322 and Asp393.

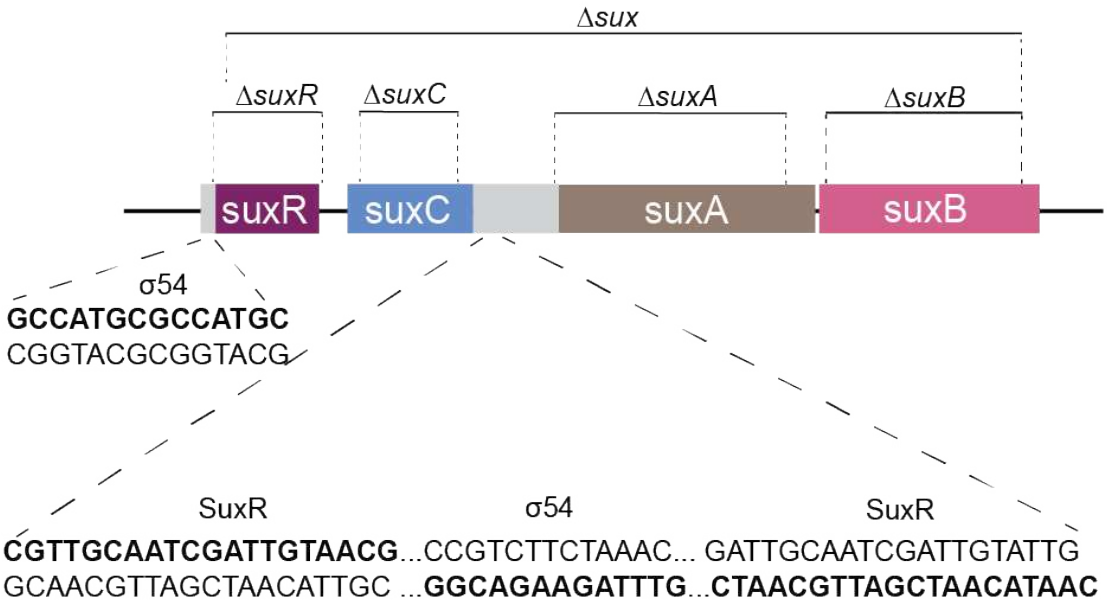

Figure 2.10: Mutants used in this study and binding motifs. *Sux* cluster structure with marked regions (dotted lines), which were replaced by a spectinomycin cassette during mutant generation. Promoter regions are colored in grey, *suxR* in purple, *suxC* in blue, *suxA* in brown, and *suxB* in pink. Putative binding sites for σ^{54} transcription factor and SuxR are highlighted and bolded for strand specificity.

Table 2.3: Data collection and refinement statistics.

	SuxB apo	**SuxB glucose**
Data collection	ESRF, ID23-2	DESY, EMBL; P13
	25.01.2025	22.03.2025
Wavelength [Å]	0.873130	1.059700
Resolution range [Å]	46.98 - 2.40 (2.49 - 2.40)	49.75 - 2.95 (3.06 - 2.95)
Space group	I 2 2 2	I 2 2 2
Unit cell [Å, °]	98.754 175.959 258.335	100.535 172.726 259.777
	90 90 90	90 90 90
Total reflections	175616 (17385)	632095 (63699)
Unique reflections	88004 (8702)	47939 (4747)
Multiplicity	2.0 (2.0)	13.2 (13.4)
Completeness (%)	1.00 (1.00)	1.00 (1.00)
Mean I/sigma (I)	7.95 (1.75)	11.07 (1.65)
Wilson B-factor [Å^2]	33.76	91.52
R-merge	0.08 (0.41)	0.13 (1.39)
CC1/2	0.99 (0.72)	1.00 (0.88)
CC*	1.00 (0.92)	1.00 (0.97)
Reflections used in refinement	87997 (8700)	47909 (4744)
Reflections used for R-free	4418 (443)	2465 (272)
R-work	0.17 (0.23)	0.24 (0.47)
R-free	0.23 (0.31)	0.30 (0.51)
CC (work)	0.97 (0.90)	0.93 (0.12)
CC (free)	0.94 (0.76)	0.92 (0.10)
Number of non-hydrogen atoms	15377	14527
macromolecules	14483	14484
Ligands	154	38
Protein residues	1861	1864
RMS (bonds)	0.01	0.01
RMS (angles)	1.26	1.26
Ramachandran favored (%)	97.40	94.00
Ramachandran allowed (%)	2.49	5.35
Ramachandran outliers (%)	0.11	0.65
Rotamer outliers (%)	0.07	12.00
Clashscore	7.16	7.98
Average B-factor	41.05	118.92
macromolecules	41.08	118.97
ligands	50.98	105.31
solvent	38.50	83.12
PDB code	9R8I	9R9L

Statistics for the overall data quality and for the highest-resolution shell are shown in parentheses.

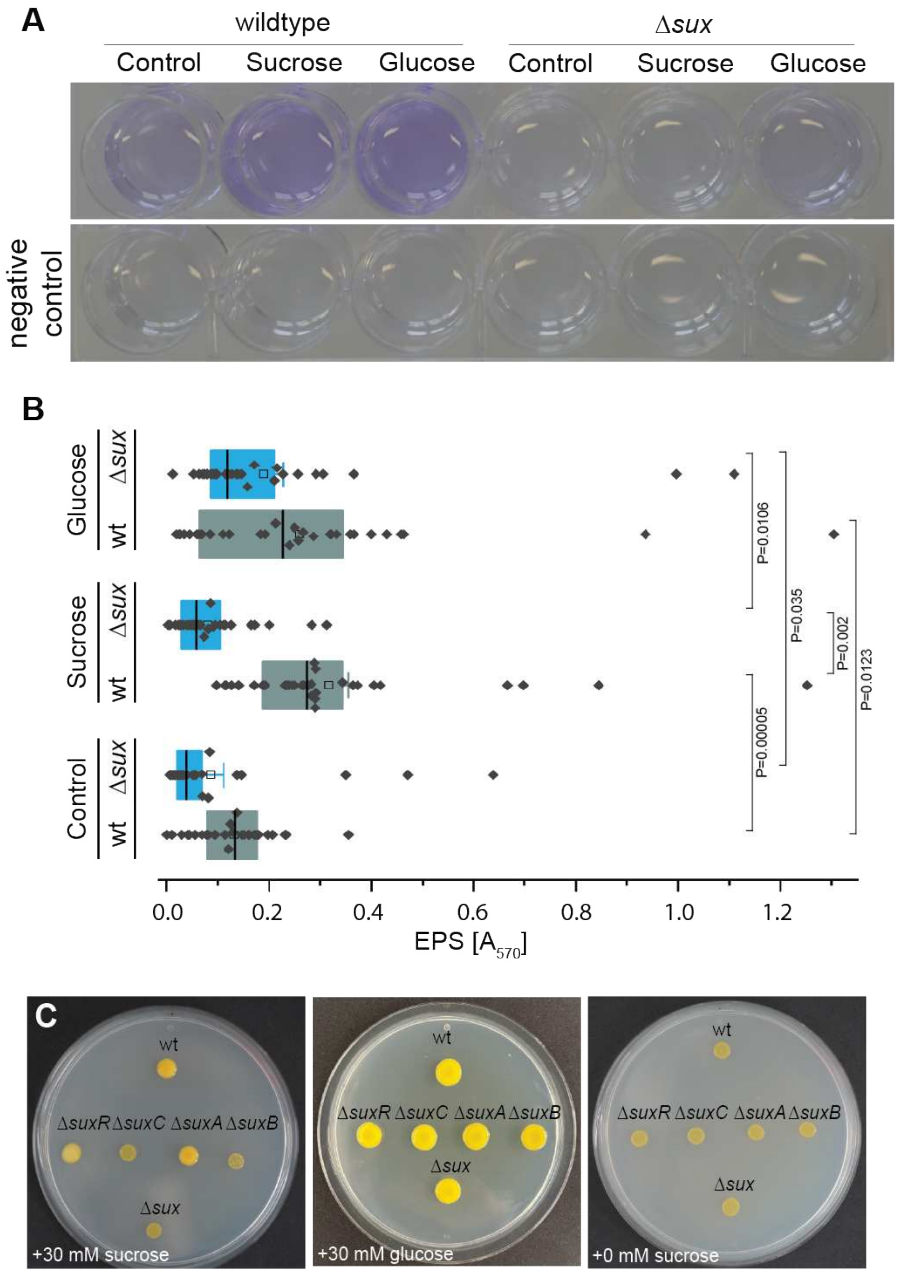

Figure 2.11: Role of *sux* genes for EPS production and biofilm formation in glucose supplemented media. A) Crystal violet staining of wildtype, Δ*sux* and negative control (no cells) in NB media ± 30 mM sucrose or glucose supply **B)** Quantification of crystal violet from wildtype and Δ*sux* in NB media ± 30 mM sucrose or glucose supply. Boxes range from 25th to 75th percentiles with median values shown as center lines and mean values as empty boxes with whiskers ± SEM. Significance between two groups was calculated using unpaired two-tailed Student's t-test with 95 % confidence. P-values given for significant results. **C)** Representative colony phenotypes of wt and *sux* mutants in NB media supplemented with 30 mM sucrose, 30 mM glucose or without sugar supplementation.

Acknowledgments

We thank Susanne Paradies for excellent technical assistance. We would like to thank Boris Szurek for advice on *Xoo* transformation. We would like to thank Eduardo Patriarca (CNR-IGB, Naples, Italy) for the 'hanging droplet assay'. This work was supported by grants from Deutsche Forschungsgemeinschaft (DFG, German Research Foundation) - Collaborative Research Center SFB1535, project ID 458090666/CRC1535/1; Deutsche Forschungsgemeinschaft (DFG, German Research Foundation) under Germany's Excellence Strategy – EXC-2048/1 – project ID 390686111, Bill and Melinda Gates Foundation to HHU (WBF), with a subcontract to MU (BY) (INV-008733, INV-063189); and the Alexander von Humboldt Professorship. The Center for Structural Studies is funded by the Deutsche Forschungsgemeinschaft (DFG Grant number 417919780, INST 208/740-1 FUGG, INST 208/868-1 FUGG and INST 208/761-1 FUGG) and Deutsche Forschungsgemeinschaft (DFG, German Research Foundation) – SFB1535 - Project ID 458090666 Project Z01 (SHJS & WBF).

CHAPTER 3

Sucrose uptake and metabolism via dual-localized SuxB[2]

2: This manuscript is currently *in preparation.*

Contributions of Nora R. Zöllner: The research described in this chapter, as well as the writing of the chapter, were entirely carried out by Nora R. Zöllner.

3.1 Introduction

During plant–pathogen interactions, competition for host-derived carbon sources is a central determinant of disease outcome [13, 23]. Both host and pathogen actively manipulate sugar metabolism and signaling networks to gain a competitive advantage. The host restricts sugar efflux and modulates pathogen perception to prevent the activation of virulence, while bacterial pathogens suppress immune signaling to evade host defense and secure access to nutrients [12, 105, 106].

In *Xoo*, central components in the metabolic "tug-of-war" include sucrose-hydrolyzing enzymes and the activation of secretion systems - in particular the type II (T2SS) and the type III secretion system (T3SS) [107]. The T2SS exports cell wall–degrading enzymes (CWDEs) and cell wall invertases (CWIVs) in a two-step process. First, the enzymes are translocated into the periplasm via either the general secretory (Sec) or the twin-arginine translocation (Tat) pathway [108]. Subsequently, the T2SS transports the enzymes into the apoplast [24]. Mass spectrometry analysis of T2SS-secreted proteins has identified the most prominent enzymes as cellulase (ClsA), lipase/esterase (LipA), and cellobiosidase (CbsA) [107, 109].

Degradation products generated by CWDEs and CWIVs can trigger host immune responses. However, these responses can be suppressed in a T3SS-dependent manner. For example, apoplasmic monosaccharides such as xylose and galactose induce transcription of *hrp* genes, which promote T3SS assembly and the secretion of transcription activator-like (TAL) effectors [107]. The TAL effectors, in turn, activate transcription of clade III *SWEET* sucrose transporters in the host, redirecting apoplasmic sucrose toward the pathogen [27, 110]. Hosts respond by reinforcing a pathogen-starvation strategy: elevated apoplasmic sugar concentrations trigger the expression of host CWIVs such as *Os*CIN1, *Os*CIN4, and *Os*CIN7, or hexose/H^+ symporters like *At*STP13. These components likely hydrolyze and reimport sugars, thereby restricting the pathogen's access [13, 102].

In this study, we identify SuxB as a sucrose hydrolase that is hypothesized to localize to both the intracellular and the extracellular space, depending on nutrient availability. We hypothesize that this dual localization enables SuxB to complement the host's pathogen-starvation strategy by hydrolyzing sucrose in both compartments. A comparable mechanism exists in the yeast *Saccharomyces cerevisiae*, where the invertase SUC2 remains cytosolic under high-glucose conditions but is secreted when extracellular sugar levels are low. In yeast, this transcriptional flexibility is discussed in the context of microbial game theory, where enzyme secretion becomes advantageous under cooperative conditions [111, 112].

Bacteria employ several mechanisms to achieve transcriptional flexibility, including the regulation of transcription termination. One example is Rho-independent transcription termination, in which a GC-rich palindromic region (dyad symmetry) followed by a uracil-rich tract forms a stem-loop structure in the nascent RNA [113]. This secondary structure stalls the RNA polymerase, and the weak RNA–DNA hybrid at the U-rich sequence destabilizes the transcription complex. The polymerase dissociates from the DNA and the transcription is terminated. Hairpins, which are not followed by U-rich tracts cause stalling but allow transcription to continue due to the stability of the RNA–DNA hybrid. A special case of intrinsic termination is the attenuation. Attenuation is a transcriptional regulatory mechanism first described for the *trp* operon of *E. coli* [114]. The *trp* operon is regulated by two distinct hairpins formed from four sequence domains. Depending on tryptophan availability, these structures either stall or terminate transcription. A similar attenuation-like mechanism may serve as a regulatory model for the dual localization of the two SuxB isoforms as two hairpins were found that encode binding regions for the small regulatory RNA sx9.

3.2 Methods

Molecular cloning

Isolation of genomic DNA from *Xoo* Genomic DNA (gDNA) of *Xoo* was isolated following the DNeasy Blood and Tissue Kit (Qiagen, 69504). *Xoo* was grown in NB media (1 g/L yeast extract, 3 g/L beef extract, 5 g/L peptone, pH 7) at 28°C for 16 hours. 0.5 to 1 mL culture was harvested by centrifugation for 10 min at 7500 x *g* at 22°C. The supernatant was discarded and the pellet resuspended in 180 μL ATL buffer before adding 20 μL proteinase K. The sample was mixed thoroughly by vortexing before incubating in a shaking incubator for 1 hour at 56°C with 700 rpm. After protein degradation, the sample was vortexed and 200 μL of preheated (56°C) AL buffer was added. The sample was vortexed again to ensure thorough mixing. To precipitate genomic DNA, 200 μL 96% ethanol was added and mixed. 650 μL of sample (including precipitate) was transferred into a DNeasy Mini Spin column, placed in a 2 mL collection tube. The sample was centrifuged for 1 min at 8000 x *g* at 22°C. The flow-through and collection tubes were discarded. Two washing steps were performed - first with 500 μL of AW1 buffer followed by centrifugation for 1 min at 8000 x *g* at 22°C. The flow-through and collection tube were discarded and 500 μL of AW2 buffer was added to the column as a second wash step. Tubes were centrifuged for 3 min at 14000 x *g* and 22°C to dry the membrane. The column was placed into a centrifuge tube. To elute the gDNA, 20 μL of AE buffer was pipetted directly onto the membrane, incubated at 22°C for 1 minute and centrifuged for 1 min at 8000 x *g* and 22°C. The elution step was repeated with another 20 μL of AE buffer to increase the elution. Purity and concentration were determined on a photo spectrometer at the absorbance of 260/280 nm and 260/230 nm. gDNA was stored at 4°C.

Isolation of plasmid DNA Plasmid DNA was isolated following the NucleoSpin Plasmid Kit (Macherey-Nagel, # 740588.250). 2 mL overnight culture was harvested by centrifuging for 30 seconds at 11000 x *g* and 22°C. The supernatant was discarded. For cell lysis, the pellet was resuspended in 250 μL of A1 buffer before 250 μL of A2 buffer was added. The tube was inverted 6 to 8 times and kept at 22°C for 5 minutes. 300 μL of A3 buffer was added and the tube inverted. When the sample turned colorless, the lysate was centrifuged for 5 minutes at 11000 x *g* at 22°C. The supernatant was pipetted onto a NucleoSpin column and spun for 1 minute at 11000 x *g* at 22°C. When all lysate was loaded onto the membrane, 500 μL AW buffer was

Table 3.1: PCR master mix for gDNA template

Reagent	Volume	Final
CloneAmp Premix	12.5 μL	1x
Primer F (5 μM)	1 μL	0.2-0.3 μM
Primer R (5 μM)	1 μL	0.2-0.3 μM
gDNA	1 μL	(10-20 ng/μL)
H_2O	9.5 μL	
Total	25 μL	

added to wash the DNA. The sample was centrifuged and 600 μL A4 buffer was added. The sample was centrifuged for 1 minute at 11000 x *g* and 22°C. The membrane was dried by centrifugation for 2 minutes at 11000 x *g* and 22°C. Pre-heated (70°C) AE buffer or water was pipetted onto the membrane and incubated at 22°C for at least 1 minute to enhance the yield during elution. Centrifugation for 1 minute at 11000 x *g* and 22°C was followed by a second elution step. Plasmid DNA was stored at -20°C.

Polymerase chain reaction To amplify gDNA from *Xoo* CloneAmp HiFi PCR Premix (Takara, 639298) was used. 10 to 20 ng/μL gave the best results. The following master mix (see Table 3.1) was prepared and run for 30 cycles (see Table 3.2).

Table 3.2: PCR program for gDNA template

Temperature	Time	Cycles
94°C	60 sec	
98°C	10 sec	
X°C	5 sec	**×30**
72°C	5 sec/kb	
20°C	hold	

PCR clean-up PCR clean-up was performed with the NucleoSpin Gel and PCR Clean-up Kit (Macherey-Nagel, 740609.250). 1 volume of sample and 2 volumes of NTI buffer were mixed and loaded onto a column. The sample was centrifuged for 30 seconds at 11000 x *g* and 22°C. Afterwards, the silica membrane was washed twice, each wash with 700 μL of NT3 buffer and centrifugation for 30 seconds at 11000 x *g* and 22°C. The membrane was dried by centrifugation for 1 minute at 11000 x *g* and 22°C and incubation for 2 minutes at 70°C. To elute the DNA, 15 μL of pre-heated (70°C) NE buffer was added to the column center and incubated for 1 minute at 22°C before centrifuging for 1 minute at 11000 x *g*. The elution was performed another time with fresh buffer.

Preparation of electro-competent *Xoo* cells To generate competent cells, the strain of choice was streaked on an NB plate and grown to single colonies at 28°C. A single colony inoculated in NB liquid media and grown overnight at 28°C and 200 rpm was used as pre-culture. The pre-culture was used to inoculate 200 mL of NB as a main culture with a strating cell concentration adjusted to OD_{600} of 0.005. The culture was growing for min 15 hours to OD_{600} of 0.8 and 1.0. The culture was split into 4 x 50 mL pre-chilled centrifugation tubes and placed on ice for 30 minutes. Cells were centrifuged for 10 minutes at 4000 x *g* and 4°C. The supernatant was decanted and the pellet carefully resuspended in 20 mL of pre-chilled autoclaved water. The cultures were placed on ice for 15 minutes before another centrifugation for 10 minutes at 4000 x *g* and 4°C. The supernatant was decanted and the pellet resuspended carefully in 20 mL of pre-chilled autoclaved 15% (w/v) glycerol. The cultures were placed on ice for 15 minutes before centrifuging for 10 minutes at 4000 x *g* and 4°C. The supernatant was decanted and the pellet carefully resuspended in 2 mL pre-chilled autoclaved 15% (v/v) glycerol. Roughly 120 aliquots of 75 μL of cells per tube were prepared and flash frozen in liquid nitrogen before storing at -80°C.

Transformation of electro-competent *Xoo* via electroporation An aliquot of competent cells was placed on ice for 10 minutes. 500 ng of plasmid DNA with maximal 5 μL and eluted in water was added to the cells. Cells and plasmid were transferred in a 0.1 cm electroporation cuvette (Biorad, 1652089). Electroporation was performed for 5 seconds at 2.5 kV and 200Ω. Immediately, 1 mL of pre-warmed (28°C) Recovery Medium for Expression (Sigma, CMR0001) was carefully added to the cells by pipetting against the cuvette wall. The cells were transferred into a 2 mL tube and grown for 3 hours at 200 rpm and 28°C. After 3 hours of incubation, the cells were concentrated by centrifugation for 30 seconds at 6000 x *g* and 22°C. The supernatant was decanted and the cells resuspended in the remaining media. 50 to 100 μL of cells were spread on an NB plate with appropriate antibiotic and grown for 3 to 7 days at 28°C.

Homologous recombination Deletion mutants in *Xoo* were generated by homologous recombination. 200 bp-long fragments up-and downstream of the gene of interest were amplified, flanked with an overlap of roughly 100 bp on the gene of interest. After amplification of the fragments as well as a spectinomycin (hereafter, spec) cassette, the PCR products were purified.
Restriction sites were added through 15 bp primer overhangs. EcoRI (5' end) and SpeI (3' end) cut sites were added to the upstream fragment. The cut sites of SpeI

Table 3.3: Ligation reaction

Reagent	Volume/Amount
T4 DNA ligase buffer (10x)	2 μL
Digested pK18sB	50 ng
Digested upstream fragment	10 ng
Digested downstream fragment	10 ng
Digested spec casette	50 ng
T4 DNA ligase	1 μL
Water	to 20 μL
Total	20 μL

were added to both ends of the spec fragment. And SpeI (5' end) and HindIII (3' end) cut sites to the downstream fragment. 1 μg purified pK18sB plasmid (Addgene, 177838) was linearized in a 100 μL reaction volume with EcoRI and HindIII at 37°C for 4 hours. The up-and downstream fragments as well as the spec-fragment were digested with the respective enzymes. Ligation of all three fragments with the pK18sB backbone was performed overnight at 16°C following the protocol in Table 3.3. 5 μL of the ligation product was used for transformation of TOP10 cells. Kanamycin-resistant colonies were tested by colony PCR and subsequent sequencing. Positive transformants were grown in liquid culture for plasmid isolation. The isolated plasmid was used to transform competent PXO99^{A} cells. The cells were grown for 5 days on NB plates. 20 colonies were transferred individually on both sides of a split plate with NB-spec and NB-spec supplemented with 10% (w/v) sucrose and grown at 28°C. On the next day, biofilm-rich colonies were used to inoculate 3 mL of NB-spec media, which were grown for 16 hours at 180 rpm and 28°C. The cultures were centrifuged for 1 minute at 11000 x *g* at 22°C and the supernatant was decanted. The pellet was resuspended in 3 mL NB media and centrifuged again. The washed pellet was resuspended in 3 mL NB supplemented with 1% (w/v) sucrose. The culture was grown for 6 hours at 180 rpm and 28°C. 100 μL of a 1:10 dilution was spread on NB-spec plates and incubated for 2 to 3 days at 28°C. Again, up to 20 colonies were transferred on both sides of a split plate with NB-spec with 10% (w/v) sucrose and NB-Kan and grown overnight at 28°C. Biofilm-rich colonies were used to inoculate 5 mL of NB-spec with 10% (w/v) sucrose and grown for 16 hours at 180 rpm and 28°C. Mutant lines were confirmed by extraction of gDNA for PCR and sequencing analysis. Cells were stored in 15% glycerol at -80°C.

Protein biochemistry

Recombinant protein production SuxB was amplified without signal peptide from *Xoo* gDNA and cloned with an N-terminal 6xHis-tag into the expression vector pRSETb. After verifying the insertion via sequencing, competent NiCo21(DE3) *E. coli* (NEB, C2529H) cells were transformed with the newly generated plasmid. Successful transformation was confirmed via colony PCR and sequencing. 5 mL LB medium was inoculated with a single colony and grown for 18 hours at 180 rpm and 37°C. The pre-culture was used to inoculate 200 mL of the main culture to a starting OD_{600} of 0.05. Since the cells inherited lacUV5, auto induction media (LB, 0.05% v/v D-glucose, 0.2% (v/v) lactose, 100 μg/mL carbenicillin) was used to induce the expression of the T7 polymerase subsequently leading to the activation of the T7 promoter of pRSETb and SuxB protein expression [115]. The main culture was grown for 48 hours at 180 rpm and 20°C before collecting the cells in four 50 mL tubes by centrifugation for 10 minutes at 5000 x *g* and 4°C. The pellets were stored at -20°C.

Protein purification via affinity chromatography Each pellet was resuspended in lysis buffer (Table 3.4) and incubated on ice for 15 minutes. The lysate was transferred into a 2mL tube and placed in a pre-cooled rack to sonicate on ice for 2 minutes with 30 cycles of a 4 seconds pulse at 50 Pa and 8 seconds rest. After sonication, the sample was centrifuged for 30 minutes at 20000 x *g* and 4°C. In the meantime, the Ni-NTA chromatography column (Biorad, #7311550) was loaded with 1.5 mL Ni-NTA (Macherey-Nagel, #745400.100). After settling, the column was equilibrated with 10 mL of 20 mM MOPS/KOH pH 7.0 buffer mixed with proteinase inhibitor. The sample supernatant was pipetted onto the column and incubated for 30 minutes at 4°C. The column was washed first with 10 mL 20 mM MOPS/KOH pH 7.0 followed by 10 mL 20 mM MOPS, 20 mM imidazole, pH 7.0. To elute SuxB from the column, 1 mL 20 mM MOPS, 250 mM imidazole, pH 7.0 was added and incubated for 30 minutes at 4°C. Afterwards, the elution was collected and a buffer exchange to 20 mM MES/KOH pH 6.5 using desalting columns (Zeba, #89892) was performed. The pH of 6.5 was chosen based on the isoelectric point (pI) of SuxB, which is predicted at a pH of 5.45. All buffers used were treated with protease inhibitor (Merck, 11836170001; 1 pill per 50 mL volume).
Successful purification of SuxB was confirmed via SDS gel electrophoresis. 4x Laemmli buffer was added to the sample and denatured for 5 minutes at 95°C. Gel electrophoresis was performed on a 4–20% polyacrylamide gel (Biorad, #4561094) for 90 minutes at 100 V in Tris-Glycine-SDS buffer (2.5 mM Tris, 19.2 mM Glycine,

Table 3.4: Lysis buffer for protein extraction of one cell pellet

Component	Volume	Concentration
MOPS/KOH, pH 7	1.6 mL	20 mM
DNase I	4 μL	50 U/μL
Lysozyme	10 μL	100 mg/mL

0.01% SDS, pH 8.3) with PageRuler (Thermo Scientific, #PI26616) as standard. To confirm the successful purification of SuxB (expected 69.7 kDa) the gel was stained with Coomassie (Serva, #35081.01) for 15 minutes and rinsed in water for 18 hours. When the correct mass was confirmed, the protein concentration was measured using a Bradford assay (Thermo Scientific, 23200). Purified SuxB and 20 mM MES/KOH pH 6.5 as control were diluted 1:10 and 1:20 in triplicates with Bradford reagent. After 10 minutes of incubation at 22°C, the reaction mix was transferred into a cuvette and the absorbance was measured at 595 nm. The protein concentration was calculated with the help of a BSA standard curve. Activity of SuxB was tested by the addition of 30 mM sucrose to 1 μg of protein. After a 30 minute incubation at 22°C, the presence of glucose was tested using a glucose test strip (Macherey-Nagel, #93024).

Enzyme kinetics To quantify the amount of glucose produced by SuxB, a DNS (3,5-dinitrosalicylic acid) assay was performed. 1 μg SuxB protein was added to 50 μL of varying sucrose concentrations (60 mM to 0.025 mM in 20 mM MES/KOH pH 6.5) in a 96-well plate. 20 mM MES/KOH pH 6.5 buffer served as negative control and 12 different glucose concentrations (60 mM to 0.025 mM in 20 mM MES/KOH pH 6.5) were used as references. The samples were incubated for 10 minutes at 28°C and enzyme activity was stopped by heat-inactivation for 5 minutes at 95°C. 60 μL of all samples, controls and standards were transferred to a new plate with 60 μL of DNS reagent (43.8 mM 3,5-dinitrosalicylic acid, 1.43 M $KNaC_4H_4O_6$ x 4 H_2O, 0.4 M NaOH) and boiled for 10 minutes at 95°C. After cooling to 22°C, 100 μL of each reaction were transferred to a flat, black 96-well plate and absorbance was measured at 540 nm. The background was subtracted, and the amount of glucose produced by SuxB calculated on the basis of the glucose reference curve.
pH- and temperature-dependent activity of SuxB was tested as described above with the difference that either 6 mM sucrose was diluted in a pH series of 20 mM MES/KOH pH 4.5 to 11.5 or the incubation temperature was set to 20, 25, 30, 31.6, 34.6, 39.5, 45.3 and 49.6°C.
To calculate the amount of glucose produced by SuxB and to determine the Michaelis-Menten constant (K_M), we performed background subtraction and generated a

standard curve using linear regression ($Y = a + bx$) from the glucose reference values. The sample absorbance readings were corrected by subtracting the intercept (a) and dividing the results by the slope (b) of the linear regression. The calculated values were normalized to reflect activity over 1 minute. The substrate concentrations (X-axis) were plotted against the calculated enzyme velocities (Y-axis) and fitted by the non-linear regression of the Michaelis-Menten equation ($v = \frac{V_{\max}[S]}{K_M+[S]}$). From the fitted curve, V_{max} was determined and $\frac{1}{2}V_{max}$ used to calculate K_M of SuxB.
Extracellular SuxB activity was tested in the culture supernatant of *Xoo*. Cells were grown in 5 mL NB media supplemented with 30 mM sucrose to activate transcription of the *sux* gene cluster. At OD_{600} 0.8, the cells were pelleted at 6000 x *g* for 2 minutes and the protein-containing supernatant was transferred into a new tube. The supernatant was used as input for the above-described assay with an incubation time of 60 minutes.

Computational analysis

Phylogenetic analysis of SuxB A phylogenetic tree of SuxB was prepared based on Lemoine et al., 2019 [89]. In brief, sequences of SuxB, including the putative signal peptide, from 17 *Xanthomonas* species (*Xanthomonas arboricola pv. juglandis* CP076725; *Xanthomonas axonopodis pv. cimmiphoreae* GCF 003698225.1; *Xanthomonas campestris pv. campestris* GCF 000007145.1; *Xanthomonas euvesicatoria pv. alfalfae* GCF 000488955.1; *Xanthomonas citri pv. citri* GCF 000961215.1; *Xanthomonas cucurbitae* GCF 009883735.1; *Xanthomonas euvesicatoria* CP018467.1; *Xanthomonas fragariae* GCF 900183975.15; *Xanthomonas oryzae pv. oryzicola* GCF 000168315.3; *Xanthomonas oryzae pv. oryzae PXO99^A* GCF 000019585.2; *Xanthomonas perforans* GCF 028010245.1; *Xanthomonas prunicola* CP096140.1; *Xanthomonas vasicola pv. vasculorum* GCF 003015715.1; *Xanthomonas translucens pv. translucens* GCF 009600865.1; *Xanthomonas translucens pv. undulosa* GCF 023221635.1; *Xanthomonas oryzae* pv. *oryzae MAI1* GCF 003031365.1; *Xanthomonas oryzae* pv. *oryzae BAI3* GCF 003031385.1) were aligned through MAFFT. Poorly aligned sections were trimmed using BMGE. A phylogenetic tree was constructed via maximum likelihood using PhyML, employing the GTR substitution model. The tree, rendered in the Newick format, was visualized with 100000 bootstraps using the online tool available at www.ngphylogeny.fr.

***In silico* prediction of SuxB localization and presence of signal peptide** The localization of SuxB was assessed using PSORTb v3.0 [116]. No difference in

localization was detected by the putative signal peptide. Signal peptide sequences of SuxB as well as putative cleavage sites were predicted using SignalP 5.0 for gram-negative organisms [117].

3.3 Results and discussion

Identification of a SuxB secretion sequence

The *sux* cluster in *Xoo* is involved in sucrose uptake and encodes four genes: *suxR*, *suxC*, *suxA* and *suxB* (Chapter 2). While *suxR* and *suxC* are each transcribed with individual promoters, *suxA* and *suxB* form a bicistronic operon (Figure 3.1). Sequence analysis identified an alternative open reading frame (ORF) for *suxB* that extends *suxB* by a 34-amino-acid N-terminal peptide. The alternative ORF overlaps with the C-terminal coding region of *suxA*, but in a different reading frame (Figure 3.1).

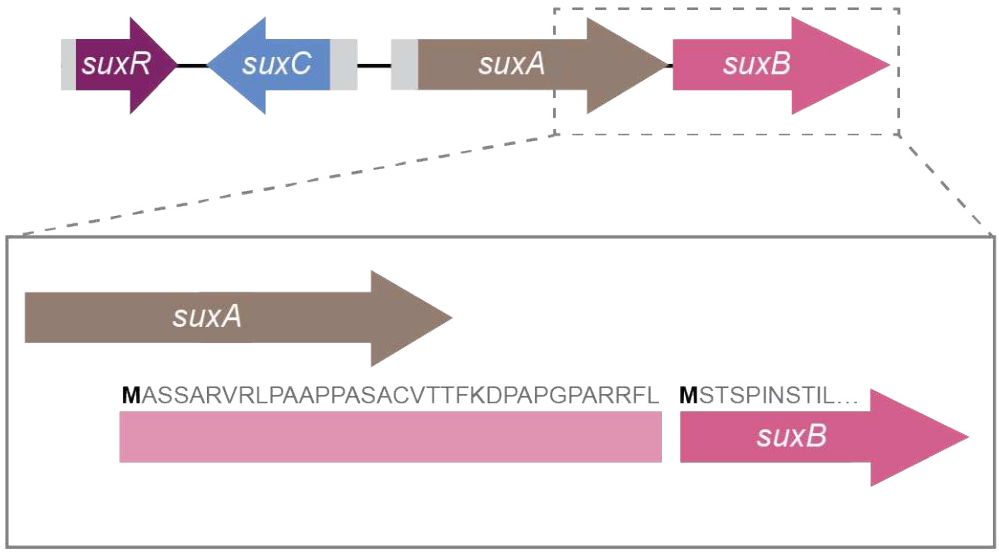

Figure 3.1: Identification of an alternative ORF for *suxB*. The *sux* cluster encodes four genes: *suxR* (purple), *suxC* (blue), *suxA* (brown) and *suxB* (pink). The zoom-in illustrates a 34-amino-acid N-terminal extension of *suxB* (light pink) that overlaps with the coding region of *suxA*, but on a different reading frame.

To assess whether the peptide affects SuxB localization, subcellular localization of SuxB with and without peptide extension was predicted using PSORTb v3.0 [116]. Both SuxB reading frames were predicted to localize to the cytoplasmic membrane (44.4%) and in the extracellular space (44.2%) (Figure 3.2A). Lower probabilities were assigned to periplasm localization (10.9%), with less than 1% each to outer-membrane and cytoplasm. Based on the prediction, a dual localization of SuxB in the intracellular ($SuxB_{in}$)- and extracellular ($SuxB_{ex}$) space was considered. To evaluate whether the alternative ORF and its resulting peptide could function as a signal peptide for secretion, we analyzed the amino acid sequence using SignalP5.0 [117]. SignalP5.0 predicted a 45.25% probability that the peptide mediates

secretion and is cleaved after 16 amino acids at an "ASA-CV" motif by signal peptidase II (Figure 3.2B). Motif analysis classified the peptide as a lipoprotein signal. The detected “ASA-C” motif shares key characteristics with the canonical “LSAC” lipobox, including the conserved cysteine residue essential for cleavage during secretion [118]. SignalP5.0 further predicted SuxB translocation via the Sec-translocon.

In summary, the analysis revealed an alternative ORF of *suxB* that putatively encodes a signal peptide for secretion via the Sec-translocon. Based on the results we hypothesize that SuxB is dual-localized and could potentially be secreted via the Sec pathway in combination with the type II secretion system (T2SS) [24].
Secreted metabolic enzymes are common for pathogens and can contribute not only to nutrient acquisition but also to pathogen-host interaction. A well-studied example is the secreted alpha-amylase AmyA of *Xanthomonas campestris pv. campestris* (*Xcc*), which is required for extracellular starch degradation [119]. In *Xoo*, secretion of metabolic enzymes primarily occurs through the T2SS. The general secretory pathway mediates the secretion of cell wall–degrading enzymes (CWDEs), including lipase LipA, endoglucanase ClsA, and xylanase XynB, which are crucial for the virulence of *Xoo* [51, 107, 120]. Unlike the canonical T2SS substrates, typically dedicated to extracellular function and localized exclusively outside of the cell, SuxB may represent an exception.
The proposed dual localization of SuxB raises the possibility of distinct functional roles in different cellular compartments. Although protein secretion is common among metabolic enzymes, dual localization of a single protein is a rare phenomenon. The most prominent example is the *suc2* gene in *Saccharomyces cerevisiae* (hereafter yeast), where two alternative mRNA isoforms determine subcellular targeting to the intra- or extracellular space [121, 122]. The two Suc2 isoforms are differentially localized and functionally specialized: extracellular Suc2 supports cooperative nutrient acquisition by acting as a shared resource, while intracellular Suc2 enables the cell to retain metabolic products for individual use under nutrient-limited conditions. This functional separation of Suc2 in yeast is discussed in the context of public and private goods, a concept derived from economic game theory [111, 112].

Conservation of SuxB signal peptides

To investigate the conservation of the newly identified signal peptide, we analyzed the potential signal peptide of 15 *Xanthomonas* species. From each *Xanthomonas* genome, we extracted a 34-amino acid sequence upstream of the annotated start

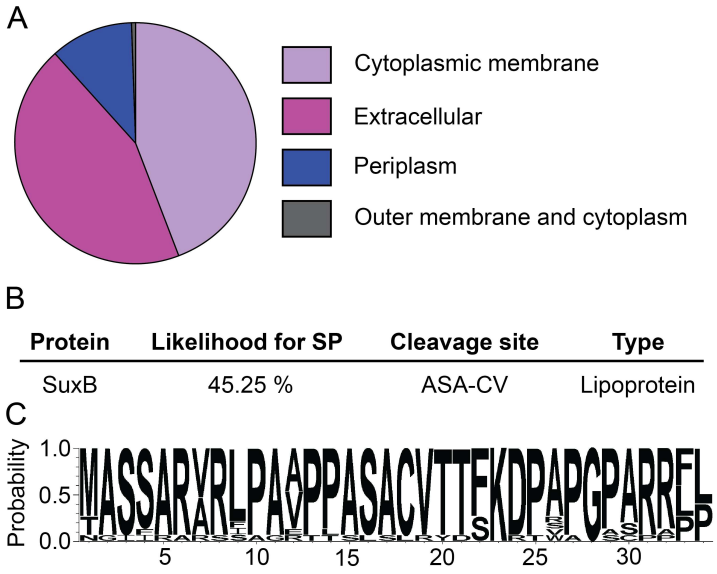

Figure 3.2: Computational characterization of SuxB A Localization likelihood prediction of SuxB depicted in a pie chart for cytoplasmic membrane (lavender), extracellular (pink), periplasm (blue) as well as outer membrane and cytoplasm (grey) localization. Protein sequence analysis using PSORTb v3.0. **B** Identification of putative signal peptide for secretion. SignalP5.0 software characterized likelihood, peptide type and cleavage site for the identified upstream region of SuxB. **C** Sequence logo analysis of SuxB signal peptide for secretion. Protein sequence of 17 *Xanthomonas* species with given probability for individual amino acid conservation.

codon. Sequence logo analysis by WebLogo3 [123] revealed a high degree of conservation within the signal peptides (Figure 3.2C). Across the analyzed species, two-thirds of the amino acid positions exhibited conservation >93%, and nearly three-quarters exceeded conservation of 80%. In contrast, in the extracted sequence of *Xcc*, conservation greater than 25% was observed at only four amino acids.
To assess functionality of the sequences as signal peptides in the analyzed *Xanthomonas* species, we searched the sequences for in-frame stop codons as well as start codons. The results indicated that SuxB from *Xcc* and *X. perforans* likely lack a functional signal peptide due to the presence of in-frame stop codons (Supplementary Table 3.5). The remaining species did not encode stop codons in the peptide sequence. Further, we analyzed the first amino acid positions for potential start codons. Compared to the remaining sequence logo, the start position showed less conservation. Roughly 74% of the analyzed species encode a methionine (M), indicating functionality of a signal peptide for secretion. In contrast, 20% encode a threonine (T), and *Xcc* encodes an asparagine (N) in the analyzed position. Comparison of the sequences at DNA level showed that methionine (ATG) and threonine (ACG) codons differ by a single base. Phylogenetic analysis of the peptide sequence mirrored the patterns observed in the sequence logo. The resulting phylogenetic tree clustered the

15 *Xanthomonas* species into two clades according to start codon identity: one clade with start codon (M), the other clade without (T or N) (Supplementary Figure 3.7). All start codon-encoding peptides were individually analyzed with SignalP5.0. The results predicted a signal peptide with lipoprotein characteristics, consistent with the results for *Xoo* (Supplementary Table 3.6).

Reduced SuxB activity under acidic and low-temperature conditions

Secreted proteins are exposed to changing environmental conditions according to their localization. To assess whether the sucrose hydrolase activity of SuxB [41] varies under conditions that mimic the intra- and extracellular environments of *Xoo* during rice infections, we measured enzymatic activity of purified SuxB across physiological pH and temperature ranges. The conditions represent the *Xoo* cytosol and the plant xylem, respectively. SuxB was treated with sucrose under the given environments, and the resulting reduced sugars, used as a proxy for SuxB activity, were quantified using a colorimetric DNS (dinitrosalicylic acid) assay. SuxB activity at reaction temperatures from 20°C to 49.6°C followed a temperature-dependent, Gaussian-shaped distribution. Minimal activity was detected below 25°C and above 49.6°C, while maximal activity was measured between 31.6°C and 39.5°C (Figure 3.3A). The SuxB activity pattern overlaps with the environmental conditions commonly encountered by *Xoo* in nature as well as with greenhouse conditions.

Activity profiling of SuxB across a pH range of 4.5 to 11.5 revealed a pH-dependent, Gaussian-shaped distribution. Highest enzymatic activity was observed between pH 7.5 and 9.5, with moderate activity at pH 5.5 and little to no activity at pH 4.5 or above pH 10.5 (Figure 3.3B). The results are consistent with previously reported physiological pH values in *Xcc*, where the cytosol ranges from pH 7 to 8, depending on culture conditions [124]. If a similar cytosolic pH is assumed for *Xoo*, the observed activity range would support SuxB function proposed at the cytoplasmic membrane. The pH of the plant extracellular space can vary during the infection. While phloem sap typically has an alkaline pH around 8.0 [125], xylem sap is more acidic, ranging from pH 5.6 to 6.0, likely due to the presence of transported amino acids [126]. In wounded rice leaves, we measured a sap pH of 4.5 (unpublished), indicating that *Xoo* must maintain enzymatic activity across a broad pH spectrum. Our results, however, showed that SuxB activity decreased under acidic conditions. This reduction may reflect a limitation of the SuxB variant used in this study, which

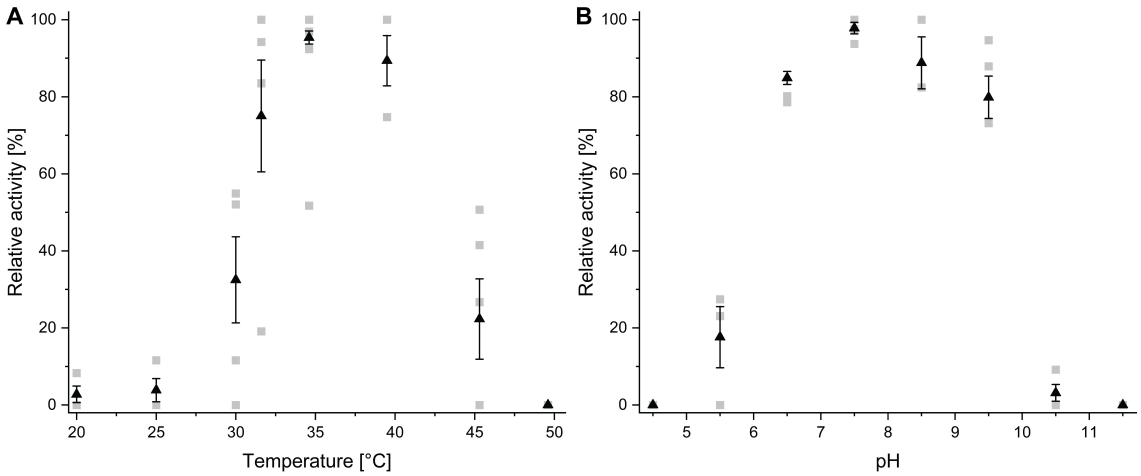

Figure 3.3: Sucrose hydrolase activity of SuxB in physiological pH and temperature conditions. Relative sucrose hydrolase activity of SuxB **A** at varying pH from 4.5 to 11.5 (n=4) and **B** at varying temperature from 20°C to 49.6°C (n=3). SuxB was purified via Ni-NTA affinity chromatography. Enzymatic activity was measured using a colorimetric invertase assay and normalized independently per biological replicate using min–max scaling. Each biological replicate (grey boxes) comprised 12 technical replicates. Black triangles indicate the mean value with error bars ± SEM.

lacks the native signal peptide. Alternatively, the reduced activity at low pH may reflect limitations of the *in vitro* conditions used to test activity. Under physiological conditions, extracellular pH is buffered by a local microenvironment. Sucrose-induced activation of the *sux* operon promotes extracellular polysaccharide (EPS) production and biofilm formation [41]. EPS has been shown to function as a protective barrier, buffering extracellular pH changes [24, 53, 127]. Within the EPS/biofilm matrix, a pH gradient has been proposed to emerge, protecting *Xoo* cells and their secreted enzymes [53]. To retain extracellular SuxB activity, *Xoo* may rely on such protective micro-environments formed by EPS and biofilm.

Extracellular SuxB activity

To test whether SuxB is secreted into the extracellular space and active, *in vitro* sucrose hydrolase activity was measured in the supernatant of *Xoo* cultures. Wildtype cells and *sux* cluster deletion strains were grown in sucrose-supplemented media, serving as a proxy for the extracellular space [41]. Reduced sugars in the supernatant were quantified using a colorimetric DNS assay. In the supernatant of wildtype *Xoo* and Δ*suxR* cells, little to no reduced sugars were detected (Figure 3.4), indicating that SuxB is not secreted into the medium under these conditions. In contrast, reduced sugars accumulated in the supernatant of Δ*suxC* and Δ*suxA* cultures, which

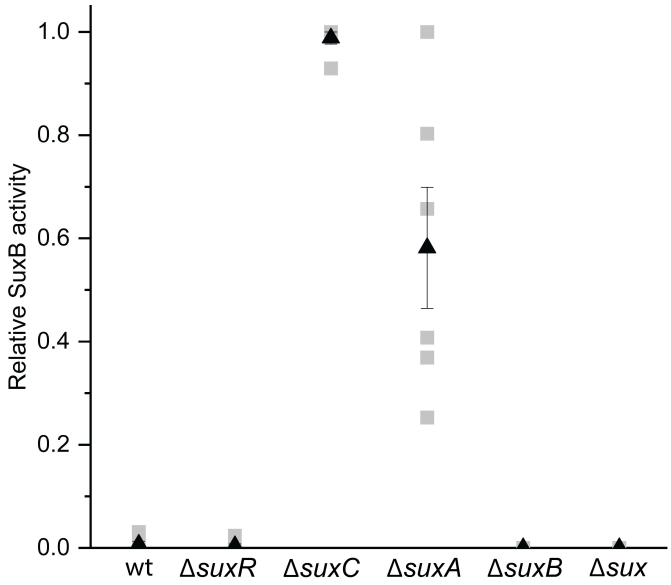

Figure 3.4: Extracellular SuxB activity Relative sucrose hydrolase activity of SuxB measured in the extracellular space of *Xoo* cultures from wildytpe, Δ*suxR* (LacI-type repressor), Δ*suxC* (inner membrane MFS H^+-symporter), Δ*suxA* (outer membrane TonB-like porin), Δ*suxB* (sucrose hydrolase), and Δ*sux*. Enzymatic activity was measured using a colorimetric invertase assay and normalized independently per biological replicate using min–max scaling. Each biological replicate comprised three technical replicates (grey boxes). Black triangles indicate the mean value with error bars ± SEM.

lack crucial sucrose transporters and are not able to grow beyond base growth [41]. Crucial to mention here is that the Δ*suxA* strain still expresses the predicted signal peptide. The result supported the computational predictions that SuxB is indeed secreted (Figure 3.4). SuxB activity was absent in Δ*suxB* and Δ*sux* deletion strains, confirming that SuxB was responsible for the observed sucrose hydrolysis. In Chapter 2 [41] and [39], the literature showed that cytosolic SuxB activity is required for sucrose utilization. Here, we detected SuxB activity in the culture supernatant when sucrose cannot be imported by *Xoo*. Based on our results, we hypothesize that the secretion of SuxB occurs under conditions of sucrose limitation.

Regulatory mechanisms of SuxB localization

The presented results provide evidence that *Xoo* can switch between a secreted ($SuxB_{ex}$) and non-secreted ($SuxB_{in}$) form of SuxB, likely depending on the nutritional status of the cell. To explore potential regulatory mechanisms allowing a dual localization, the *sux* operon was analyzed for sequences or structural elements that allow the cell to distinguish between the two forms of SuxB. The alternative ORF for $SuxB_{ex}$ overlaps with the coding region of *suxA*. In contrast, *suxA* and $SuxB_{in}$

are separated by an intergenic region encoding 11 amino acids. *In silico* analysis of this intergenic region revealed dyad symmetries of putative hairpin structures [113]. Additionally, an RNA sequence between the ORFs of *suxR* and *suxC* was identified with potential for regulation as a small regulatory RNA (sRNA) or as a peptide (Figure 3.5 and Supplementary Figure 3.6).

Rho-independent transcription termination To generate distinct *suxB* transcripts from the *suxAB* operon, differential termination of *suxA* transcription could play a regulatory role. In bacteria, transcription can be terminated via a Rho-independent mechanism. For a Rho-independent termination, secondary RNA structures, such as the described hairpins, can act as intrinsic terminators. Hypothesizing a Rho-independent transcription termination of *suxA*, two independent *suxB* transcripts could be transcribed and enable *Xoo* to distinguish between $SuxB_{ex}$ and $SuxB_{in}$. As a prerequisite for the hypothesis, it requires that the *suxAB* operon is transcribed as two separate units: *suxA* and *suxB*. To determine whether *suxAB* is transcribed as a single polycistronic mRNA or as discrete transcripts, we examined the existing *in vitro* RNAseq data from Chapter 2 [41]. Transcriptomic analysis revealed transcription across *suxA* and *suxB* leading to one polycistronic mRNA. The findings indicate that the identified hairpin structures are unlikely to function as Rho-independent terminators. The hypothesis that the termination of *suxA* transcription can contribute to the regulation of dual localization of SuxB was therefore rejected.

Attenuation-like regulation by small RNA An alternative hypothesis to Rho-independent transcription termination is that secondary RNA structures, such as the identified hairpins, mediate an attenuation-like mechanism that controls the regulation of $SuxB_{ex}$ and $SuxB_{in}$. The key principle of attenuation lies in the use of structural elements which can form competing hairpins [114]. One structure promotes ribosome stalling and transcriptional read-through, while the other hairpin causes transcription termination. In the *suxAB* operon, we identified two hairpin structures, which can be divided in three domains (Figure 3.5A). The first hairpin is formed by domains 1 and 2 and the second hairpin by domains 2 and 3 (Figure 3.5B, C). The formation of two hairpins by differential usage of the same domains, indicates a similar mechanism of structural competition as in classical attenuation. The hairpins differ in G-C bonds, and we therefore hypothesize that a hairpin formed by domain 1 and 2 is more likely to be overcome by RNA polymerase and ribosomes as the

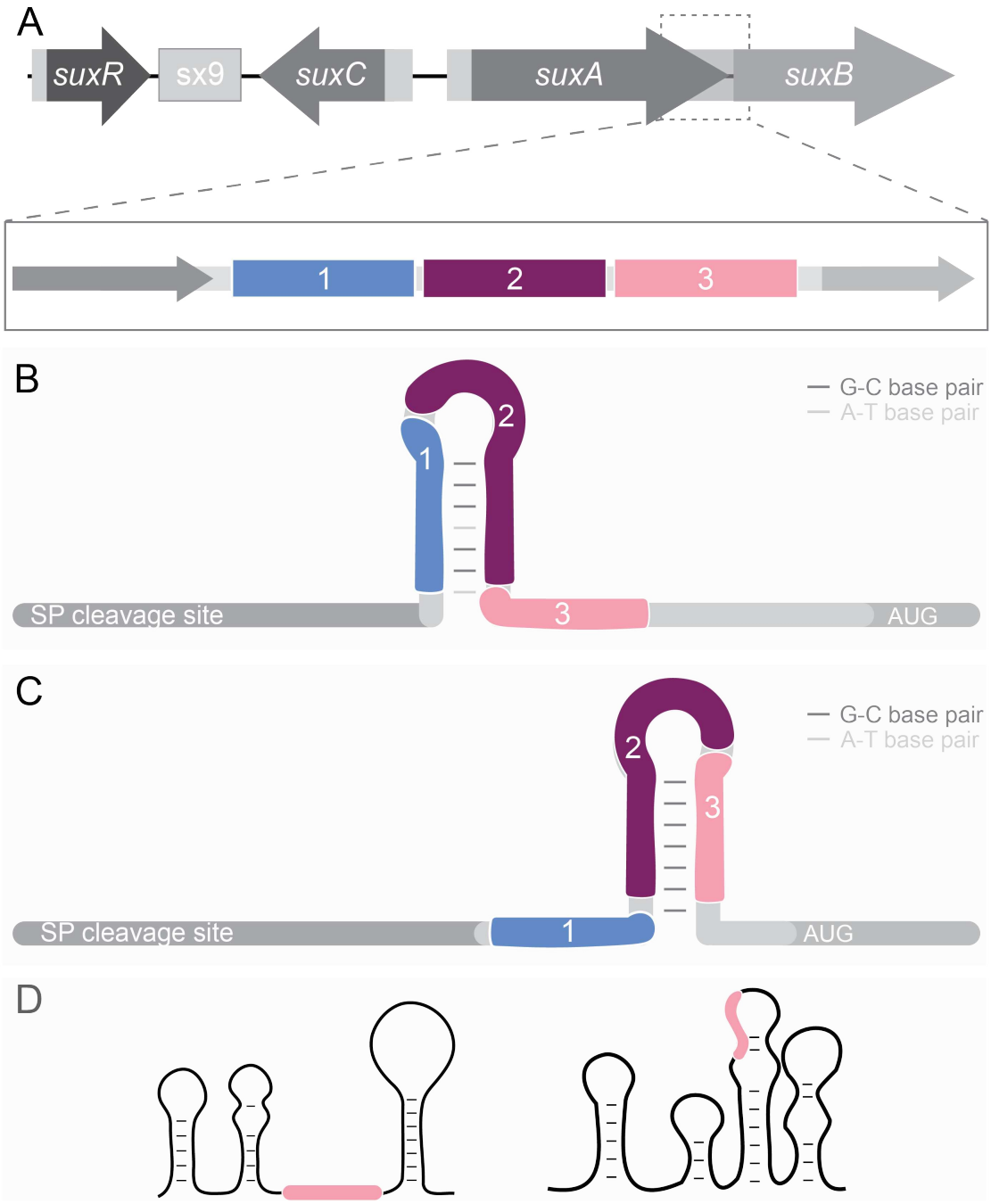

Figure 3.5: Potential attenuation-like regulation of the *sux* operon by sRNA sx9. A Schematic overview of the *sux* operon, including the newly identified sRNA sx9. A close-up of the intergenic region between *suxA* and $SuxB_{in}$ highlights three domains capable of forming two distinct hairpins. **B** The first hairpin forms through base pairing between domain 1 (blue) and 2 (purple), comprising five G-C and two A-U base pairs. **C** The second hairpin forms between domain 2 (purple) and 3 (pink), with seven G-C base pairs. **D** Predicted secondary structures of sx9 based on Rfam model RF02228. The pink region indicates sequence homology with domain 3, present in both hairpins.

hairpin made out of domain 2 and 3, which possesses 7 instead of 5 G-C bonds. Attenuation of the *trp* operon involves transcription-translation coupling and is regulated by the availability of $tRNA^{trp}$, which determines whether a transcriptional terminator forms in the leader peptide [114]. The *sux* operon is not involved in amino acid biosynthesis but contributes to sucrose uptake. Thus, we hypothesized that sugar availability may influence the transcription and translation of the *sux* operon through a similar mechanism. Sugar binding of structural elements might affect the formation of hairpins within the *sux* transcript. Sugar-mediated transcriptional regulation is found in the *bgl* operon of *E. coli*, which encodes genes for β-glucoside sugar metabolism. In the presence of β-glucosides, BglG binds the RNA and acts as anti-terminator by preventing the formation of a terminator hairpin, enabling transcription of the *bgl* operon [128, 129]. We observed that the identified sRNA in the *sux* cluster, Sx9, contains sequence homology to domain 3 of the predicted hairpins (Figure 3.5D). We hypothesize that Sx9 might bind to the RNA of domain 3 and destabilize secondary structures, thereby facilitating transcriptional read-through and translation of $SuxB_{ex}$. This hypothetical function resembles the role of BglG, although mediated by an sRNA molecule rather than a protein.
To distinguish between classical attenuation, anti-termination and riboswitch-like regulation, and to evaluate our hypothesis, ribosome profiling could be used to determine ribosome positions during translation of the *sux* operon. Ribosome profiling provides high positional resolution on ribosome occupancy, which can help to find out whether transcription and translation are coupled - a hallmark of attenuation - or whether regulatory elements act independently of ribosomes, as seen in riboswitches. One possible scenario is that hairpin 1 enhances translation of $SuxB_{ex}$ by causing the ribosome to pause over the secretion peptide sequence [130, 131]. Formation of hairpin 2 may enable ribosome re-binding and promote the translation of $SuxB_{in}$ (Figure 3.5).

3.4 Conclusions and outlook

Bacterial blight is a rice disease caused by the bacterium *Xoo*. To acquire nutrients from its host, the pathogen secretes transcription activator like effectors (TALes) into the host, which induce the transcription of rice *SWEET sucrose uniporter* genes. TAL secretion eventually leads to sucrose export into the xylem parenchyma, where it becomes accessible to the bacterium. Host-derived sucrose is imported by *Xoo* via the *sux* cluster, which comprises four core genes: *suxR*, *suxC*, *suxA* and *suxB*. SuxB was previously classified as cytosolic sucrose hydrolase [40]. Here, we detected

an alternative ORF for *suxB* that encodes a secreted form of the sucrose hydrolase. We identified the responsible signal peptide, which likely mediates secretion and is conserved across multiple *Xanthomonas* species. In light of the proposed dual role of SuxB during host colonization, it is essential to understand how *Xoo* regulates between $SuxB_{in}$ and $SuxB_{ex}$. We propose three non-exclusive mechanistic hypotheses regarding the biological significance:

(i) A parallel pathway increases uptake capacity.
To maximize the capacity for sucrose hydrolysis, *Xoo* could benefit by producing both intracellular and extracellular SuxB under conditions of high substrate availability. An opposing example is the α-amylase AmyA, which is exclusively secreted by *Xanthomonas campestris pv. campestris* and breaks down host starch in the extracellular space [119]. A dual localization of metabolic proteins in *Xoo* would allow flexibility and fast adaptation to changing environments. Dual localization of SuxB in *Xoo* could enhance the efficiency with which host-derived sucrose is processed once TALes are secreted, *SWEET* genes are activated and sucrose is released.

(ii) Two isoforms have been optimized for distinct biochemical niches.
The intra- and extracellular forms of SuxB may differ in terms of their kinetic properties, such as pH optima since after signal peptide cleavage 15 amino acids of the peptide remain on $SuxB_{ex}$. This could allow *Xoo* to effectively hydrolyze sucrose in both, the cytoplasm and the xylem parenchyma. Although the dual localization of metabolic enzymes is rare in bacteria, it is a known strategy in eukaryotes. Several mitochondrial and cytosolic isoforms of glycolytic enzymes allow fine-tuning of carbohydrate metabolism across compartments [132–134]. In such systems, compartment-specific physicochemical constraints, such as ion concentrations and redox potential drive the isoform specialization. In *Xoo*, the xylem sap may favor the secretion of an enzyme form that remains stable and active under the given conditions.

(iii) Secretion transforms SuxB into a public good.
Secreted SuxB could act as a cooperative trait, enabling neighboring non-secreting cells to benefit from extracellular sucrose hydrolysis. A well-documented example of such a dual system is the SUC2 invertase of *Saccharomyces cerevisiae* (hereafter called yeast). SUC2 produces two isoforms via differential transcriptional initiation and mRNA processing: a longer transcript encodes a secreted enzyme with an N-terminal signal peptide, and a shorter transcript produces a cytoplasmic version [121, 135].

SUC2 promotes cooperative growth in structured environments by releasing glucose and fructose as public goods that can diffuse to cells of their kin. In microbial ecology, such cooperative enzyme secretion is favored when the local density of kin is high, as known in biofilms, since it reduces the risk of exploitation by unrelated 'cheater' cells [136]. In *Xoo*, extracellular polysaccharides (EPS) support biofilm formation and may buffer local pH allowing hydrolysis and limit diffusion of products. This could promote the retention of hydrolysis products and stabilizes enzyme activity [53, 127]. $SuxB_{ex}$ may provide a fitness advantage at the community level.

To test these hypotheses, a crucial next step is be generation of exclusively intra- or extracellular SuxB mutants. Further biochemical comparison of the two SuxB forms is required, including an assessment of their kinetic parameters, pH optima and thermostability under extracellular conditions resembling those of the host. The current results are based on activity measurements performed with $SuxB_{in}$, the cytoplasmic form of the enzyme lacking the N-terminal signal peptide required for secretion. Analysis of native SuxB protein using invertase activity gels could reveal differences in folding or stability conferred by the presence or absence of the signal peptide. Post-translational modifications such as glycosylation, although less well understood in bacteria, may play a role. Glycosylation of *Xoo* flagellin proteins has been shown to enhance stability and evade host immune recognition [137]. Additionally, we have identified 15 potential hexose uptake candidates, that could import the hydrolysis products. A combination of identifying the role of $SuxB_{ex}$ *in planta* and characterizing a potential hexose uptake pathway would allow a deeper understanding of the physiological function of SuxB secretion.

Supplementary

Table 3.5: Alignment of putative signal peptide sequences from different *Xanthomonas* species.

Species	Peptide sequence
X. vasciola pv. vasculorum	MASSARVRLPAAPPASA-CVTTFKDPAPGPARRLL
X. prunicola	MASSARVRLPAAPPASA-CVTTSKDPAPGPARRLP
X. perforans	MASSARAR*PAVPPASA-CVTTFKDPAPGPARRPL
X. oryzae pv. oryzicola	MASSARVRLPAAPPASA-CVTTFKDPAPGPARRFL
X. oryzae pv. oryzae MAI3	MASSARVRLPAAPPASA-CVTTFKDPAPGPARRFL
X. oryzae pv. oryzae PXO99^A	MASSARVRLPAAPPASA-CVTTFKDPAPGPARRFL
X. oryzae pv. oryzae BAI3	MASSARVRLPAAPPASA-CVTTFKDPAPGPARRFL
X. euvesicatoria pv. alfalfae	MASSARARLPAVPPASA-CVTTFKDPAPGPARRPL
X. euvesicatoria	MASSARARLPAVPPASA-CVTTFKDPAPGPARRPL
X. fragariae	TASSARVRFPAEPPASA-CVTTSKDPSPGPSRRFP
X. cucurbitae	TASSARARSPAVPPASA-CVTTSKDPVPGAARPLP
X. arboricola pv. juglandis	TASSARARLPAAPPASA-CVTTSKDPWPGSSRRLP
X. citri pv. citri	MASFARVRLPAVPPASA-CVTTFKDPAPGPARRLP
X. campestris pv. campestris	-NGIIRARSIAGRTTSLSLRYDF*RTRAGPCPAFP
X. axonopodis pv. commiphoreae	MASSARARLPAVPPASA-CVTTFKDPAPGPARRPL

Table 3.6: Predicted signal peptide likelihoods for SuxB$_{ex}$ across *Xanthomonas* species. Putative SuxB$_{ex}$ peptide sequences of 12 *Xanthomonas* species were analyzed for signal peptide properties using SignalP5.0. Predicted likelihoods for distinct secretion pathways are given (Sec/SPI = Transport of "standard" peptides via Sec translocon/cleaved by signal peptidase I (Lep); Tat/SPI= Transport of "tat" peptides via Tat translocon/-cleaved by signal peptidase I (Lep); Sec/SPII= Transport of lipoprotein peptides via Sec translocon/cleaved by signal peptidase II (Lsp); Other= No signal peptide) [117]. Higher values indicate higher likelihoods for secretion via the respective pathways.

Species	Sec/SPI	Tat/SPI	Sec/SPII	Other
X. vasciola pv. vasculorum	0.095	0.0623	0.4327	0.4099
X. prunicola	0.0949	0.0993	0.5228	0.2831
X. perforans	0.1255	0.1007	0.4028	0.3709
X. oryzae pv. oryzicola	0.093	0.0554	0.4525	0.3991
X. oryzae pv. oryzae MAI3	0.093	0.0554	0.4525	0.3991
X. oryzae pv. oryzae PXO99^A	0.093	0.0554	0.4525	0.3991
X. oryzae pv. oryzae BAI3	0.093	0.0554	0.4525	0.3991
X. euvesicatoria pv. alfalfae	0.0417	0.0279	0.8547	0.0757
X. euvesicatoria	0.0417	0.0279	0.8547	0.0757
X. citri pv. citri	0.0747	0.047	0.5901	0.2882
X. axonopodis pv. commiphoreae	0.0919	0.0775	0.5326	0.298

Figure 3.6: Secondary RNA structures of SuxB hairpins. The first underlined sequence shows the signal peptide cleavage site of $SuxB_{ex}$. Hairpin forming domains are colored with blue (domain 1), purple (domain 2) and pink (domain 3). The second underlined sequences indicated the start codon of $SuxB_{in}$. **A** The first hairpin forms through base pairing between domain 1 (blue) and 2 (purple), comprising five G-C and two A-U base pairs. **B** The second hairpin forms between domain 2 (purple) and 3 (pink), with seven G-C base pairs.

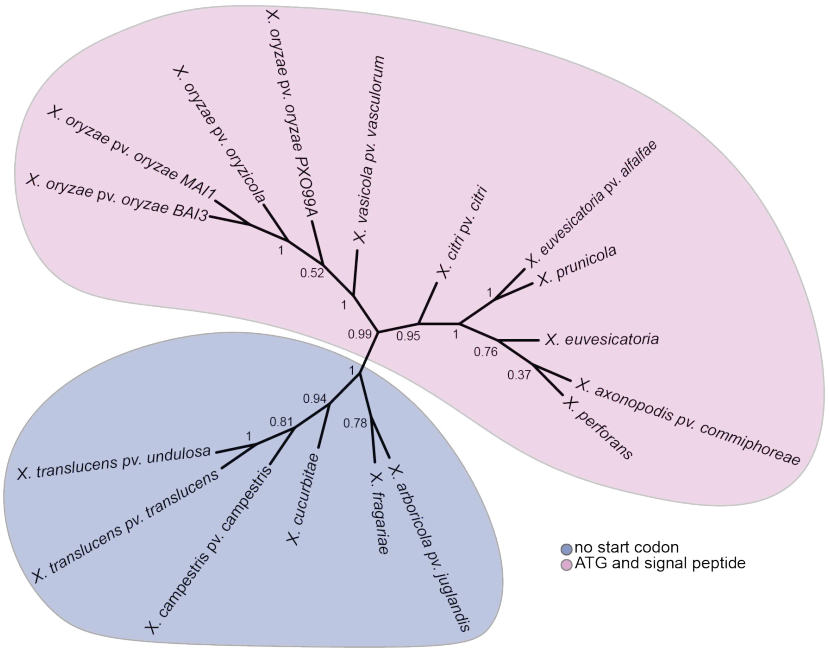

Figure 3.7: Phylogenetic analysis of predicted SuxB signal peptide sequences from 15 *Xanthomonas* species. The sequences clustered into two main clades according to start codon identity: one clade containing species with methionine (M) as start codon and the other clade comprising species without start codon.

CHAPTER 4

Infection against the xylem stream[3]

3: This chapter summarizes unpublished work.

I contributed approximately 95 % to this chapter. For Chapter 4.1, I collaborated with Prof. Dan V. Nicolau and Dr. Ayyappasamy Sudalaiyadum Perumal of McGill University, Montreal. The collaboration partners developed the model and provided the corresponding equations, which were published in [66]. I independently calculated the motility trajectories and wrote the chapter.
For Chapter 4.2, I collaborated with PD Dr. Dietrich Kohlheyer and Lennart Witting of the Forschungszentrum Jülich. The collaboration partners developed the microfluidic chip, which was published in [138]. Under the instructions of Lennart Witting, I conducted motility experiments in the microfluidic setup. I performed the data analysis and wrote the chapter.
For Chapter 4.3, I performed all experiments, data analysis, and wrote the chapter independently.

4.1 Hydrodynamic modeling of *Xoo* swimming motility

The xylem vasculature of rice presents a structurally complex environment for bacterial motility. Vessel elements are interrupted by pit membranes, which connect adjacent parenchyma cells. Effective host colonization by *Xanthomonas oryzae pv. oryzae* (*Xoo*) depends on the ability to localize to optimal physical spaces in the xylem environment [66]. However, it remains unclear where within the xylem vessels *Xoo* colonizes and swims during infection.

To predict the ideal biophysical localization within the xylem for *Xoo*, we applied a hydrodynamic motility model developed by Tokárová et al. 2021 [66], which predicts bacterial swimming trajectories based on cell geometries and flagellar dynamics. To apply the model to *Xoo*, we extracted values for cell shape and flagellum length from the literature: *Xoo* is a rod shaped bacterium (0.8–1.0 × 1.7 μm) with a monotrichous polar flagellum measuring 6–8 μm [5, 6]. Based on these values, the input parameters for the motility model were calculated (Table 4.1) and a simplified motility model was visualized with the predicted trajectory of *Xoo* (Figure 4.1). Published trajectories from Tokárová et al. 2021 were kept for reference [66].

Table 4.1: Input parameters of the motility model for *Xoo* cell body and flagellum dimensions. Parameters were calculated using data from [5, 6] and the equations of [66].

Parameter Description	Symbol	Value
Polar radius of the cell body	a_1	0.85 μm
Equatorial radius of the cell body	a_2	0.45 μm
Aspect ratio of the cell body	a_1/a_2	1.88
Curvilinear length of the flagellum	L	7 μm
Radius of sphere with volume of cell body	$\bar{a}$	0.5563 μm
Nondimensional length of the flagellum divided by $\bar{a}$	$L/\bar{a}$	12.58

The calculated parameters $L/\bar{a}$ and a_1/a_2 for *Xoo* ($L/\bar{a} = 12.58$ and $a_1/a_2 = 1.88$) place the bacterium within the model category of stable motion parallel to the vessel walls. The predicted localization proposes low shear stress, where upstream movement of *Xoo* would energetically be less demanding [139]. Experimental validation will be needed to determine whether *Xoo* is indeed in a stable motion parallel to the xylem walls and if *Xoo* actively modulates its position in response to flow conditions.

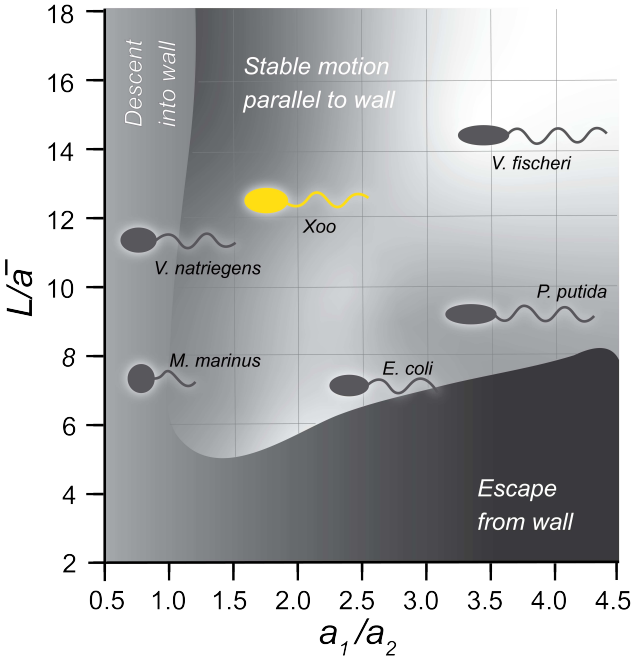

Figure 4.1: Adapted motility model for predicting *Xoo* motility. Swimming trajectories of *Xoo* (yellow) were predicted based on cell body and flagellum dimensions calculated in Table 4.1. Trajectories of previously characterized species were retained for reference [66]. The model offers three categories, which are represented in different gray shades: descent into wall, escape from wall and stable motion parallel to the wall. $L/\bar{a}$ denotes the non-dimensional flagellum length divided by radius of a sphere with the volume of the cell body; a_1/a_2 describes the aspect ratio of the cell body, defined as polar radius divided by equatorial radius. The model is adapted from Tokárová et al. 2021 [66]

4.2 Motility of *Xoo* in microfluidic chambers

Bacterial movement is primarily mediated by flagella and pili, which enable distinct forms of motility including swimming, swarming, or twitching [140]. To assess whether the predicted motility behavior of *Xoo* (Chapter 4.1) enables upstream movement under flow conditions, we used a microfluidic platform designed to mimic the xylem. The rice xylem pathogen *Xoo* is known to carry a polar flagellum [47], but it remains unsolved whether the resulting swimming motility enables *Xoo* cells to move against a stream, such as the xylem stream during infection.

The microfluidic chip was designed by Witting et al., 2025 [138] and provided through a collaboration with Dietrich Kohlheyer (Forschungszentrum Jülich). In the chip, each unit consists of a central diffusion chamber connected to two lateral flow chambers. *Xoo* was cultured in NB medium (1 g/L yeast extract, 3 g/L beef extract, 5 g/L peptone, pH 7) supplemented with 30 mM sucrose at 28 °C and 200 rpm until

the exponential phase was reached (OD_{600} 0.3). The cells were gently introduced into the chip and incubated at 22 °C.

To confirm that motility is retained in the microfluidic chip, the cells were first introduced in the absence of flow. Without current, *Xoo* showed active movement in all dimensions within the chamber (data not shown), thus validating the usability of the chip. We then applied a constant, unidirectional medium flow rate of 100 nL/min. The majority of cells were passively carried away by the stream or actively swam along the flow axis. Notably, a few cells moved against the current (Figure 4.2). These results indicate that *Xoo* can generate sufficient motile force to overcome weak flow conditions. Why many cells did not show movement against the stream remains

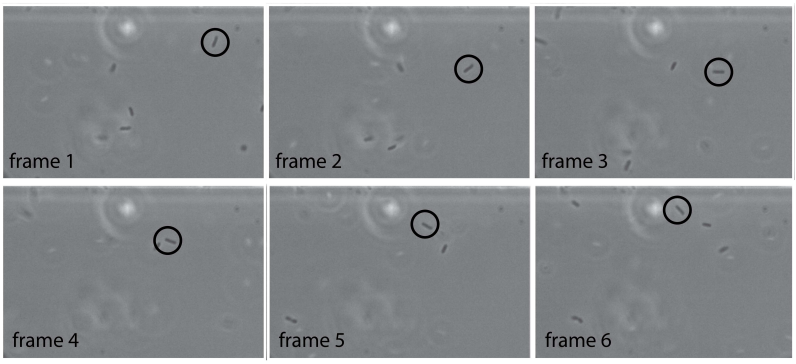

Figure 4.2: Upstream motility of *Xoo* in microfluidic chambers. A constant medium flow rate of 100 nL/min was applied to a microfluidic chamber, which was filled with *Xoo* cells. Six consecutive frames show exemplary upstream motility by *Xoo* (encircled cell). The air bubble visible is located on a different z-plane and does not interfere with the cells, but can be used as reference point.

elusive. Also, this artificial system does not replicate the structural or biochemical properties of xylem vessels and the applied flow rate is below the xylem velocities reported *in planta*. Yet, xylem flow rates vary with transpiration and time of day, with typical velocities ranging from 0.4 to 1.0 mm/s [14]. Based on the fact that a few cells were able to withstand the current, we hypothesize that under favorable conditions such as night, *Xoo* motility may enable upstream infection. To further study *Xoo* motility in microfluidic chambers, it has to be tested whether *Xoo* can adhere to microfluidic surfaces via pili or fimbriae. *Xylella fastidiosa* migrates without a flagellum against the xylem stream at approximately 5 μm/min via pili-driven twitching, even against a flow rate of 20,000 μm/min in microfluidic chambers [61]. This highlights the potential relevance of adhesion mechanisms in infection. This experiment provides crucial evidence that upstream movement against low flow rates is possible for *Xoo in vitro*, how *Xoo* can migrate against the xylem flow *in planta* remains to be studied.

4.3 The role of xylem flow for *Xoo* infection

The primary infection sites of *Xanthomonas oryzae pv. oryzae* are the xylem vessels of rice leaves [5, 78]. Together with the phloem, the xylem forms the plant vasculature, which connects source and sink organs. While the phloem transports photosynthates from leaves to roots, xylem sap moves in the opposite direction - from the base toward the leaf tip. Based on the directionality of xylem flow, one might expect disease symptoms to progress in the same direction. However, during Bacterial Blight, lesions expand in the reverse direction, from the tip toward the base. To assess the role of the xylem flow directionality in disease progression, we developed an assay that preserves the integrity of the natural xylem stream, in contrast to classical leaf clipping methods.

To avoid artificial disruption of vessel flow and to investigate the role of the xylem flow on disease progression, we developed an infection assay that preserves the integrity of the xylem stream. This approach differs from the classical Kauffmann leaf-clipping method [88], which cuts off vascular tissues and disrupts xylem continuity. For the modified assay, *Oryza sativa* ssp. *japonica* cv. *Kitaake* was cultivated under controlled greenhouse conditions (12 h light at 28 °C; 12 h dark at 25°C; 80% relative humidity). Fully expanded leaves of at least 20 cm in length were gently abraded using fine sandpaper at a position approximately 10 cm below the leaf tip. The wound was treated with a bacterial suspension of *Xoo* strain PXO99^{A} (OD_{600} of 0.6) or sterile water as control; untreated wounds were included to assess the effects of mechanical wounding alone. Lesion development was monitored for 12 days post-inoculation (dpi), with lesion lengths recorded separately in the acropetal (with the xylem stream) and basipetal (against the stream) directions.

In an initial experiment, PXO99^{A}-inoculated leaves exhibited lesions mainly in the direction of the xylem flow. In most cases, lesions reached the leaf tip before the measurement time point (Figure 4.3A). To increase resolution, the infection period was shortened from 12 to 10 days, and longer leaves were selected with an inoculation site 20 cm below the leaf tip (Figure 4.3B). Under the improved conditions, average lesion lengths were 15.9 cm in the acropetal direction and 5.2 cm in the basipetal direction (Figure 4.3C). Neither water-treated leaves nor untreated controls developed lesions of more than 1 cm in length. This result indicates that *Xoo* can infect rice passively with the stream and also actively against the xylem stream.

While classical clipping assays provide information limited to a single spatial axis, the sandpaper-infection assay enables observation of lesion expansion in both acropetal and basipetal directions. In clipping experiments, lesions progressed uniformly from

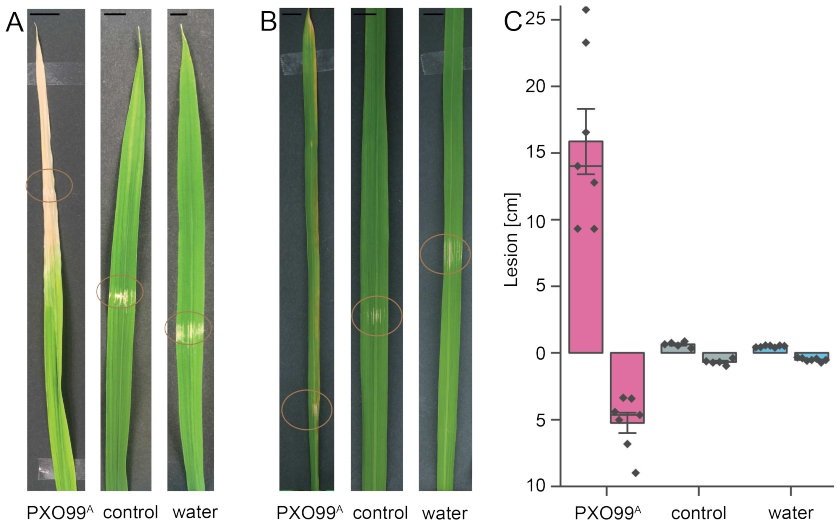

Figure 4.3: Sandpaper-mediated infection of *Kitaake* rice leaves. A Representative lesions observed under the initial infection settings (12-day infection period, shorter leaves). **B** Representative lesions observed under optimized conditions (10-day infection period, longer leaves). **C** Quantification of lesion lengths under optimized conditions. Sandpaper-wounded leaves were treated with PXO99^A (yellow, $n = 7$) or sterile water (blue, $n = 7$); untreated plants served as a wounding control (grey, $n = 5$). Lesion lengths were measured both acropetally (above the wounding site at 0 cm, i.e., in the direction of xylem flow) and basipetally (below 0 cm, i.e., against the xylem flow). Circles mark wounding sites. Bars represent mean ± SEM; horizontal lines indicate the median.

the wound site, consistent with previous reports [88]. By contrast, the sandpaper-based assay revealed directional differences in lesion development. Lesions extending with the xylem stream were approximately threefold longer than those expanding against it. This directional bias indicated distinct mechanisms underlying acropetal and basipetal colonization.

One possible explanation is that cells migrating against the xylem stream may rely on adhesion and active motility, whereas cells moving with the stream might exploit passive transport, as seen in Chapter 4.2. To test this hypothesis, sandpaper-infection assays using *Xoo* mutants deficient in swimming motility or adhesion could allow a deeper understanding. Another contributing factor to the directional bias in lesion development may be biofilm formation during xylem infection. In *Xoo*, biofilm production is promoted by host-derived sugars such as sucrose and xylose [8, 41]. Accumulating biofilm can clog xylem vessels and reduce sap flow [141]. A decline in xylem current could allow further basipetal colonization.

CHAPTER 5

Unraveling the host-pathogen interaction between rice and *Xoo* with dualRNAseq[5]

5: The content of this chapter provides a preview of ongoing analyses.
I contributed approximately 90 % to this project, primarily through study design and wet-lab work, including growing plants, cultivating bacteria, performing infections, collecting samples and preparing samples for sequencing. cDNA library preparation and sequencing were carried out at Novogene. Data analysis is currently being performed by Jacob Sharkey. This chapter was written by me.

5.1 Introduction

Global rice production is threatened by a range of diseases, including Bacterial Blight, caused by the bacterium *Xanthomonas oryzae pv. oryzae* (*Xoo*) [1, 4, 68]. This disease alone contributes to an estimated 8.5 % yield loss in the Indo-Gangetic plain [68]. As rice is a staple food for half the world, its diseases pose direct threats to global food security [68].

Xoo is a vascular pathogen that enters the plant through wounds or hydathodes, leading to colonization of the xylem and subsequent basipetal spread [4]. During infection, *Xoo* shifts from planktonic growth to colonization by producing exopolysaccharides and forming biofilms [141]. At the same time, the bacterium delivers transcription activator-like (TAL) effectors via the type III secretion system into host cells [33]. TAL effectors translocate to the host nucleus and bind specific promoter sequences, inducing the transcription of target genes. The most prominent TAL effector, *PthXo1*, activates host sucrose transporter genes such as *SWEET11a*, promoting sucrose efflux that drives bacterial growth [11, 12].

While individual aspects of the infection are well characterized, they do not explain how host and pathogen adapt transcriptionally towards each other during the different infection stages [142]. We hypothesize that along the infection gradient, *Xoo* and rice undergo a series of coordinated transcriptional transitions. We further hypothesize that these shifts recur at successive colonization steps, indicating a spiral-like infection strategy. Despite the dynamic nature of host–pathogen interactions, most studies focus on either the host or the pathogen in isolation [143, 144]. DualRNAseq captures transcriptional changes of both organisms in a single reaction, enabling detailed insights into the infection process. A previous dualRNAseq study in *Xoo* sampled only early stages of the disease, limiting insight e.g. into the biotrophy–necrotrophy transition [142]. Moreover, spatial resolution has been largely neglected, even though it can reveal tissue-specific infection dynamics.

Here, to address these gaps, we dissected the infection process in a spatio-temporal manner. Multiple sections along infected leaves were collected at successive time points to resolve both temporal and spatial dynamics. This approach will enables us to distinguish temporal from spatial aspects of disease progression and transcriptional reprogramming at the infection front from that at the base.

5.2 Methods

Plant and bacterial cultivation

Oryza sativa ssp. japonica cv. Kitaake plants were grown in a plant growth chamber at 80 % humidity with 12 hours light at 28 °C and 12 hours in darkness at 25 °C. In order to perform a dualRNAseq experiment, plants showing symptoms of any disease or nutrient limitations before treatment were excluded from the experiment. *Xanthomonas oryzae pv. oryzae* strains PXO99^{A} and PXO99^{ME2} were cultivated at 28 °C in optimized nutrient broth (NB) media (1 g/L yeast extract, 3 g/L beef extract, 5 g/L peptone, pH 7) to a low exponential phase with an OD_{600} of 0.3.

Clipping infection assay

Healthy, four-week old *Oryza sativa ssp. japonica cv. Kitaake* plants were inoculated with bacterial suspensions of PXO99^{A} or PXO99^{ME2} using the established leaf tip-clipping method [88], while water-treated plants served as controls. In brief, a sterile scissor was dipped into bacterial solution with OD_{600} of 0.3 or water and the tip of a rice leaf was cut off. Successful disease development was verified via lesion length measurements. Lesion lengths were observed at defined time points of 6 hours, 3, 6, 9, and 12 days post-inoculation. The first 2 cm of the leaf below the cut off site were discarded and three leaf segments (A, B, C) of 2 cm each were harvested (Figure 5.1). For each time point, five leaf segments (A, B, or C) from five infected leaves of a single plant were pooled to form one biological replicate. Three biological replicates were collected for each of the two independent experiments.

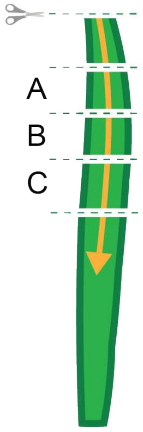

Figure 5.1: Schematic representation of a rice leaf after clipping infection, showing the segmentation of leaf tissue into A, B, and C sections for sample collection.

Library preparation and RNA sequencing

Infected plant material was ground under liquid nitrogen supply using mortar and pestle. Bacterial and plant RNA were extracted from the samples using the RNeasy Plant Mini kit (74904, Qiagen). Bioanalyzer assays were used to assess the RNA quality (DNF 471, Genomics & Transcriptomics Labor Duesseldorf). Samples with a quality value (RQN) below 6 were excluded. Extracted RNA was provided to

Novogene for rRNA depletion, library preparation and RNA sequencing. Ribosomal RNA was removed based on a RNase H depletion workflow.

RNA sequencing analysis

RNAseq analysis was performed by Jacob Sharkey (Figure 5.2). In brief, FASTQ files were mapped to a rice reference genome (Kitaake) which was combined with a PXO99^{A} *Xoo* reference genome as an artificial chromosome using the Spliced Transcripts Alignment to a Reference (STAR) software. The number of reads per gene for rice and *Xoo* were quantified with HTSeq. Further, differentially expressed genes between plants inoculated with water, PXO99^{ME2}, and PXO99^{A} were identified with the R-packages EdgeR and visualized using Volcano3D. Differences were considered significantly where the adjusted p-value was below 0.05 and log2(FC) was greater than 1 or less than –1 for plant and bacterial samples.

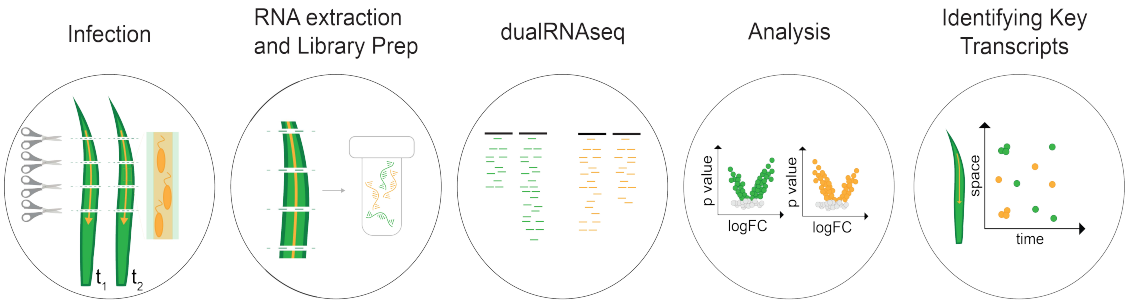

Figure 5.2: Schematic representation of sample preparation and dualRNAseq analysis.

5.3 Results

Validation of the disease development and dualRNAseq dataset

To capture the molecular interactions during Bacterial Blight of both partners, we applied a dual transcriptomic approach that simultaneously quantifies mRNA transcripts of rice and its pathogen *Xoo*. Each library was sequenced to a depth of 15 GB, providing sufficient coverage to capture transcripts from both rice and *Xoo* within a single sample. Read numbers ranged from 16 to 30 million per library. An initial mapping strategy ("host first, pathogen following" [145]) produced false-positive assignments of *Xoo* reads to the rice genome. To eliminate misclassifications, an artificial rice–*Xoo* reference chromosome was constructed and used for all subsequent alignments.

Susceptible *Oryza sativa ssp. japonica cv. Kitaake* plants were inoculated with the virulent strain PXO99^{A}, the avirulent strain PXO99^{ME2} or water. PXO99^{ME2} lacks the TAL effector *PthXo1* and does not induce the host *SWEET11a* gene. Lesion assays confirmed that PXO99^{A} caused developing lesions, whereas PXO99^{ME2} and water treatment produced only localized tissue damage that did not extend into the first sampling segment (Figure 5.3). To validate the RNAseq dataset

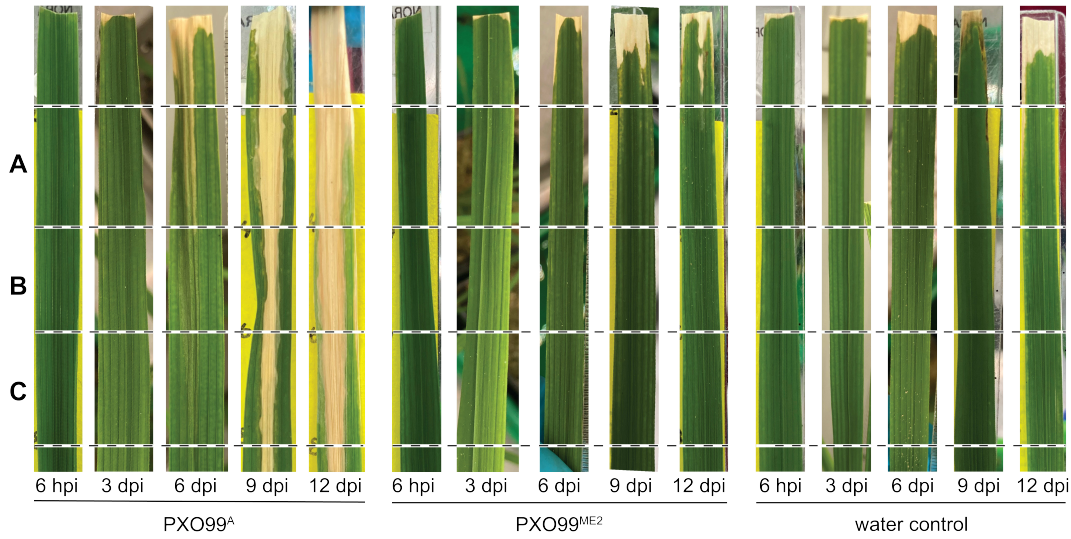

Figure 5.3: Time course of rice leaf infection following clipping assays with PXO99^{A} and PXO99^{ME2}. Representative leaves are shown at 6 hours, 3, 6, 9, and 12 days post-inoculation. Sampling segments A, B and C are indicated, as well as the the discarded top region. PXO99^{A} caused progressive lesion development, whereas PXO99^{ME2} and water controls produced only localized damage at the leaf tip.

and confirm treatment-specific host responses, we examined transcript levels of

SWEET11a, a susceptibility gene previously reported to be activated by the TAL effector *PthXo1* delivered by PXO99^{A} [33]. Accordingly, induction was expected only in PXO99^{A}–infected plants, but not in plants treated with PXO99^{ME2} or water. Transcriptional changes were assessed in segment A at 6 hours, 3 days, and 6 days post-inoculation. In line with our hypothesis, no changes were observed after PXO99^{ME2} or water treatment at any time point. Also PXO99^{A} did not alter *SWEET11a* transcript levels at 6 hours, but caused a strong increase at 3 and 6 days. These results confirm that the dataset reliably captures host–pathogen transcriptional dynamics and provides a validated foundation for downstream analyses.

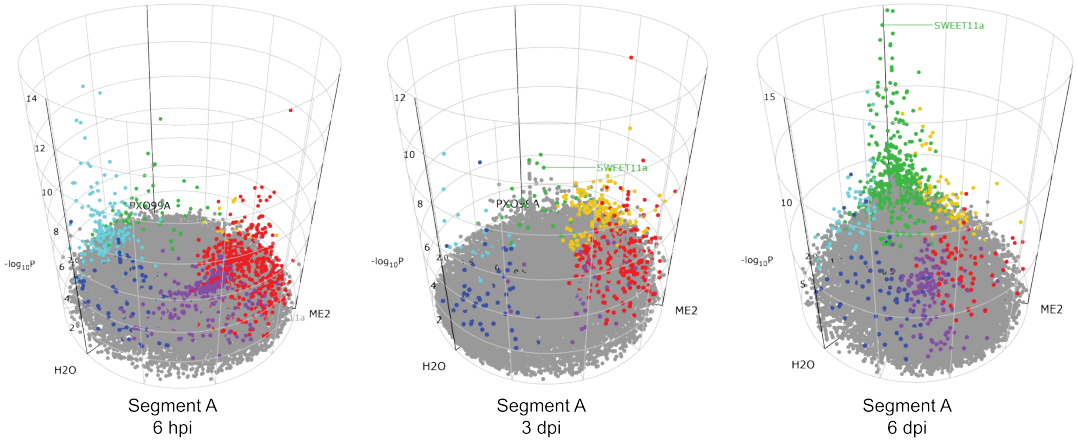

Figure 5.4: Validation of RNAseq dataset by monitoring *SWEET11a* expression. Transcript abundance of *SWEET11a* was quantified in rice leaves treated with PXO99^{A}, PXO99^{ME2}, or water at 6 hours, 3 days, and 6 days post-inoculation. Significant increase in transcripts was detected exclusively in segment A of PXO99^{A}-treated plants at 3 (middle) and 6 (right) days, whereas PXO99^{ME2} and water controls showed no induction at any time point. Further samples and segments have not been analyzed yet. Three-dimensional volcano plots depict differentially expressed genes across the three treatments. The z-axis represents –log$_{10}$ p-values from the likelihood ratio test between conditions. Genes with an adjusted p-value < 0.05 (z-axis) were considered significant; non-significant genes are shown in gray. Colors indicate pairwise comparisons (FDR < 0.05) between treatments: primary colors highlight genes with increased transcripts in a single group: water (blue), PXO99^{ME2} (red), or PXO99^{A} (green), relative to the reference group with minimum expression. Composite colors indicate genes with significantly increased transcripts in two groups.

Spatial *Xoo* transcriptome dynamics during Bacterial Blight

To resolve spatial aspects of disease progression and track bacterial transcriptional changes within a single leaf, we analyzed the *Xoo* transcriptome in segments A, B, and C from the 6-day samples. The top 24 KEGG pathways, represented by differentially expressed genes, covered diverse functional categories. Many pathways are associated

with metabolic processes, including sulfur metabolism, carbon metabolism, and starch and sucrose metabolism, while others relate to cellular functions such as two-component signaling, secretion systems, and biofilm formation (Figure 5.5). Along the infection gradient, defined by the three segments, transcript levels for exopolysaccharide biosynthesis tended to increase, whereas transcript levels for starch and sucrose metabolism decreased. These shifts indicate how the dataset can be used to trace changes in bacterial physiology across spatial niches, with potential transitions from nutrient utilization toward EPS-associated functions. Ongoing analyses of the underlying genes and pathways will provide a more detailed picture of spatial infection dynamics.

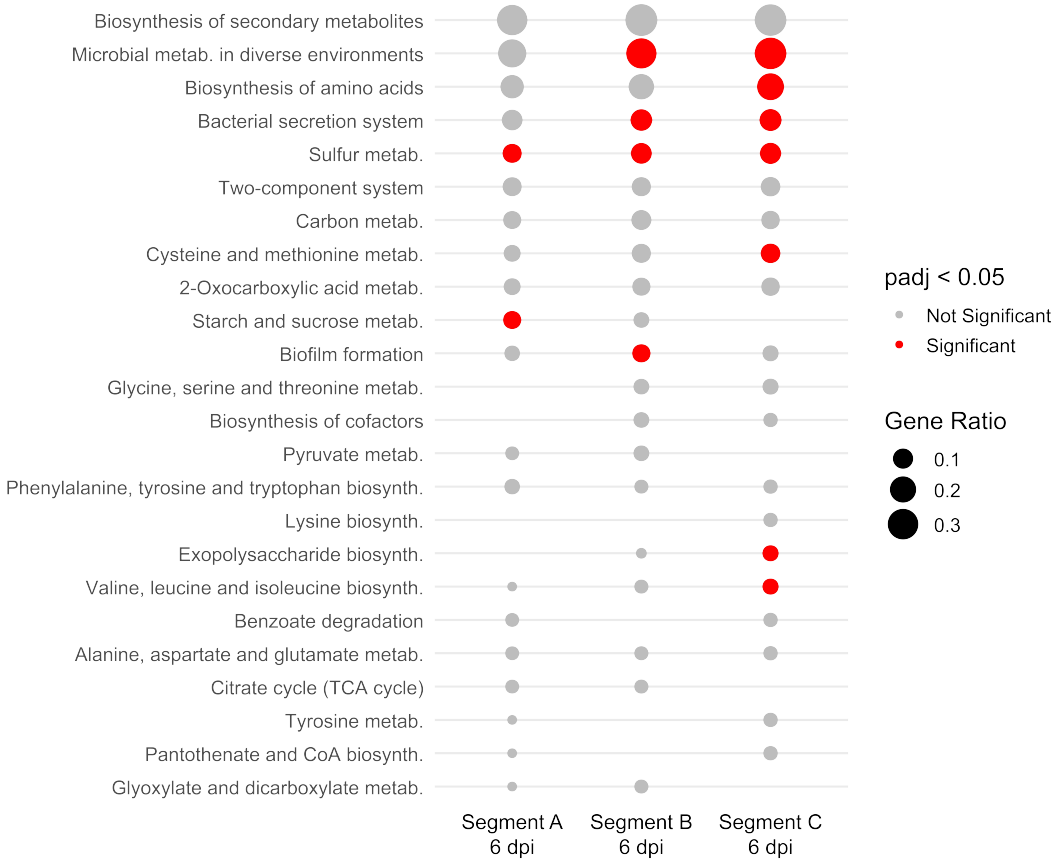

Figure 5.5: KEGG pathway enrichment analysis of *Xoo* transcription across spatial niches of infected rice leaves. The top 24 KEGG pathways, represented by differentially expressed genes, were identified in leaf segments A, B, and C at 6 days post-inoculation. Circle size indicates the ratio of differentially expressed genes within each pathway, and color denotes significance (red: adjusted p-value < 0.05; gray: not significant).

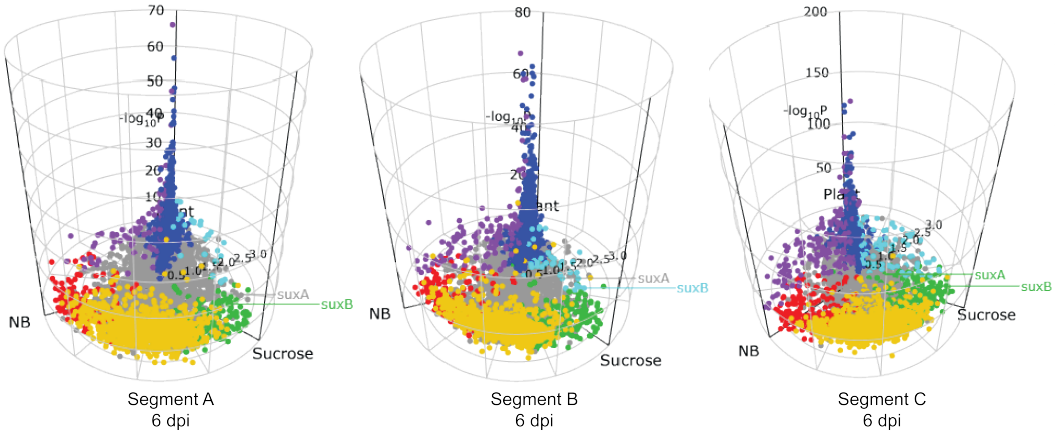

Figure 5.6: Spatially resolved transcriptional responses during Bacterial Blight by *Xoo*. Differential gene expression in *Xoo* was analyzed in leaf segments A, B, and C at 6 days post-inoculation. Three-dimensional volcano plots depict differentially expressed genes across the spatial gradient, with the z-axis representing $-\log_{10}$ p-values from the likelihood ratio test between conditions. Genes with adjusted p-value < 0.05 are shown in color, nonsignificant genes in gray. Colors indicate pairwise comparisons (FDR < 0.05) between segments. Exemplary genes of the sucrose utilization cluster, *suxA* and *suxB*, are highlighted.

Profiling of host-induced transcript dynamics

To identify *Xoo* transcripts specifically induced in the host environment, we compared the dualRNAseq dataset with our previously generated *in vitro* RNAseq results [41]. Through comparing the sets, we found transcripts uniquely changed in abundance through the *in planta* environment. Further, comparison allowed identification of sucrose-induced changes in transcript abundance. A prominent candidate for sucrose- and host-induced transcript increase were members of the sucrose-uptake cluster in *Xoo*, which we described in Chapter 2. In temporal alignment with the previous observed transcript increase in *SWEET11a* sucrose transporter genes, genes of the *suxAB* operon were detected (Figure 5.6). The concomitant increase in transcripts for host *SWEET11a sucrose transporter* genes and pathogen *sux sucrose uptake* genes indicates a direct feeding mechanism of the pathogen.

Next to sucrose- and host-induced transcript changes, we also observed changes that uniquely react to the host environment. In PXO99^A-inoculated plants, we observed an increase of virulence effectors from segment A 3 days post-inoculation on, including the TAL effector *PthXo1*, which was not observed in the *in vitro* dataset. This transcriptional increase is noteworthy, as *PthXo1* was generally considered low-level constitutive although neither constitutive nor inducible expression of *PthXo1* had been reported previously [51, 107]. Inducible effectors typically carry a plant inducible promoter (PIP) motif, but no canonical PIP box has been identified

upstream of *PthXo1*, potentially due to the absence of Shine-Dalgarno elements in many *Xanthomonas* species [146].

5.4 Discussion

This study presents a dualRNAseq dataset capturing transcriptional changes in both rice (*Oryza sativa*) and *Xanthomonas oryzae pv. oryzae* (*Xoo*) during Bacterial Blight. Although our analysis is preliminary, the dataset already demonstrates treatment-specific responses, validating its utility for dissecting host–pathogen interactions. Initial validation focused on the susceptibility gene *SWEET11a*, activated by the PXO99^A TAL effector *PthXo1*. Consistent with previous work [147], *SWEET11a* transcripts increased exclusively in PXO99^A-inoculated plants from 3 days post inoculation, indicating that early infection is dominated by pathogen colonization rather than by immediate host reprogramming.

A first look at the *Xoo* transcriptome across leaf segments revealed spatially structured transcriptional reprogramming. Metabolic genes were elevated near the infection base, whereas genes for exopolysaccharide (EPS) production and secretion systems increased toward the infection front. These patterns indicate a transition from nutrient acquisition to colonization across infection zones.

In the host environment, bacterial sucrose uptake transcripts (including the *suxAB* operon [41]) showed changes overlapping with *SWEET11a* transcripts, supporting the hypothesis of a feeding mechanism. We further observed that transcripts of the TAL effector *PthXo1* increased in the host environment, although it was previously considered constitutive [33, 147]. Although the dataset has not yet been fully analyzed, it already demonstrates potential to reveal novel insights into the spatio-temporal coordination of host and pathogen transcripts.

In contrast to previous dualRNAseq studies in *Xoo* [142, 145], this study adds spatial resolution, capturing defined leaf segments. Later disease stages of infection, including lesion development, were studied, which is crucial for understanding the transition e.g. from biotrophic to necrotrophic pathogen lifestyles [4]. Ultimately, the dualRNAseq dataset provides more than a static snapshot: it captures the molecular network driving Bacterial Blight and offers a framework for exploring complex host–pathogen–microbiome interactions.

CHAPTER 6

Evidence for rapid hydrolysis of shoot-derived sucrose using an ultrasensitive ratiometric Matryoshka-type MGlucoMeter sensor[6]

6: This chapter is based on the article *Evidence for rapid hydrolysis of shoot-derived sucrose using an ultrasensitive ratiometric Matryoshka-type MGlucoMeter sensor* by Yuuma Ishikawa, **Nora R. Zöllner**, and Wolf B. Frommer, which is currently in preparation.

I contributed approximately 15 % to this project, primarily by co-writing the manuscript with WBF, analyzing and validating constructs and sequencing results, and assisting with fluorimetric analyses using the TECAN.

Abstract

To enable sensitive *in vivo* monitoring of the glucose transport and metabolism, we developed a series of ultrasensitive and ratiometric genetically encoded nanosensors by inserting a Matryoshka dual fluorophore cassette consisting of cpsfGFP and LSSmApple into the glucose binding protein *Tt*GBP from *Thermus thermophilus*. The initial MGlucoMeter1.0 was subjected to an alanine scan of the hinge region producing more sensitive MGlucoMeter2.6 with a glucose-induced $\Delta F/F_0$ change of 3.0, an affinity for glucose of 15 μM, and an approximate detection range of 1.1-216 μM. To generate variants suitable for *in vivo* measurements, a series of affinity mutants was generated by mutating two histidines predicted to be involved in substrate binding. MGlucoMeter2.6-353n, MGlucoMeter2.6-15 μ, MGlucoMeter2.6-700 μ, MGlucoMeter2.6-1m, and MGlucoMeter2.6-7m cover a detection range between $\sim$40 nM and 55 mM. When expressed from a ubiquitous promoter in the cytosol of the Arabidopsis gene silencing mutant *rdr6*, MGlucoMeter2.6-1m reports time- and concentration-dependent accumulation of glucose in seedling roots. The sensor also detects rapid hydrolysis of shoot- derived sucrose in the root tip.

6.1 Introduction

While metabolomics provides quantitative information on the steady state levels of metabolites, it lacks spatial and time resolution. An alternative is the visualization of metabolite dynamics with subcellular resolution using genetically encoded nanosensors. The first sugar sensors were developed by sandwiching a sugar binding proteins from the family of bacterial periplasmic binding proteins between two variants of the green fluorescent proteins that had features allowing for Förster Resonance Energy Transfer [148–151]. These sensors were successfully used for monitoring glucose dynamics in bacterial and yeast cells, mammalian cells and in the plant Arabidopsis [152–156]. The glucose sensors were also successfully deployed for genetic screens to identify networks involved in the regulation of glucose transport and for studying the transfer of glucose across ER membranes [149, 157–159]. While the FRET-based approach yielded sensors suitable for *in vivo* measurements, the sensitivity of the sensors was limited due to the intrinsic coupling of the relative change in the emission of the two fluorophores. Roger Tsien had developed an alternative approach using a circular permutated GFP as an intensiometric reporter element [160]. Although the sensitivity of the intensiometric cpGFP-based sensors was higher, the FRET sensors had one major advantage: they were ratiometric and thus not impacted by changes in the sensor levels. To overcome the limitation, calcium and ammonium transporter activity sensors were generated that contained a nested large Stokes shift fluorophore (LSSmOrange) as a reference, enabling ratiometric measurements [161, 162]. The calcium sensor was further improved by replacing LSSmOrange with the better suited LSSmApple [163]. Since proteins from thermophilic organisms are more robust, the glucose-binding protein from *Thermus thermophilus* had previously been used to generate an intensiometric glucose sensors by inserting cpGFP into *Tt*GBP to produce iGlucoSnFR [164]. Here, a series of ultrasensitive glucose sensors (MGlucoMeter) was generated using the Matryoshka technology. For this purpose, the previously developed Matryoshka cassette, consisting of the superfolder variant cpsfGFP as a sensory domain and LSSmApple as a reference fluorophore [163], was inserted into the glucose binding protein *Tt*GBP from *Thermus thermophilus*. The initial sensor was further optimized by linker mutagenesis, and site directed mutagenesis was used to produce a series of affinity mutants. MGlucoMeter2.6-1m with an affinity of 1 mM for glucose was then used to monitor the accumulation of glucose in Arabidopsis roots as well as the accumulation and transport of glucose in Arabidopsis seedling roots after supply of sucrose to shoots.

6.2 Material and methods

Construction of MGlucoMeter

MGlucoMeter2.0 were generated from the initial construct MGlucoMeter1.0 (Sadoine et al., 2025), which carries an insertion of the cpsfGFP-LSSmApple cassette from GA-MatryoshCaMP6s into the hinge region of *Tt*GBP from *Thermus thermophilus* in the pRSETb T7 expression vector (Thermo Scientific; V35120) [163, 165] (Figure 6.1, Table 6.1). The expressed gene product (P0328) of *Tt*GBP lacks the 21-bp leader sequence [165]. An alanine scan of the linker and hinge region (amino acids targeted left linker/hinge region: DSDPSKYPASH; right linker/hinge region FNNPNAYGQSAM) was performed by inverse PCR (Figure 6.1, Table 6.1). PCR products were amplified using PrimeSTAR GXL (Takara Bio; R050B) (Table 6.5). The resulting product was cleaned up by gel extraction using the NucleoSpin column kit (Macherey-Nagel; 740609). Affinity variants were generated by introducing single point mutations into *Tt*GBP. All sequences were confirmed by DNA sequencing (Microsynth SEQLAB). Plasmids containing the MGlucoMeter2.6 affinity mutants are available from AddGene (www.addgene.org).

Expression and purification of the MGlucoMeter

E. coli BL21 (DE3) [fhuA2 [lon] ompT gal (λ DE3) [dcm] ΔhsdS; λ DE3 = λ sBamHIo ΔEcoRI-B int::(lacI::PlacUV5::T7 gene1) i21 Δnin5] (New England Biolabs; C2527I) was transformed with pRSETb containing MGlucoMeter plasmids. Single colonies were inoculated into 3 mL of LB medium (Duchefa Biochemie; 4800-94-6) containing 50 μg/mL carbenicillin (Sigma-Aldrich; C1389) in glass tubes (Hardy diagnostics; 1517) and incubated at 37 °C with shaking at 200 rpm for 14-18 h. 2 mL of the starter culture were transferred into 100 ml LB medium containing 50 μg/mL carbenicillin disodium, 0.2% D-lactose (Sigma-Aldrich; 64044-51-5), and 0.05% D-glucose monohydrate (Thermo Scientific Chemicals; 14431-43-7) in 500 mL Erlenmeyer flasks without baffles (SciLahware; 1135/26D). After 2 h of incubation at 37 °C with shaking at 200 rpm, cultures were transferred to a 20 °C incubator with shaking at 200 rpm and incubated for 48 h. Bacterial cultures were cooled on ice and centrifuged at 3,790 x *g* for 10 min at 4 °C. The cell pellet was stored at –20 °C for at least 14 h. After thawing on ice, the pellet was resuspended in 1.5 mL of 20 mM MOPS (Roth; 1132-61-2), pH 7.0. To prevent sensor degradation, one cOmplete ULTRA Tablet Mini protease inhibitor cocktail (Merck; 1183670001) was added per 100 mL of all purification buffers. Cells were lysed by sonication at 50 amplitude

(QSonica Q700 Sonicator), with a total processing time of 45 s (3 s pulse on, 8 s pulse off). The sonicated sample was centrifuged at 15,871 x g for 10 min at 4 °C to remove cellular debris. His-tagged MGlucoMeter sensor proteins were purified using Ni-NTA agarose beads (Qiagen; 30210). Prior to lysate application, 1.5 mL of Ni-NTA agarose beads was loaded onto a column and washed with 10 mL of 20 mM MOPS, pH 7.0. After the loading of the lysate, the column was washed again with 10 mL of 20 mM MOPS, pH7.0. His-tagged MGlucoMeter protein was eluted with 1.5 mL of 250 mM imidazole (Sigma-Aldrich; 1467-16-9) and 20 mM MOPS, pH 7.0. Protein concentration was determined by a NanoDrop One (Thermo Scientific). Purified sensors were incubated at 4 °C for at least 14 h to ensure maturation of the fluorescent protein.

Fluorimetric analysis of MGlucoMeter2.0 sensors

For each well, 10 μL of sensor solution was mixed with 190 μL of buffer. Ligand titrations were performed using a TECAN Spark microplate reader (Tecan Austria GmbH; 704004367). Steady-state fluorescence spectra were recorded with excitation wavelength at 453 ± 20 nm and emission from 499 to 700 nm in 2 nm steps, using a 50% mirror. Measurements were recorded in the top-reading mode with a gain of 80–130 and the temperature controlled at 27 ± 0.5 °C. Spectra were background-subtracted using 20 mM MOPS containing 250 mM buffer (pH 7.0). Analysis was performed in 96-well clear, flat-bottom, microplate (Corning; 3370). Fluorescence emission ratios were calculated as cpsfGFP emisson intensity (λex 480 nm, λem 515 nm) divided by LSSmApple emission intensity (λex 460 nm, λem 600 nm). The baseline ratio defined as R_0 and the ratio at increasing ligand concentrations as R. Data were normalized accordingly;

$$\frac{\Delta R}{R_0} = \frac{R - R_0}{R_0} \tag{6.1}$$

Data analysis and visualization of the data were performed using Excel, Origin Lab 2020, and Affinity Designer. Sigmoid curve fitting was performed with MyCurveFit. Values are reported as the mean ± standard error of $\Delta R/R_0$ or $\Delta F/F_0$ from n = 3 biological replicates (n = 3 technical replicates per biological replicates) out of two independent titrations. The dissociation constant (K_d) was defined as the ligand concentration at 50% $\Delta R_max/R_0$ in the fitted sigmoid function.

Cloning of MGlucoMeter2.6 constructs for expression in plants

MGlucoMeter2.6-1m was subcloned into pAY367-HTv443-UBQ10-Hspt binary vector (provided by Dr. A. Yoshinari, Institute for Transformative Biomolecules, ITbM, Nagoya University, Nagoya, Japan), which contains the Arabidopsis UBQ10 promoter and Hsp18.2 terminator. To insert MGlucoMeter2.6-1m, pAY367-HTv443-UBQ10-Hspt was digested with *Asc*I and *Apa*I restriction enzymes. Ligation reaction was carried out in the solution mixture containing 40 fmol DNA of the entry clones, 1x T4 DNA ligase buffer (Thermo Fisher; B69) and 5U T4 DNA ligase (Thermo Fisher; EL0012) in a total volume of 20 μL (thermalcycler: 22 °C for 10 minutes). The Arabidopsis gene-silencing mutant *rdr6-11* [155, 166] was transformed using the floral dip method. Transformed plants were selected on 50 μg/ml kanamycin and 2.35 mM MES containing 1/2 salt strength Murashige and Skoog (MS) medium (Duchefa Biochemie; M0255), adjusted to pH 5.7 with KOH, and solidified with 1% agar (Merck; 05040).

Plant growth conditions

Seeds were surface sterilized with 75% ethanol containing 0.08% Tween20, sown on 1/2 salt strength MS medium containing 2.35 mM MES, adjusted to pH 5.7 with KOH, and solidified with 1% agar. Plants were sealed with micropore tape and vernalized at 4 °C for 1 day. Plants were grown at 22 °C for 5 days after germination under the long day conditions (16 hours light/8 hours dark, light intensity was 110 μmol m^{-2} s^{-1}).

Root uptake kinetics measured with an automated perfusion system

MGlucoMeter2.6 seedlings were germinated, and 10-day-old seedlings were transferred to 1/2 salt strength MS medium in a 60 μ-Dish (Ibidi; 81158) and immobilized using double side adhesive tape (Tesa Tape; 05338). Seedlings were acclimated for 20 min by perfusion with mock buffer (1/4 salt strength MS containing 2.35 mM MES, pH 5.7) in the recording room. A peristaltic pump was used (Fisher Scientific; Cytiva 18-1110-91, flow rate; 2 mL/min) to perfuse the filtered 1/4 salt strength MS containing 2.35 mM MES (pH 5.7) liquid media to the whole seedling. Fully automated buffer exchange to 1 mM glucose containing 1/4 salt strength MS containing 2.35 mM MES (pH 5.7) liquid media was achieved using valve controller (Automate scientific; ValveBank Controllers). The hold-up time (delayed arrival of buffer in a fluid reservoir) was assessed in the perfusion set-up using a fluorescent

dye (ATTO 390; ATTO-TEC GmbH, AD 390-25). Hold-up time was calculated by taking the saturated fluorescence intensity as 100% and determining the time that required to reach 85% or 15% of that fluorescence intensity. An Olympus IXplore SpinSR spinning disk confocal microscope was used for imaging. Samples were excited with a 488 nm laser (Obis; 100mW, used at 10-30% power). The microscope was equipped with a Yokogawa confocal scanning unit (CSU)-W1 SoRa micro-lensed pinhole disk and an Olympus UAPON 10x UPL SAPO10x2. Emission intensities were collected in sequential stacks using a 525/50nm emission filter for GFP, 617/73 nm emission filter for LSSmApple. For detection, an Andor iXon Ultra 888 electron-multiplying charge coupled device (EMCCD) was used. Z-stacks were set by using a Mad City Labs Z-axis piezo nano positioner with 300 nm travel range (OLY-S1023-Nano-ZL300-OSSU). Full Z-stack acquisitions for each channel were performed at a frame rate of 1 min. The exposure time for each channel was 50 ms, with 4x4-pixel binning.

Quantitative imaging of glucose in roots in response to sucrose addition to shoots

Seedlings were acclimated for at least 2 h on 1% agar plates containing 1/2 salt strength MS and 2.35 mM MES (pH 5.7), sealed with micropore tape, in the recording room. Seedlings were placed on 1% agar plates containing 1/2 salt strength MS and 2.35 mM MES (pH 5.7) in a glass bottom chamber (Ibidi; μ-slide 1 well glass bottom). A flat PCR tube cap filled with 2M sucrose containing 1/4 salt strength MS containing 2.35 mM MES (pH 5.7) liquid media was placed in the glass bottom chamber, with the tip of cotyledon submerged in the sucrose solution (Figure 6.8). Quantitative glucose imaging was performed using a Zeiss AxioZoom V16 zoom microscope equipped with a X-Cite XYLIS LED Illumination System (XT720L), a 1 x objective lens (PlanNeoFluar Z 1 $\times$ /0.25 NA, FWD 56 mm, Zeiss, Oberkochen, Germany), and a Hamamatsu ORCA Flash4.0 CMOS camera. Zoom magnification was set between 7x and 10x, and pixel binning was set to 2 x 2 or 4 x 4-pixel binning for acquisitions. cpsfGFP fluorescence was detected using a filter cube with a 488/10 nm excitation filter, a 491 nm long-pass dichroic mirror, and a 519/26 nm emission filter. LSSmApple fluorescence was detected using a filter cube with a 488/10 nm excitation filter, a 514 nm long-pass dichroic mirror, and a 605/50 nm emission filter. A motorized xy stage (Zeiss) was used for time-lapse tiling acquisitions. Tiles were stitched using ZEN Blue 2.6 software (Zeiss). Z-step sizes were set equal to the optical section thickness (2-4 μm).

Image analyses

Segmentation and labeling were performed with the FRETENATOR plugins in Fiji [167]. Segmentation settings were optimized for each experiment. The GFP channel was used for segmentation. Watershed algorithm was used for the image segmentation. Difference of Gaussian kernel size was determined empirically due to different magnifications, resolutions and amount of noise. As a default, Otsu thresholds were used for segmentation in FRETENATOR.

6.3 Results and discussion

Development of new ultra-sensitive Matryoshka-type sugar sensors

Proteins from thermophiles often exhibit enhanced stability. For generating a Matryoshka-type glucose sensor, the glucose binding protein from *Thermus thermophilus*, for which crystal structure information is available, was selected as a recognition element [164, 165]. The glucose binding protein *Tt*GBP had been used to develop the intensiometric glucose sensor GluSnFR by inserting the *T. thermophilus* GBP lacking the leader peptide and a linker combination left linker-ProAla/right linker-AsnPro (L1-PA/L2-NP) between residues 326 and 327 of *Tt*GBP [164]. Analogous to the construction of GluSnFR, but here with the Matryoshka cassette consisting of cpsfGFP carrying an insertion of the Large Stokes Shift (LSS) mApple (LSSmApple) that had been used to generate MatryoshCaMP6s [163] was inserted into *Tt*GBP without the N-terminal signal sequence to generate MGlucoMeter1.0. The linkers that flank the fusion site between cpsfGFP and the recognition element are thought to be important for ESPT [168]. To further increase the sensitivity and detection range for *in vivo* measurements, the codons for amino acid pairs in the linker sequence flanking the Matryoshka cassette in MGlucoMeter1.0 were mutated. An alanine scan was performed corresponding to 19 amino acids surrounding the cpsfGFP insertion site; i.e. the hinge region of the glucose-binding domain, and linker sequences (FNNPNAYGQSAM/DSDPSKYPASH) (Figure 6.1a, Table 6.1). A set of 32 mutants carrying single, double or triple alanine replacements were characterized (Table 6.1). Fluorometric analysis of the glucose-induced ratio changes of the series indicated that some of the sensors lost responses, some showed altered affinities (Figure 6.1b). We selected one variant that showed the highest sensitivity MGlucoMeter2.6 ($\Delta F/F_0$ 3.0) for generating a series of affinity variants.

Generation of an affinity variants for MGlucoMeter2.6

Previous studies had shown that FLIPglu600μ with an affinity for glucose of 600 μM was well suited for recording glucose responses in Arabidopsis roots, we generated a series of affinity mutants of MGlucoMeter2.6 by site directed mutagenesis of candidate residues that interact with the glucose molecule: H66 and H348 (numbering based on the previously published sequence of *Tt*GBP (Figure 6.7; Supplementary Text) [154, 164, 165]. The resulting mutants exhibited affinities (K_d) for glucose of approximately 355 nM, 717 μM, 1 mM, 7.3 mM, respectively (Figure 6.2, Figure 6.3, Table 6.2). All affinity variants showed higher sensitivity ($\Delta F/F_0$ 1.90-3.69) compared to the

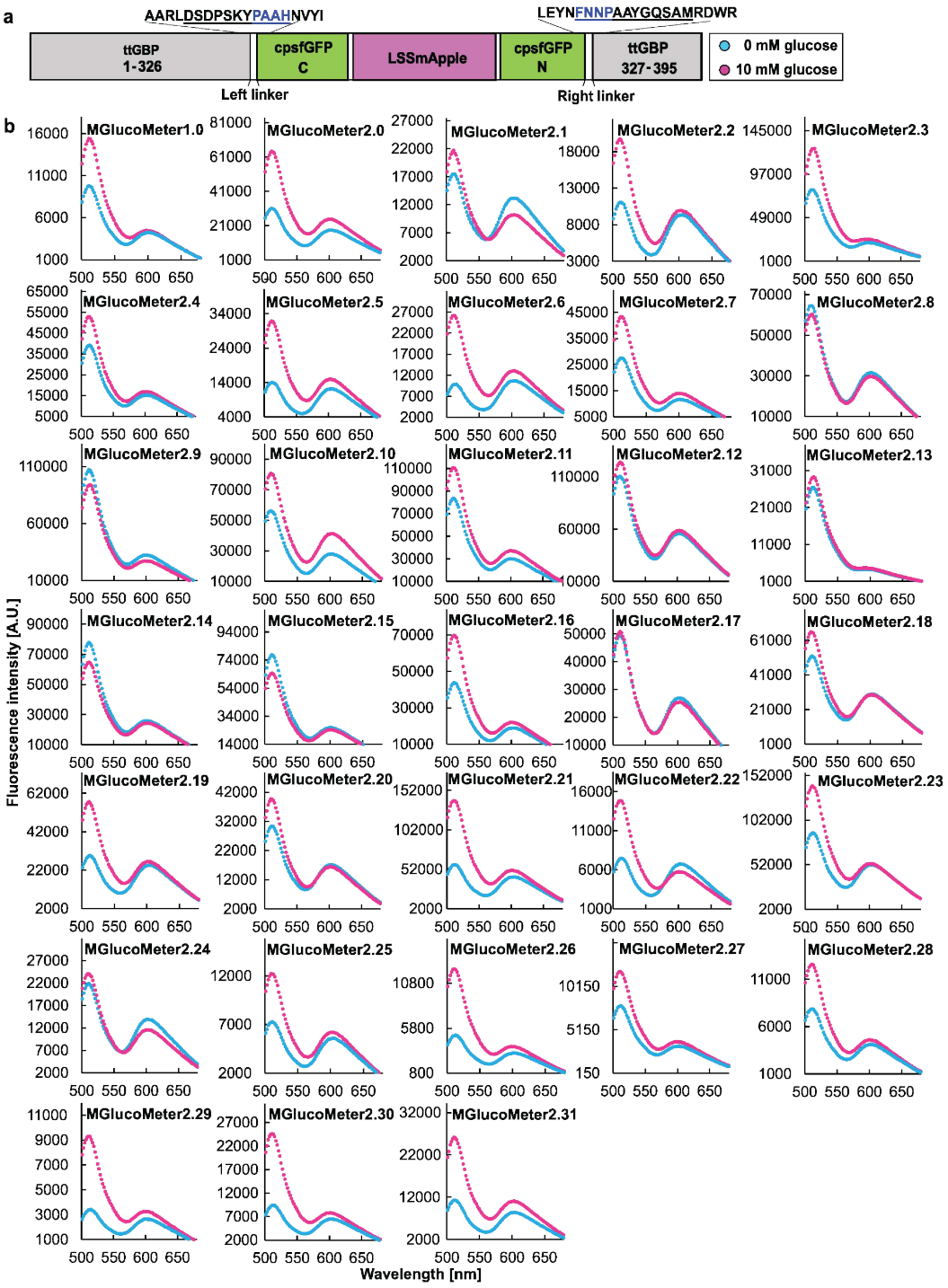

Figure 6.1: *In vitro* screening of MGlucoMeter variants with increased sensitivity. a. Construct map of MGlucoMeter2.6 carrying an insertion of the Green-Apple cassette (GA; cpsfGFP-LSSmApple) in *Tt*GBP. The amino acid residues substituted for MGlucoMeter are indicated as underlined. Four amino acid linker sequences connecting the Green-Apple cassette and *Tt*GBP are indicated with blue underline. **b.** The fluorescence responses of 32 purified MGlucoMeter variants, generated by the alanine scan, were tested *in vitro* for changes upon addition of 10 mM glucose.

FLIPglu (Figure 6.3, Table 6.3). Notably, the detection range of the MGlucoMeter2.6 sensors is substantially larger compared to FLIPglu, which covered less than two orders of magnitude (Table 6.3)(FLIPglu-600 μ: 65.4-5301 μM)[149]. Analysis of the substrate specificity showed that glucose had the highest affinity followed by galactose, whereas other sugars showed much lower affinities (Figure 6.4, Table 6.4). Of note, MGlucoMeter2.6-1m used below for *in planta* analyses, did not show detectable *in vitro* responses to the addition of sucrose (Figure 6.4).

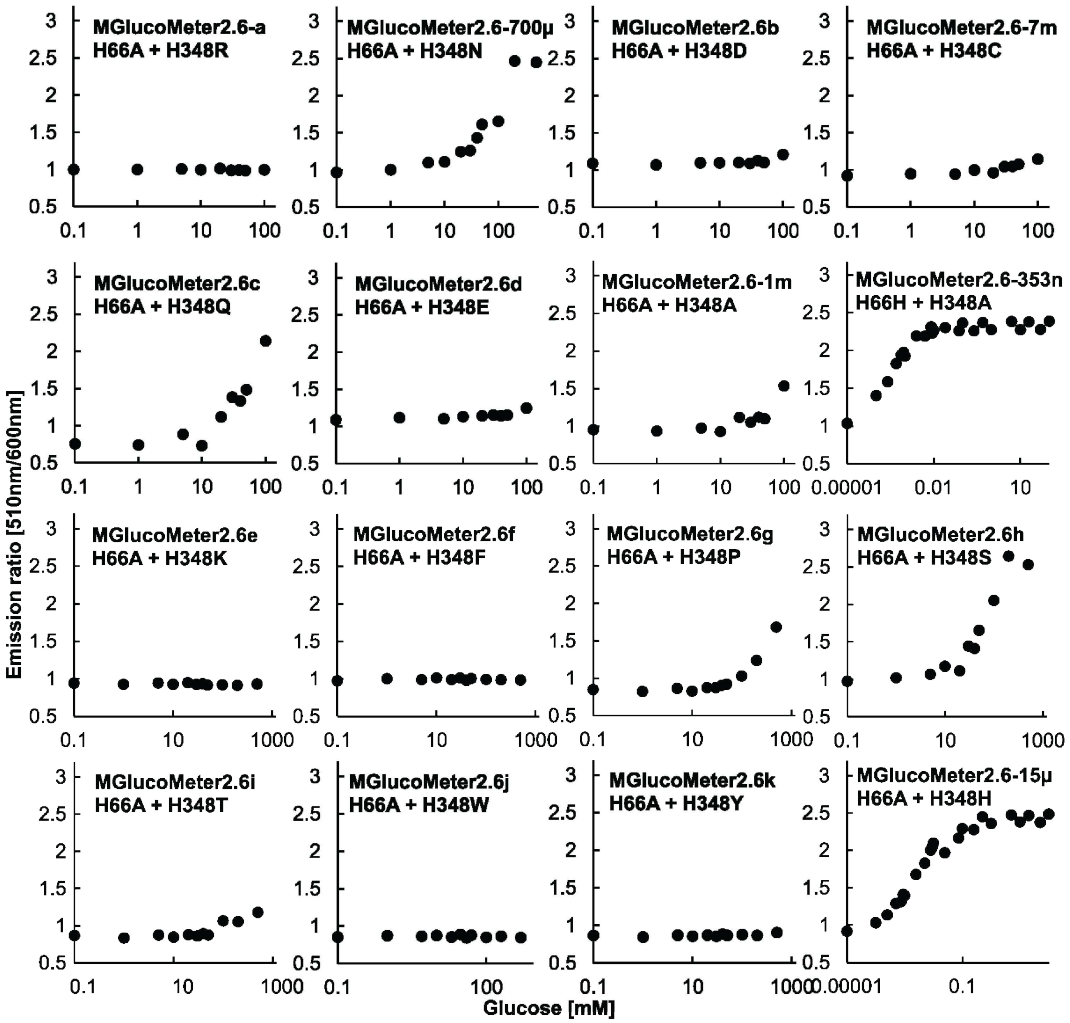

Figure 6.2: *In vitro* screening of affinity variants based on MGlucoMeter2.6. 16 affinity variants, generated by site directed mutagenesis at H66 and H348, were characterized *in vitro* using the cpsfGFP/LSSmApple emission ratio. Purified protein was titrated with increasing glucose concentrations.

Monitoring uptake of glucose into Arabidopsis roots

To be able to monitor glucose concentration changes *in planta*, MGlucoMeter2.6-1m was expressed from the UBQ10 promoter in the cytosol of the Arabidopsis

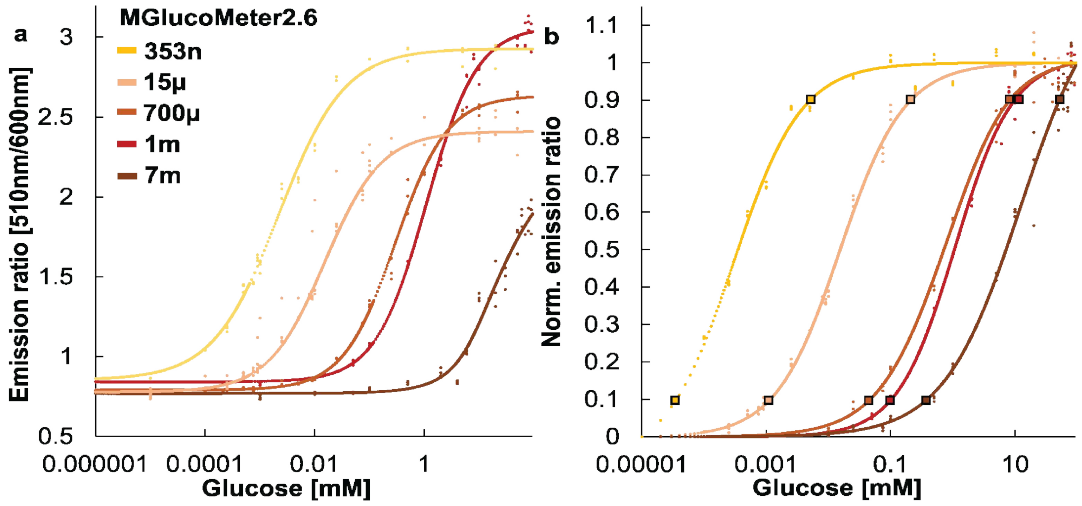

Figure 6.3: Glucose concentration dependent changes in fluorescence emission ratio of MGlucoMeter2.6 affinity variants. a. *In vitro* substrate titrations of MGlucoMeter2.6 affinity variants. MGlucoMeter2.6-353n (H66H + H348A), MGlucoMeter2.6-15 μ (H66A + H348H), MGlucoMeter2.6-700 μ (H66A + H348N), MGlucoMeter2.6-1m (H66A + H348A), and MGlucoMeter2.6-7m (H66A + H348C) were generated by site directed mutagenesis. The *in vitro* properties of each sensor are summarized in Table 6.2, Table 6.3. The mean of three technical replicates is plotted. Experiments were repeated independently two times with comparable results. **b.** Estimation of the detection range of MGlucoMeter2.6 (linear range between 10 and 90% saturation).

gene silencing mutant *rdr6*. Roots of 10-day-old seedlings mounted in a hand-made perfusion chamber were perfused with square pulses of glucose and the emission change after addition of glucose was monitored under an upright fluorescence microscope. Within one minute after addition of 1 mM glucose, MGlucoMeter2.6-1m showed a detectable emission ratio change in the root (Figure 6.5, Supplementary Video 1). Within about two minutes, the maximal response was reached, which would correspond to reaching the K_d of 1 mM, given that previous experiments with FRET glucose sensors had shown that extra- and intracellular levels of glucose rapidly equilibrated [154]. During further perfusion, the sensor response remained constant, and declined rapidly after replacing glucose-containing buffer with glucose-free buffer, consistent with reversibility of the response.

Detection of glucose accumulation by sucrose treatment to leaf

Sucrose generated by photosynthesis is loaded into the phloem of leaves and translocated from shoot to root. Sucrose utilization requires metabolic activities, e.g. invertases, that produce glucose and fructose. To investigate whether the MGlucoMeter2.6 can detect the production of glucose in roots that is derived from long distance

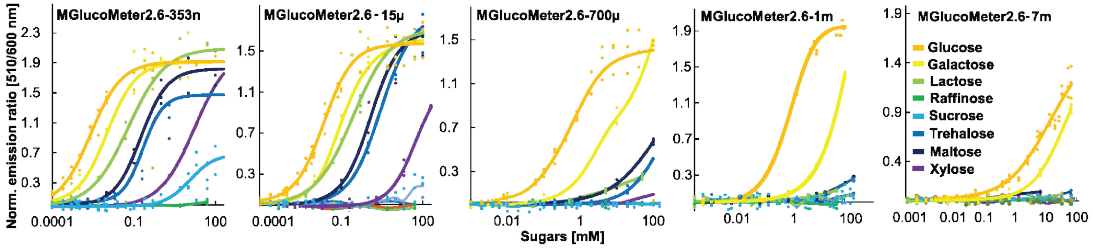

Figure 6.4: *In vitro* determination of the substrate selectivity of MGlucoMeter2.6 affinity variants. *In vitro* substrate titrations of MGlucoMeter2.6 affinity variants. MGlucoMeter2.6-353n, MGlucoMeter2.6-15μ, MGlucoMeter2.6-700μ, MGlucoMeter2.6-1m, MGlucoMeter2.6-7m were tested to determine the substrate selectivity. The *in vitro* properties of each sensor are summarized in Table 6.4. The mean of three technical replicates is plotted. Experiments were repeated independently two times with comparable results.

translocation of sucrose from the shoots, shoots of Arabidopsis plants expressing MGlucoMeter2.6-1m were exposed to media containing sucrose, and glucose accumulation was monitored in root tips (Figure 6.8). About 42 minutes after sucrose supply to the shoots, a ratio change was detected in roots, indicating that sucrose had been translocated from the shoot to the root tip unloading zone, where sucrose was then converted to glucose (Figure 6.6, Supplementary Video 2). As one may expect, we did not observe a change in glucose levels in the vasculature, consistent with delivery of sucrose from the shoot in the phloem, followed by unloading in the unloading zone in the root and hydrolysis and diffusion in the unloading zone. Of note, MGlucoMeter2.6-1m did not show detectable responses even to high sucrose concentrations (Figure 6.4). These observations are consistent with the important role of cytosolic invertases CINV1 and 2 for root growth and development [169]. In particular, CINV1 mRNA levels were high in cells in the unloading zone (Figure 6.9). Thus, detection of glucose accumulation by sucrose treatment to shoot confirmed that the sensitivity ($\Delta R/R_0$ 180 - 230%) of MGlucoMeter2.6-1m is high enough for effective and sensitive wide-view imaging to explore long-distance sugar translocation and metabolism in Arabidopsis.

Summary

In summary, we developed a new series of genetically encoded ultrasensitive ratiometric glucose sensors using the Matryoshka concept, in which excitation at a single wavelength enables detection of the emission for the sensory domain, a circular permutated superfolder GFP and the large Stokes shift reference fluorophore LSSmApple. The sensory domain was a periplasmic glucose binding protein from a

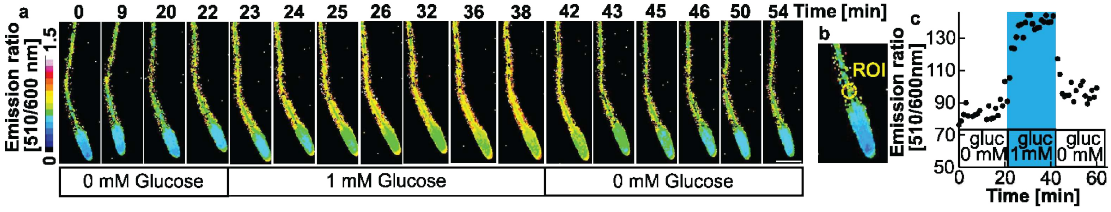

Figure 6.5: Time-dependent accumulation of glucose in Arabidopsis roots as monitored with MGlucoMeter2.6-1m to perfusion of roots with 1 mM glucose. **a.** Data from 10-day-old seedlings expressing MGlucoMeter2.6-1m (Supplementary Video 1). Maximum intensity Z-projection and the emission ratio of cpsfGFP over LSSmApple are shown. Experiments were repeated three times independently with comparable results. Scale bar: 200 μm. **b.** ROI used for quantification of the emission ratio in (Figure 6.5c) is shown as dotted yellow circle. **c.** Time-dependent *in vivo* response of MGlucoMeter2.6-1m in Arabidopsis roots. The cpsfGFP/ LSSmApple emission ratio was plotted. The blue square indicates square pulse of 1 mM glucose containing medium to MGlucoMeter2.6-1m expressing Arabidopsis seeding roots. The experiment was repeated with three biological replicates (individual roots) and three times independently with comparable results.

thermophile, which is likely more robust to insertion and mutagenesis. An alanine scan yielded sensors with a high sensitivity. We generated affinity mutants and used the optimized MGlucoMeter2.6 with an affinity for glucose of 1 mM to monitor glucose accumulation in intact Arabidopsis roots either from externally added glucose to roots or from hydrolysis of sucrose delivered from the shoot. Rapid hydrolysis of sucrose had previously been detected with a FRET glucose sensor [154]. Here we obtained evidence that sucrose is likely hydrolyzed after release from the phloem upon delivery from the shoot via the phloem. Cell-to-cell movement in the root is most likely mediated by plasmodesmata [154, 170, 171]. The new sensors can likely be deployed in a wide range of organisms, as previously shown for the FRET glucose sensors, including bacteria, yeast and human cell lines [149, 152, 157–159].

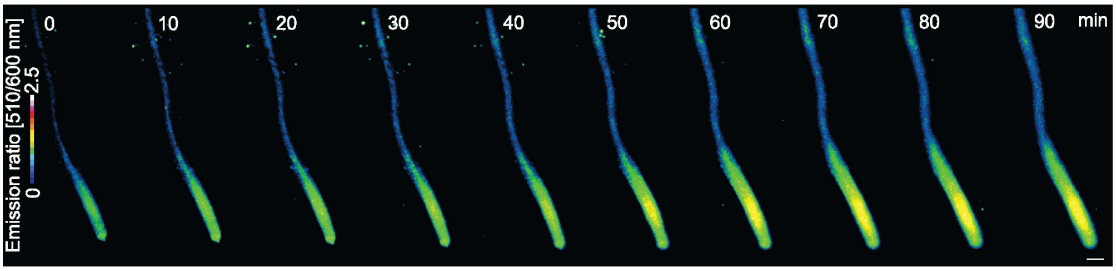

Figure 6.6: Detection of glucose accumulation in root tips of MGlucoMeter2.6-1m expressing Arabidopsis seedlings in response to sucrose application to the cotyledons. a. Data from 12-day-old seedlings expressing MGlucoMeter2.6-1m (Supplementary Video 2). Maximum intensity Z-projection and emission ratio of cpsfGFP over LSSmApple are shown. Scale bars: 200 μm. **b.** Time-dependent *in vivo* glucose accumulation in Arabidopsis roots after sucrose treatment to the cotyledons. Emission ratio of cpsfGFP over LSSmApple was plotted. The blue square indicates treatment with 2 M sucrose containing medium to MGlucoMeter2.6-1m expressing Arabidopsis cotyledons (Figure 6.8). ROI used for quantification of the emission ratio is shown as dotted red circle. The experiment was repeated with three biological replicates (individual roots) and three times independently with comparable results.

Main text tables

Table 6.1: Sequence of linker/hinge sequence subjected to alanine scanning of MGlucoMeter variants. Bold indicates sensor chosen for further studies. Italics indicates alanine mutation in linker region relative to MGlucoMeter1.0.

MGlucoMeter	$\Delta F/F_0$	Left linker	Right linker
MGlucoMeter1.0	0.50	DSDPSKYPASH	FNNPNAYGQSAM
MGlucoMeter2.0	0.84	DSDPSKYPASH	F*A*NPNAYGQSAM
MGlucoMeter2.1	0.24	DSDPSKYPASH	FNNPNA*A*GQSAM
MGlucoMeter2.2	0.85	DSDPSKYPA*A*H	FNNPNAYGQSAM
MGlucoMeter2.3	0.50	DSDPSKYPAS*A*	F*A*NPNAYGQSAM
MGlucoMeter2.4	0.36	DSDPSKYPA*A*H	*A*NNPNAYGQSAM
MGlucoMeter2.5	1.10	DSDPSKYPA*A*H	F*A*NPNAYGQSAM
MGlucoMeter2.6	**3.00**	**DSDPSKYPA*A*H**	**FNNP***A*AYGQSAM
MGlucoMeter2.7	0.45	DSDPSKY*A*ASH	*A*NNPNAYGQSAM
MGlucoMeter2.8	<0	DSDPSKYPASH	FN*A*PNAYGQSAM
MGlucoMeter2.9	<0	DSDPSK*A*PASH	FNNPNAYGQSAM
MGlucoMeter2.10	0.44	DSDPS*A*YPASH	FNNPNAYGQSAM
MGlucoMeter2.11	0.32	DSDPSKYPAS*A*	FN*A*PNAYGQSAM
MGlucoMeter2.12	0.13	DSDPSKYPAS*A*	FNN*A*NAYGQSAM
MGlucoMeter2.13	0.10	DSDPSKY*A*ASH	F*A*NPNAYGQSAM
MGlucoMeter2.14	< 0	DSDPSKY*A*ASH	FN*A*PNAYGQSAM

Sequence of linker/hinge sequence subjected to alanine scanning of MGlucoMeter variants — continued.

MGlucoMeter	$\Delta F/F_0$	Left linker	Right linker
MGlucoMeter2.15	0.59	DSDPSKY*A*ASH	FNN*A*NAYGQSAM
MGlucoMeter2.16	0.46	DSDPSKY*A*ASH	FNNP*A*AYGQSAM
MGlucoMeter2.17	0.03	DSDPSKYPA*A*H	FNNPNAYGQSA*A*
MGlucoMeter2.18	0.27	*A*SDPSKYPA*A*H	FNNP*A*AYGQSAM
MGlucoMeter2.19	0.95	D*A*DPSKYPA*A*H	FNNP*A*AYGQSAM
MGlucoMeter2.20	0.31	D*A*DPSKYPA*A*H	FNNPNAYGQSAM
MGlucoMeter2.21	1.39	DSD*A*SKYPASH	FNNP*A*AYGQSAM
MGlucoMeter2.22	1.00	DSDPSKYPA*A*H	FNNP*A*AYGQ*A*AM
MGlucoMeter2.23	0.61	DSDP*A*KYPASH	FNNP*A*AAGQSAM
MGlucoMeter2.24	0.10	DSDPSKYPASH	F*A*NP*A*AYGQSAM
MGlucoMeter2.25	0.68	DSDPSKYPA*A*H	FNNP*AA A*GQSAM
MGlucoMeter2.26	1.49	DSDPSKYPA*A*H	FNNP*A*AY*A*QSAM
MGlucoMeter2.27	0.50	DSDPSKYPA*A*H	FNNP*A*AYG*A*SAM
MGlucoMeter2.28	0.59	DSDPSKYPA*A*H	FNNP*A*AYGQSA*A*
MGlucoMeter2.29	1.74	DSD*A*SKYPA*A*H	FNNP*A*AYGQSAM
MGlucoMeter2.30	1.63	DSDP*A*KYPA*A*H	FNNP*A*AYGQSAM
MGlucoMeter2.31	1.05	DSDPSKYPASH	FNNP*A*AYGQSAM

Table 6.2: Affinity and mutation of MGlucoMeter2.6 variants. Bold indicates sensor chosen for further studies. n.r. indicates no response.

MGlucoMeter	Mutation	K_d glucose
MGlucoMeter2.6a	H66A + H348R	n.r.
MGlucoMeter2.6-700μ	**H66A + H348N**	$717 \pm 0.5\,\mu$M
MGlucoMeter2.6b	H66A + H348D	n.r.
MGlucoMeter2.6-7m	**H66A + H348C**	7.3 ± 0.5 mM
MGlucoMeter2.6c	H66A + H348Q	42.9 mM
MGlucoMeter2.6d	H66A + H348E	> 150 mM
MGlucoMeter2.6-1m	**H66A + H348A**	1.00 ± 0.01 mM
MGlucoMeter2.6-353n	**H66H + H348A**	355 ± 2.7 nM
MGlucoMeter2.6e	H66A + H348K	n.r.
MGlucoMeter2.6f	H66A + H348F	n.r.
MGlucoMeter2.6g	H66A + H348P	210.5 mM
MGlucoMeter2.6h	H66A + H348S	65.1 mM
MGlucoMeter2.6i	H66A + H348T	95.3 mM

Table 6.2: Affinity and mutation of MGlucoMeter2.6 variants.*(Continued)*

MGlucoMeter	**Mutation**	K_d **glucose**
MGlucoMeter2.6j	H66A + H348W	n.r.
MGlucoMeter2.6k	H66A + H348Y	n.r.
MGlucoMeter2.6-15μ	**H66A + H348H**	$15.0 \pm 0.46\,\mu$M

Table 6.3: Sensitivity and detection range of MGlucoMeter2.6 variants. MGlucoMeter2.6-1m sensor chosen for further studies.

MGlucoMeter	$\Delta F/F_0$	**Detection range (10–90% sat)**
MGlucoMeter2.6-353n	1.90 ± 0.06	$0.04\,\mu\text{M} - 5.1 \pm 0.1\,\mu$M
MGlucoMeter2.6-15μ	3.00 ± 0.13	$1.1 \pm 0.005\,\mu\text{M} - 216 \pm 14.4\,\mu$M
MGlucoMeter2.6-700μ	2.63 ± 0.18	$46.6 \pm 1.6\,\mu\text{M} - 8.6 \pm 1.0\,$mM
MGlucoMeter2.6-1m	3.69 ± 0.14	$102.7 \pm 0.003\,\mu\text{M} - 10.0 \pm 0.76\,$mM
MGlucoMeter2.6-7m	2.21 ± 0.19	$0.39 \pm 0.03\,\text{mM} - 55.9 \pm 11.4\,$mM

Table 6.4: Substrate selectivity of MGlucoMeter2.6 variants. 1 m sensor chosen for further studies. n.r. indicates no response.

K_d **Sugars**	**353n**	**15μ**	**700μ**	**1m**	**7m**
Glucose	$355 \pm 2.7\,$nM	$15 \pm 0.4\,\mu$M	$717 \pm 0.5\,\mu$M	$1.00 \pm 0.01\,$mM	$7.3 \pm 0.5\,$mM
Xylose	$1.83 \pm 0.6\,$mM	$25.6 \pm 2.3\,$mM	n.r.	n.r.	n.r.
Maltose	$62.3 \pm 0.07\,\mu$M	$0.97 \pm 0.02\,$mM	n.r.	n.r.	n.r.
Trehalose	$0.23 \pm 0.06\,$mM	$0.72 \pm 0.02\,$mM	n.r.	n.r.	n.r.
Sucrose	n.r.	n.r.	n.r.	n.r.	n.r.
Raffinose	n.r.	n.r.	n.r.	n.r.	n.r.
Lactose	$11 \pm 2.2\,\mu$M	n.r.	n.r.	n.r.	n.r.
Galactose	$2.8 \pm 0.3\,\mu$M	$38.2 \pm 4.5\,\mu$M	$2.87 \pm 0.2\,$mM	$14.9 \pm 0.7\,$mM	$25.5 \pm 2.2\,$mM

Supplementary

Protein sequence of the *Tt*GBP polypeptide from *Thermus thermophilus* used for sensor construction. The expressed gene product (P0328) lacks the 21 bp leader [165].

Leader 1-21: `MRKWLLAIGM VLGLSALAQG G`

Protein used for structure determination (pdb: 2B3B):

```
MKLEIFSWWA GDEGPALEAL IRLYKQKYPG VEVINATVTG GAGVNARAVL 50
KTRMLGGDPP DTFQVHAGME LIGTWVVANR MEDLSALFRQ EGWLQAFPKG 100
LIDLISYKGG IWSVPVNIHR SNVMWYLPAK LKEWGVNPPR TWDEFLATCQ 150
TLKQKGLEAP LALGEN WTQ QHLWESVALA VLGPDDWNNL WNGKLKFTDP 200
KAVRAWEVFG RVLDCANKDA AGLSWQQAVD RVVQGKAAFN VMGDWAAGYM 250
TTTLKLKPGT DFAWAPSPGT QGVFMMLSDS FGLPKGAKNR QNAINWLRLV 300
GSKEGQDTFN PLKGSIAARL DSDPSKYNAY GQSAMRDWRS NRIVGSLVHG 350
AVAPESFMSQ FGTVMEIFLQ TRNPQAAANA AQAIADQVGL GRLGQ
```

Numbering of residues based on protein P0328.

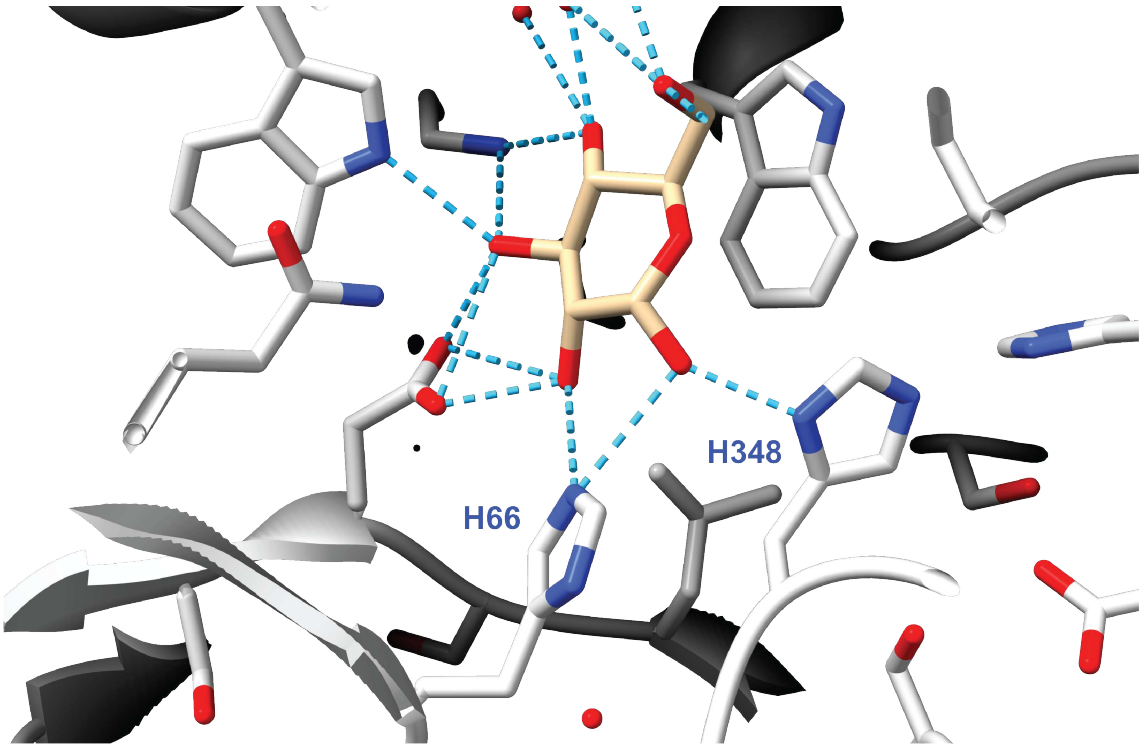

Figure 6.7: Hydrogen bond interactions of two histidines with glucose in *Tt*GBP (pdb 2B3B). Hydrogen bonds between *Tt*GBP and glucose are shown in turquoise. H66 and H348 are marked. The figure was generated using UCSF Chimera X (www.cgl.ucsf.edu/chimerax/).

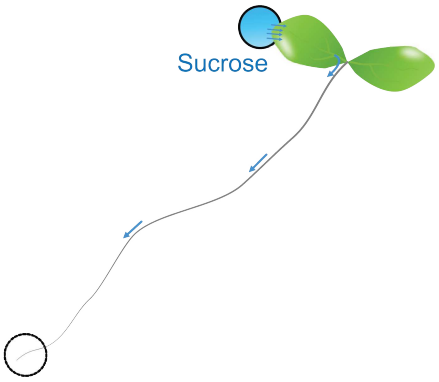

Figure 6.8: Experimental setup for observing glucose production in root tips. ROI used for quantification of the emission ratio in Figure 6.6 is shown as dotted black circle. The tip of leaf was exposed to 2M sucrose containing 1/2 salt strength MS and 2.35 mM MES (pH 5.7) buffer. Roots were placed on 1% agar plates containing ½ salt strength MS and 2.35 mM MES (pH 5.7).

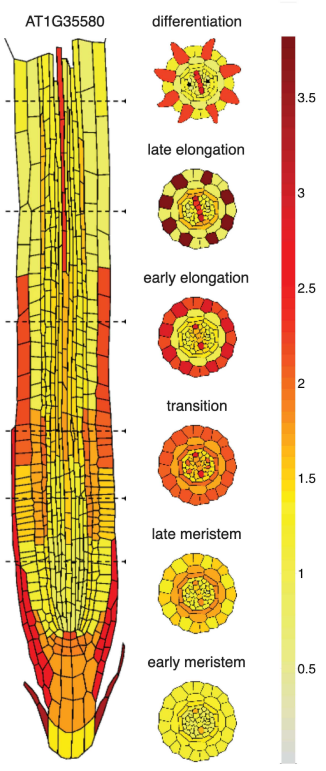

Figure 6.9: Levels of cytosolic invertase CINV1 mRNA in cell types in the root tip derived from single cell sequencing data. Image downloaded from the Root Cell Atlas (https://rootcellatlas.org/). Generated by Rahul Shaw, Maria Savina, Xin Tian, Zhichao An, Victoria Mironova, and Jian Xu.

Table 6.5: Partial list of primer names and their sequences.

Primer Name	Sequence (5'->3')
Ishi797 MGlucoMeter2.0 f	Gttatattccagtttatgccccaga
Ishi799 MGlucoMeter2.0 r	aaactggaatataactttGCTaatcctaatgcatatggtcaaag
Ishi871 MGlucoMeter2.1 f	GCAggtcaaagtgcgatgcgcgactggcg
Ishi872 MGlucoMeter2.1 r	gcatcgcactttgaccTGCtgcattaggattgttaaagttatattccag
Ishi808 MGlucoMeter2.2 f	gctagcagggtatttggatgg
Ishi810 MGlucoMeter2.2 r	tccAAAtaccctgctGCACATaacgtgtatattaccgcggataaacagaa
Ishi806 MGlucoMeter2.3 f2	cacgttTGCgctagcagggtatttggatggat
Ishi807 MGlucoMeter2.3 r2	gctagcGCAaacgtgtatattaccgcggataaacaga
Ishi798 MGlucoMeter2.4 r	aaactggaatataacGCTAACaatcctaatgcatatggtcaaag
Ishi804 MGlucoMeter2.6 f	tgcatatggtcaaagtgcgatgcgcg
Ishi805 MGlucoMeter2.6 r	ctttgaccatatgcAGCaggattgttaaagttatattccagt
Ishi798 MGlucoMeter2.7 r	gatccatccAAAtacGCAGCtAGCCATaacgtgtatattaccgcggata
Ishi800 MGlucoMeter2.8 f	gttaaagttatattc
Ishi801 MGlucoMeter2.8 r	gaatataactttaacGCTcctaatgcatatggtcaaagtgcga
Ishi865 MGlucoMeter2.9 f	GCAcctgctagccataacgt
Ishi867 MGlucoMeter2.9 r	gttatggctagcaggTGCtttggatggatcgctatcaagacgtg
Ishi868 MGlucoMeter2.10 r	gctagcagggtaTGCggatggatcgctatcaagacgtgcag
Ishi802 MGlucoMeter2.12 f	accatatgcattAGCattgttaaagttatattccagttta
Ishi803 MGlucoMeter2.12 r	GCTaatgcatatggtcaaagtgcgatgcgcgac
Ishi811 MGlucoMeter2.13 r	gatccatccAAAtacGCAGCtAGCCATaacgtgtatattaccgcggata
Ishi804 MGlucoMeter2.15 r	GCTaatgcatatggtcaaagtgcgatgcgcgac
Ishi805 MGlucoMeter2.16 r	ctttgaccatatgcAGCaggattgttaaagttatattccagt
Ishi879 MGlucoMeter2.17 f	GCAcgcgactggcgcagtaaccggattgtagg
Ishi880 MGlucoMeter2.17 r	gcgccagtcgcgTGCcgcactttgaccatatgcattaggattgttaaagttatat
Ishi881 MGlucoMeter2.18 f	GCAagcgatccatccaaataccc
Ishi882 MGlucoMeter2.18 r	ggatggatcgctTGCaagacgtgcagcaatagagcctttcagtg
Ishi883 MGlucoMeter2.19 f	GCAgatccatccaaataccctgct
Ishi884 MGlucoMeter2.19 r	tttggatggatcTGCatcaagacgtgcagcaatagagcctttca
Ishi887 MGlucoMeter2.21 f	GCAtccaaataccctgctagccata
Ishi888 MGlucoMeter2.21 r	agggtatttggaTGCatcgctatcaagacgtgcagca
Ishi894 MGlucoMeter2.22 f	Gcgatgcgcgactggcg
Ishi1125 MGlucoMeter2.22 r	ccagtcgcgcatcgcTGCttgaccatatgcTGCagga
Ishi957 MGlucoMeter2.23 f	GCAaaataccctgctGCAcataacgtgtatattaccgcgg
Ishi890 MGlucoMeter2.23 r	agcagggtatttTGCtggatcgctatcaagacgtgcagc
Ishi892 MGlucoMeter2.25 f	ggtcaaagtgcgatgcgcg
Ishi952 MGlucoMeter2.25 r	catcgcactttgacctgctgcTGCaggattgttaaagttatat

Table 6.5: Partial list of primer names and their sequences.*(Continued)*

Primer Name	Sequence (5'->3')
Ishi953 MGlucoMeter2.26 r	cgcactttgTGCATAtgcTGCaggattgttaaagttatattccagt
Ishi875 MGlucoMeter2.27 f	GCAagtgcgatgcgcgactggcgcagtaac
Ishi954 MGlucoMeter2.27 r	gcgcatcgcactTGCaccatatgcTGCaggattgttaaagttata
Ishi955 MGlucoMeter2.28 r	gcgccagtcgcgTGCcgcactttgaccatatgcTGCaggattgttaaagttatat
Ishi956 MGlucoMeter2.29 r	ccatccaaataccctgctGCAcataacgtgtatattacc
Ishi889 MGlucoMeter2.30 f	GCAtccaaataccctgctagccata
Ishi924 H66A f	tccataccggcCGCcacctgaaatgtgtccggaggatcaccgcc
Ishi1126 H66A r	tgGCGgccggtatggaactcattggcacttgggtagttgcgaa
Ishi900 A66H f	Atgccggtatggaactcattggcacttg
Ishi925 A66H r	Gttccataccggcatgcacctgaaatgtgtccggaggatcaccg
Ishi898 H348A f	gGCGggcgctgtcgctccggaaagtttcatg
Ishi899 H348A r	gcgacagcgccCGCcactaagctgcctacaatccggttactg
Ishi1127 A348H f	gCATggcgctgtcgctccggaaagtttcatg
Ishi1128 A348H r	gcgacagcgccATGcactaagctgcctacaatccggttactg
Ishi1129 Inv f	Ggcgctgtcgctccggaaagtttcatg
Ishi1130 MGlucoMeter2.6a r	CGGAgcgacagcgccACGcactaagctgcctacaatccggttactg
Ishi1131 MGlucoMeter2.6-700μ r	CGGAgcgacagcgccATTcactaagctgcctacaatccggttactg
Ishi1132 MGlucoMeter2.6b r	CGGAgcgacagcgccATCcactaagctgcctacaatccggttactg
Ishi1133 MGlucoMeter2.6-7m r	CGGAgcgacagcgccACAcactaagctgcctacaatccggttactg
Ishi1134 MGlucoMeter2.6c r	CGGAgcgacagcgccTTGcactaagctgcctacaatccggttactg
Ishi1135 MGlucoMeter2.6d r	CGGAgcgacagcgccTTCcactaagctgcctacaatccggttactg
Ishi1139 MGlucoMeter2.6e r	CGGAgcgacagcgccCTTcactaagctgcctacaatccggttactg
Ishi1140 MGlucoMeter2.6f r	CGGAgcgacagcgccAAAcactaagctgcctacaatccggttactg
Ishi1141 MGlucoMeter2.6g r	CGGAgcgacagcgccAGGcactaagctgcctacaatccggttactg
Ishi1142 MGlucoMeter2.6h r	CGGAgcgacagcgccACTcactaagctgcctacaatccggttactg
Ishi1143 MGlucoMeter2.6i r	CGGAgcgacagcgccAGTcactaagctgcctacaatccggttactg
Ishi1144 MGlucoMeter2.6j r	CGGAgcgacagcgccCCAcactaagctgcctacaatccggttactg
Ishi1145 MGlucoMeter2.6k r	CGGAgcgacagcgccATAcactaagctgcctacaatccggttactg

Supplemental videos

Supplemental videos will be available with the publication of the manuscript.

Acknowledgements

This work is part of the collaboration research center CRC1535 funded by grants to WF from Deutsche Forschungsgemeinschaft (DFG, German Research Foundation) - Project 458090666/CRC1535/1 and Germany´s Excellence Strategy – EXC-2048/1 – project ID 390686111 (CEPLAS), and an Alexander von Humboldt Professorship.

CHAPTER 7

Ratiometric Matryoshka MSucMeter sensors for sucrose[7]

7: This chapter is based on the article *Ratiometric Matryoshka MSucMeter sensors for sucrose* by Athanasios Papadopoulos, Jens Reiners, **Nora R. Zöllner**, Laura Redzich, Mayuri Sadoine, Christoph G. W. Gertzen, Tom Berwanger, Kerstin Schipper, Manuel Anlauf, Stefanie Weidtkamp-Peters, Wolf B. Frommer, and Sander H. J. Smits, which is currently in preparation. This dissertation presents only a summary of the study.

I contributed approximately 15 % to this project, primarily through the design, execution, and analysis of *in vitro* biochemical experiments, as well as by providing substantial conceptual guidance on biosensors that informed experimental design and methodology throughout the study.

7.1 Summary

The accurate detection of metabolite fluctuations in living cells remains a challenge in cell biology. Sugars such as sucrose are central to plant and microbial metabolism, acting both as energy sources and signaling molecules. Monitoring their levels with spatial and temporal resolution is essential for understanding metabolic pathways and regulatory networks. Genetically encoded fluorescent biosensors have emerged as powerful non-invasive tool for real-time metabolite detection. However, their development is a laborious and time consuming.

Until recently, the detection of sucrose *in vivo* relied exclusively on Förster resonance energy transfer (FRET)–based biosensors. These systems enable metabolite tracking but are constrained by a low signal-to-noise ratio, restricted sensitivity, and a narrow dynamic range. Such constraints hamper quantitative analyses in conditions where sucrose concentrations vary broadly. To overcome these limitations, a novel ratiometric biosensor, MSucMeter, was designed based on Matryoshka architecture. This Matryoshka-based biosensor incorporates a large stokes shift (LSS) reference fluorophore and a circularly permuted reporter fluorophore into a single genetic cassette, enabling single-wavelength excitation with dual-fluorescence emission (Figure 7.1). The approach allows normalization of reporter signal changes against the stable reference signal, thereby improving measurement accuracy under varying imaging conditions.

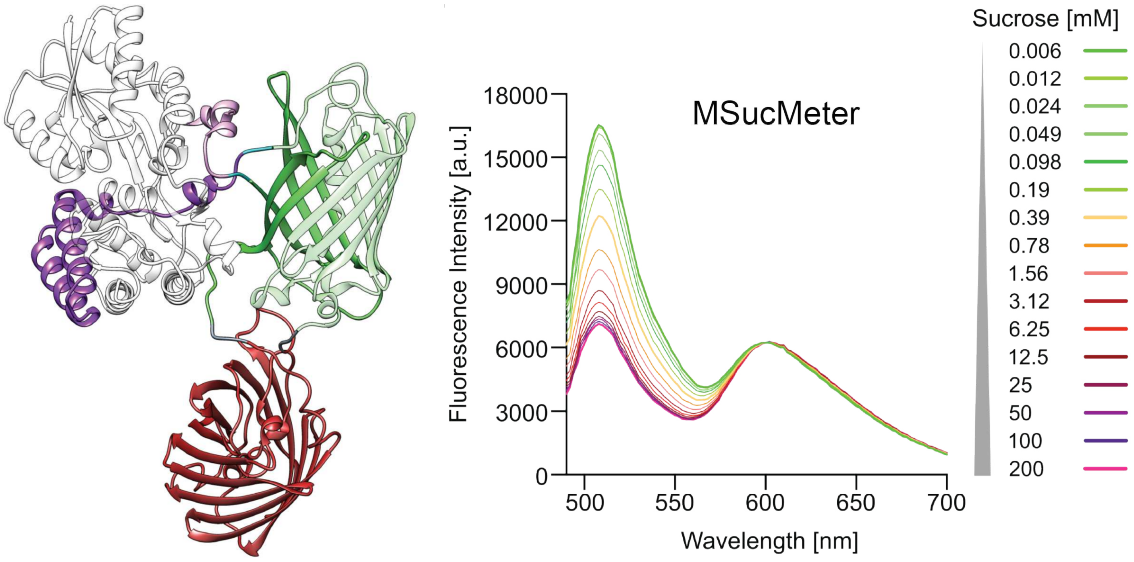

Figure 7.1: Newly developed MSucMeter. AlphaFold2-modeled structure of the biosensor with reporter fluorophore cpsfGFP (green), reference fluorophore LSSmApple (red) and sucrose binding domain (purple); and spectral *in vitro* characterization.

In the MSucMeter, the Matryoshka cassette was inserted into the highly sucrose-specific protein *At*ThuE from *Agrobacterium tumefaciens*. Multiple affinity mutants were generated and biochemically characterized, revealing binding affinities within physiologically relevant ranges from 400 μM to 4.4 mM. Structural analysis by small-angle X-ray scattering (SAXS) provided a three-dimensional model of the biosensor, defining the relative orientation of domains and confirming the absence of oligomerization. Monomers are especially important to maintain free binding sites and enable consistent sensor performance.

The sensing mechanism of MSucMeter is characterized by a negative ratiometric response: increasing sucrose concentrations quench the fluorescence intensity of the reporter fluorophore cpsfGFP, while the reference fluorophore, LSSmApple, remains constant. This inverse correlation enables robust quantitative measurements through ratiometric analysis. *In vitro* studies confirmed the biochemical stability of the biosensor, while *in vivo* assays demonstrated its functionality in both bacterial and plant systems. Expression in bacteria allowed proof-of-principle validation via unspecific sucrose uptake, whereas plant-based experiments confirmed the sensor's applicability for monitoring sucrose uptake in a physiologically relevant context.

In conclusion, the newly developed MSucMeter represents a substantial advancement in metabolite biosensing technology. By combining the high specificity of the ThuE protein with the precision and stability of the Matryoshka approach, this ratiometric sensor overcomes major limitations of FRET-based biosensors. Its ability to provide direct, quantitative, and real-time readouts of sucrose dynamics both *in vitro* and *in vivo* opens new possibilities for research of sugar transport, allocation, and signaling in plants and microbes.

CHAPTER 8

Outlook

Conclusions

While genome editing of clade III *SWEET* genes has provided an effective resistance strategy, the evolutionary adaptability of *Xoo* raises the likelihood that such an resistance will eventually be overcome. A deeper understanding of the infection process is therefore essential to identify additional targets for durable resistance.

This dissertation establishes that *Xoo* relies on a dedicated sucrose uptake system, the *sux* cluster, to couple host sucrose efflux with pathogen metabolism (Chapters 2 and 5), and reveals a potential dual localization of the sucrose hydrolase SuxB (Chapter 3). Furthermore, the work introduces three approaches to address the long-standing question of how *Xoo* colonizes the xylem against the bulk sap stream (Chapter 4). Beyond these biological insights, I developed ultrasensitive ratiometric biosensors for sucrose and glucose in collaboration with Papadopulos et al. and Ishikawa et al. (Chapters 6–7), creating tools that enable direct visualization of sugar fluxes *in vivo* with unprecedented precision. Together, these findings deepen our understanding of the metabolic basis of Bacterial Blight and provide the field with novel methodologies to dissect host–pathogen sugar dynamics.

Although the work described in this dissertation represents significant progress toward our understanding of the infection process caused by *Xoo*, these results also point to new questions. First, the origin of sucrose accessed through the *sux* cluster, described in Zoellner et al., 2025, remains unclear and requires joint analysis of host efflux and bacterial uptake (I). Second, the proposed dual localization of SuxB is currently based on mainly descriptive evidence; it remains to be determined whether the two isoforms are relevant *in vivo* for the infection (II). How is the dual localization regulated, and what roles do the isoforms play during infection (II). Lastly, what is the origin of residual virulence observed in SuxA mutants (III).

(I) Strategies to connect *SWEET*-mediated sucrose release with *sux*-driven sucrose uptake

A major limitation of this study was the absence of a direct link between the host sucrose efflux and pathogen uptake. Although *sux*-deletion mutants were avirulent, the loss of virulence might reflect indirect effects of impaired EPS production, biofilm formation, or reduced motility rather than a primary feeding defect. The critical unresolved question is therefore whether *sux*-mediated sucrose uptake is functionally linked to *SWEET*-mediated sucrose release during infection.
To address this gap, I performed a host-pathogen RNA sequencing (dualRNAseq),

which allows simultaneous analysis of host and pathogen transcriptomes. Preliminary results were obtained while writing this dissertation. These preliminary results indicate a parallel increase of *SWEET* and *sux* transcripts, indicating that bacterial sucrose uptake is temporally coordinated with host sucrose efflux. Further analysis of the dualRNAseq dataset is necessary to confirm this transcriptional coupling. Additionally, applying the newly developed ratiometric biosensors for sucrose and glucose will allow to measure sugar fluxes in the pathosystem and determine biochemical rates of transporters and enzymes. Potentially, biosensors could reveal whether host sucrose release quantitatively matches the pathogen uptake. Initial applications should focus on simplified experimental systems to reduce experimental complexity, before moving to intact host–pathogen interactions. Together, the dualRNA-seq and biosensor approaches will establish a crucial link between host carbon export and pathogen acquisition.

(II) Implications of potential dual-localized sucrose hydrolase and strategies for experimental validation

This work provides initial, descriptive evidence for two SuxB isoforms. A predicted signal peptide for secretion supports the hypothesis of dual localization. However, the functional relevance of these isoforms during infection remains unknown. The activity of the secreted SuxB under nutrient-limited conditions indicates a potential role in infection, where extracellular hydrolysis could enhance sucrose uptake during colony lifestyle.

Identifying the implication of each isoform will require further research. A crucial next step is generating mutants that produce an exclusively secreted or non-secreted SuxB and perform infection assays. Further, these mutants should be used for biochemical characterization to enable exploration of three non-exclusive scenarios: Dual localization allows (i) parallel uptake to increase total sucrose acquisition; (ii) specialization in distinct biochemical niches; and (iii) secretion of SuxB as a "public good" supporting neighboring bacterial cells. Understanding the molecular basis of dual localization is equally critical. Potential mechanisms could include alternative translation initiation through attenuation-like regulation.

Together, these complementary approaches will determine whether dual localization is genuine, how it is regulated, and how it contributes to virulence. Lastly, isoform-specific mutants will enable the metabolic modeling of public good dynamics in bacterial interactions.

(III) Identification of origin for residual virulence

The *suxA* mutants of *Xoo* lack the outer membrane transporter of the *sux* cluster, but still exhibit residual virulence. Similarly, deleting the *sux* cluster in *Xanthomonas axonopodis pv. glycines* and *Xanthomonas axonopodis pv. manihotis* caused only moderate or no delay in disease development [39, 84]. Understanding the origin of this residual virulence is critical for identifying alternative targets for resistance engineering, particularly when SWEET-dependent resistance is overcome.
Several mechanisms may contribute to residual virulence. First, alternative carbon sources, such as glucose and fructose, as well as host cell wall-derived oligosaccharides, may partially compensate for the loss of *sux*-mediated sucrose uptake. Second, redundant bacterial transport systems, such as porins, hexose transporters, PTS systems, and ABC transporters, may enable the pathogen to acquire these sugars. Third, metabolic flexibility may enable the pathogen to utilize organic acids or amino acids present in the xylem sap.
To address these hypotheses, the dualRNAseq dataset will be examined for hexose or alternative carbon transporters that are differentially regulated during infections and can import hydrolysis products from secreted SuxB or other sucrolytic enzymes. The identified candidates will be systematically mutated in combination with *suxA* mutants, and their virulence will be assessed *in vivo*. Complementary approaches, including metabolomic profiling of xylem sap and *in vivo* sugar flux measurements, will help quantify the residual carbon sources available to the pathogen. Together, these strategies will reveal the metabolic pathways underlying residual virulence and inform resistance strategies targeting the pathogen's multiple carbon acquisition routes.

Despite the identification of Bacterial Blight in the 19th century and extensive studies since then, the infection process remains only partially understood. In this thesis, I made a significant contribution to our understanding of the role of sugars in plant–pathogen interactions and providing highly sensitive tools for quantitative sugar flux analyses.

Using diverse transcriptomic approaches, I provided a more detailed molecular understanding of how TALe-mediated induction of clade III *SWEETs* and sucrose uptake via the *sux* cluster establish sucrose as one key factor for *Xoo* virulence. Biochemically, I characterized a unique sucrose hydrolase and determined kinetic constants. Applying crystallographic techniques, I confirmed an exclusive sucrose hydrolysis function of SuxB. Further analysis, revealed characteristics of potential dual localization with so far undetermined function.

Because TALe-mediated induction of *SWEETs* is a conserved virulence strategy across diverse *Xanthomonas* pathovars and crops, the insights of this thesis are likely to extend beyond Bacterial Blight and may inform resistance breeding strategies across multiple pathosystems. Such strategies will be essential for achieving durable and sustainable resistance of rice and other crops against vascular pathogens, and the concepts developed here may inform broader studies of carbon allocation during plant–microbe interactions.

Bibliography

[1] Wolinsky, H. The mystery of an unprecedented plant disease in Africa. *EMBO Rep.* **2023**. *24*, DOI: 10.15252/embr.202357596.

[2] Loo, E. P. I.; Huguet-Tapia, J.; Selvaraj, M.; Stiebner, M.; Killing, B.; Buchholzer, M.; Schepler-Luu, V.; Hartwig, T.; Gutierrez, S. V.; Rast-Somssich, M. I.; Szurek, B.; Tohme, J.; Charraviaga, P.; White, F. F.; Yang, B.; Frommer, W. B. From lab to field: analyses of genome-edited bacterial blight resistant rice. 2025. DOI: 10.1101/2025.05.26.656110.

[3] Ou, S. H. *Rice diseases*; IRRI: 1985.

[4] Niño-Liu, D. O.; Ronald, P. C.; Bogdanove, A. J. *Xanthomonas oryzae* pathovars: model pathogens of a model crop. *Mol. Plant Pathol.* **2006**. *7*, 303–324. DOI: 10.1111/j.1364-3703.2006.00344.x.

[5] Hilaire, E.; Young, S. A.; Willard, L. H.; McGee, J. D.; Sweat, T.; Chittoor, J. M.; Guikema, J. A.; Leach, J. E. Vascular defense responses in rice: Peroxidase accumulation in xylem parenchyma cells and xylem wall thickening. *Mol. Plant-Microbe Interact.* **2001**. *14*, 1411–1419. DOI: 10.1094/MPMI.2001.14.12.1411.

[6] Ranjani, P.; Palani, P. Isolation and molecular typing of *Xanthomonas oryzae pv. oryzae* isolates from hotspots in southern states of india. *Plant Dis. Rep.* **2020**. *35*, 161–172. DOI: 10.5958/2249-8788.2020.00033.5.

[7] Chatterjee, S.; Samal, B.; Singh, P.; Pradhan, B. B.; Verma, R. K. Transition of a solitary to a biofilm community life style in bacteria: a survival strategy with division of labour. *Int. J. Dev. Biol.* **2020**. *64*, 259–265. DOI: 10.1387/ijdb.190176sc.

[8] Ham, Y.; Kim, T.-J. Nitrogen sources inhibit biofilm formation of *Xanthomonas oryzae pv. oryzae*. *J. Microbiol. Biotechnol.* **2018**. *28*, 2071–2078. DOI: 10.4014/jmb.1808.08025.

[9] Grau, J.; Reschke, M.; Erkes, A.; Streubel, J.; Morgan, R. D.; Wilson, G. G.; Koebnik, R.; Boch, J. AnnoTALE: bioinformatics tools for identification, annotation and nomenclature of TALEs from *Xanthomonas* genomic sequences. *Sci. Rep.* **2016**. *6*, 21077. DOI: 10.1038/srep21077.

[10] Yang, B.; Sugio, A.; White, F. F. *Os8N3* is a host disease-susceptibility gene for bacterial blight of rice. *Proc. Natl. Acad. Sci. U.S.A.* **2006**. *103*, 10503–10508. DOI: 10.1073/pnas.0604088103.

[11] Chen, L.-Q. SWEET sugar transporters for phloem transport and pathogen nutrition. *New Phytol.* **2014**. *201*, 1150–1155. DOI: 10.1111/nph.12445.

[12] Chen, L.-Q.; Hou, B.-H.; Lalonde, S.; Takanaga, H.; Hartung, M. L.; Qu, X.-Q.; Guo, W.-J.; Kim, J.-G.; Underwood, W.; Chaudhuri, B.; Chermak, D.; Antony, G.; White, F. F.; Somerville, S. C.; Mudgett, M. B.; Frommer, W. B. Sugar transporters for intercellular exchange and nutrition of pathogens. *Nature* **2010**. *468*, 527–532. DOI: 10.1038/nature09606.

[13] Bezrutczyk, M.; Yang, J.; Eom, J.-S.; Prior, M.; Sosso, D.; Hartwig, T.; Szurek, B.; Oliva, R.; Vera-Cruz, C.; White, F. F.; Yang, B.; Frommer, W. B. Sugar flux and signaling in plant–microbe interactions. *Plant J.* **2018**. *93*, 675–685. DOI: 10.1111/tpj.13775.

[14] Buchanan, B. B.; Gruissem, W.; Jones, R. L.; Vickers, K. *Biochemistry and molecular biology of plants*; John Wiley & Sons: 2015.

[15] Lalonde, S.; Wipf, D.; Frommer, W. B. Transport mechanisms for organic forms of carbon and nitrogen between source and sink. *Annu Rev Plant Biol* **2004**. *55*, 341–372. DOI: 10.1146/annurev.arplant.55.031903.141758.

[16] Naseem, M.; Kunz, M.; Dandekar, T. Plant–pathogen maneuvering over apoplastic sugars. *Trends Plant Sci.* **2017**. *22*, 740–743. DOI: 10.1016/j.tplants.2017.07.001.

[17] Liu, Y.-H.; Song, Y.-H.; Ruan, Y.-L. Sugar conundrum in plant–pathogen interactions: roles of invertase and sugar transporters depend on pathosystems. *J. Exp. Bot.* **2022**. *73*, 1910–1925. DOI: 10.1093/jxb/erab562.

[18] Yamada, K.; Saijo, Y.; Nakagami, H.; Takano, Y. Regulation of sugar transporter activity for antibacterial defense in Arabidopsis. *Science* **2016**. *354*, 1427–1430. DOI: 10.1126/science.aah5692.

[19] Sosso, D.; van der Linde, K.; Bezrutczyk, M.; Schuler, D.; Schneider, K.; Kämper, J.; Walbot, V. Sugar partitioning between *Ustilago maydis* and its host *Zea mays* during infection. *Plant Physiol.* **2019**. *179*, 1373–1385. DOI: 10.1104/pp.18.01435.

[20] Fotopoulos, V.; Gilbert, M. J.; Pittman, J. K.; Marvier, A. C.; Buchanan, A. J.; Sauer, N.; Hall, J.; Williams, L. E. The monosaccharide transporter gene, *AtSTP4*, and the cell-wall invertase, *Atβfruct1*, are induced in Arabidopsis during infection with the fungal biotroph *Erysiphe cichoracearum*. *Plant Physiol.* **2003**. *132*, 821–829. DOI: 10.1104/pp.103.021428.

[21] Lemonnier, P.; Gaillard, C.; Veillet, F.; Verbeke, J.; Lemoine, R.; Coutos-Thévenot, P.; La Camera, S. Expression of Arabidopsis sugar transport protein STP13 differentially affects glucose transport activity and basal resistance to *Botrytis cinerea*. *Plant Mol. Biol.* **2014**. *85*, 473–484. DOI: 10.1007/s11103-014-0198-5.

[22] Gómez-Ariza, J.; Campo, S.; Rufat, M.; Estopà, M.; Messeguer, J.; Segundo, B. S.; Coca, M. Sucrose-mediated priming of plant defense responses and broad-spectrum disease resistance by overexpression of the Maize pathogenesis-related PRms protein in Rice plants. *Mol. Plant-Microbe Interact.* **2007**. *20*, 832–842. DOI: 10.1094/MPMI-20-7-0832.

[23] Gebauer, P.; Korn, M.; Engelsdorf, T.; Sonnewald, U.; Koch, C.; Voll, L. M. Sugar accumulation in leaves of Arabidopsis *sweet11/sweet12* double mutants enhances priming of the salicylic acid-mediated defense response. *Front. Plant Sci.* **2017**. *8*, DOI: 10.3389/fpls.2017.01378.

[24] Büttner, D.; Bonas, U. Regulation and secretion of *Xanthomonas* virulence factors. *FEMS Microbiol. Rev.* **2010**. *34*, 107–133. DOI: 10.1111/j.1574-6976.2009.00192.x.

[25] Parrent, J. L.; James, T. Y.; Vasaitis, R.; Taylor, A. F. Friend or foe? Evolutionary history of glycoside hydrolase family 32 genes encoding for sucrolytic activity in fungi and its implications for plant-fungal symbioses. *BMC Evol. Biol.* **2009**. *9*, 148. DOI: 10.1186/1471-2148-9-148.

[26] Talbot, N. J. Living the SWEET life: How does a plant pathogenic fungus acquire sugar from plants? *PLoS Biology* **2010**. *8*, DOI: 10.1371/journal.pbio.1000308.

[27] Kay, S.; Bonas, U. How *Xanthomonas* type III effectors manipulate the host plant. *Curr. Opin. Microbiol.* **2009**. *12*, 37–43. DOI: 10.1016/j.mib.2008.12.006.

[28] Cantu, D.; Govindarajulu, M.; Kozik, A.; Wang, M.; Chen, X.; Kojima, K. K.; Jurka, J.; Michelmore, R. W.; Dubcovsky, J. Next generation sequencing provides rapid access to the genome of *Puccinia striiformis f. sp. tritici*, the causal agent of wheat stripe rust. *PLoS ONE* **2011**. *6*, DOI: 10.1371/journal.pone.0024230.

[29] Zheng, W.; Huang, L.; Huang, J.; Wang, X.; Chen, X.; Zhao, J.; Guo, J.; Zhuang, H.; Qiu, C.; Liu, J.; Liu, H.; Huang, X.; Pei, G.; Zhan, G.; Tang, C.; Cheng, Y.; Liu, M.; Zhang, J.; Zhao, Z.; Zhang, S.; Han, Q.; Han, D.; Zhang, H.; Zhao, J.; Gao, X.; Wang, J.; Ni, P.; Dong, W.; Yang, L.; Yang, H.; Xu, J.-R.; Zhang, G.; Kang, Z. High genome heterozygosity and endemic genetic recombination in the wheat stripe rust fungus. *Nat. Commun.* **2013**. *4*, 2673. DOI: 10.1038/ncomms3673.

[30] Aparna, G.; Chatterjee, A.; Sonti, R. V.; Sankaranarayanan, R. A cell wall–degrading esterase of *Xanthomonas oryzae* requires a unique substrate recognition module for pathogenesis on rice. *Plant Cell* **2009**. *21*, 1860–1873. DOI: 10.1105/tpc.109.066886.

[31] Wittek, A.; Dreyer, I.; Al-Rasheid, K. A. S.; Sauer, N.; Hedrich, R.; Geiger, D. The fungal UmSrt1 and maize ZmSUT1 sucrose transporters battle for plant sugar resources. *J. Integr. Plant Biol.* **2017**. *59*, 422–435. DOI: 10.1111/jipb.12535.

[32] Eom, J.-S.; Chen, L.-Q.; Sosso, D.; Julius, B. T.; Lin, I.; Qu, X.-Q.; Braun, D. M.; Frommer, W. B. SWEETs, transporters for intracellular and intercellular sugar translocation. *Curr. Opin. Plant Biol.* **2015**. *25*, 53–62. DOI: 10.1016/j.pbi.2015.04.005.

[33] Streubel, J.; Pesce, C.; Hutin, M.; Koebnik, R.; Boch, J.; Szurek, B. Five phylogenetically close rice *SWEET* genes confer TAL effector-mediated susceptibility to *Xanthomonas oryzae* pv. *oryzae*. *New Phytol.* **2013**. *200*, 808–819. DOI: 10.1111/nph.12411.

[34] Liu, Q.; Yuan, M.; Zhou, Y.; Li, X.; Xiao, J.; Wang, S. A paralog of the MtN3/saliva family recessively confers race-specific resistance to *Xanthomonas oryzae* in rice. *Plant, Cell & Environment* **2011**. *34*, 1958–1969. DOI: 10.1111/j.1365-3040.2011.02391.x.

[35] Antony, G.; Zhou, J.; Huang, S.; Li, T.; Liu, B.; White, F.; Yang, B. Rice xa13 recessive resistance to bacterial blight is defeated by induction of the disease dusceptibility gene *Os-11N3*. *Plant Cell* **2010**. *22*, 3864–3876. DOI: 10.1105/tpc.110.078964.

[36] Chong, J.; Piron, M.-C.; Meyer, S.; Merdinoglu, D.; Bertsch, C.; Mestre, P. The SWEET family of sugar transporters in grapevine: *Vv*SWEET4 is involved in the interaction with *Botrytis cinerea*. *J. Exp. Bot.* **2014**. *65*, 6589–6601. DOI: 10.1093/jxb/eru375.

[37] Tsuge, S.; Nishida, M.; Furutani, A.; Kubo, Y.; Horino, O. Growth of glucose-uptake-deficient mutant of *Xanthomonas oryzae pv. oryzae* in Rice leaves. *J. Gen. Plant Pathol.* **2001**. *67*, 144–147. DOI: 10.1007/PL00013000.

[38] Bogs, J.; Geider, K. Molecular analysis of sucrose metabolism of *Erwinia amylovora* and influence on bacterial virulence. *J. Bacteriol.* **2000**. *182*, 5351–5358. DOI: 10.1128/jb.182.19.5351-5358.2000.

[39] Kim, H.-S.; Park, H.-J.; Heu, S.; Jung, J. Molecular and functional characterization of a unique sucrose hydrolase from *Xanthomonas axonopodis pv. glycines*. *J. Bacteriol.* **2004**. *186*, 411–418. DOI: 10.1128/JB.186.2.411-418.2004.

[40] Blanvillain, S.; Meyer, D.; Boulanger, A.; Lautier, M.; Guynet, C.; Denancé, N.; Vasse, J.; Lauber, E.; Arlat, M. Plant carbohydrate scavenging through TonB-dependent receptors: A feature shared by phytopathogenic and aquatic bacteria. *PLoS ONE* **2007**. *2*, DOI: 10.1371/journal.pone.0000224.

[41] Zoellner, N. R.; Long, J. Y.; Song, C.; Sharkey, J.; Wudick, M. M.; Loo, E. P.; Sadoine, M.; Applegate, V.; Port, A.; Smits, S.; Yang, B.; Frommer, W. B. A critical role of *sux* cistron-mediated sucrose uptake for virulence of the rice blight pathogen *Xanthomonas oryzae pv. oryzae*. 2025. DOI: 10.1101/2025.06.02.657373.

[42] Bae, C.; Han, S. W.; Song, Y.-R.; Kim, B.-Y.; Lee, H.-J.; Lee, J.-M.; Yeam, I.; Heu, S.; Oh, C.-S. Infection processes of xylem-colonizing pathogenic bacteria: possible explanations for the scarcity of qualitative disease resistance genes against them in crops. *Theor. Appl. Genet.* **2015**. *128*, 1219–1229. DOI: 10.1007/s00122-015-2521-1.

[43] Lowe-Power, T. M.; Khokhani, D.; Allen, C. How *Ralstonia solanacearum* exploits and thrives in the flowing plant xylem environment. *Trends Microbiol.* **2018**. *26*, 929–942. DOI: 10.1016/j.tim.2018.06.002.

[44] McCully, M. E. Niches for bacterial endophytes in crop plants: a plant biologist's view. *Funct. Plant Biol.* **2001**. *28*, 983–990. DOI: 10.1071/pp01101.

[45] Peuke, A. D.; Rokitta, M.; Zimmermann, U.; Schreiber, L.; Haase, A. Simultaneous measurement of water flow velocity and solute transport in xylem and phloem of adult plants of *Ricinus communis* over a daily time course by nuclear magnetic resonance spectrometry. *Plant Cell Environ.* **2001**. *24*, 491–503. DOI: 10.1046/j.1365-3040.2001.00704.x.

[46] Tyree, M. T.; Zimmermann, M. H. Xylem structure and the ascent of sap in: *Wood Sciences*; Springer: Heidelberg, 2002.

[47] Das, A.; Rangaraj, N.; Sonti, R. V. Multiple adhesin-like functions of *Xanthomonas oryzae* pv. *oryzae* are involved in promoting leaf attachment, entry, and virulence on Rice. *Mol. Plant-Microbe Interact.* **2009**. *22*, 73–85. DOI: 10.1094/MPMI-22-1-0073.

[48] Paauw, M.; van Hulten, M.; Chatterjee, S.; Berg, J. A.; Taks, N. W.; Giesbers, M.; Richard, M. M. S.; van den Burg, H. A. Hydathode immunity protects the Arabidopsis leaf vasculature against colonization by bacterial pathogens. *Curr. Biol.* **2023**. *33*, 697–710.e6. DOI: 10.1016/j.cub.2023.01.013.

[49] Cerutti, A.; Jauneau, A.; Auriac, M.-C.; Lauber, E.; Martinez, Y.; Chiarenza, S.; Leonhardt, N.; Berthomé, R.; Noël, L. D. Immunity at cauliflower hydathodes controls systemic infection by *Xanthomonas campestris* pv *campestris*. *Plant Physiol.* **2017**. *174*, 700–716. DOI: 10.1104/pp.16.01852.

[50] Redzich, L.; Arra, Y.; Loo, E.; Frommer, W. B. Restricted transmission of *Xanthomonas oryzae pv. oryzae* from rice roots to shoots detected by a rapid root infection system. 2025. DOI: 10.1101/2025.08.13.670017.

[51] Rajeshwari, R.; Jha, G.; Sonti, R. V. Role of an *in planta*-expressed xylanase of *Xanthomonas oryzae pv. oryzae* in promoting virulence on rice. *Mol. Plant-Microbe Interact.* **2005**. *18*, 830–837. DOI: 10.1094/MPMI-18-0830.

[52] Kharadi, R. R.; Sundin, G. W. Dissecting the process of xylem colonization through biofilm formation in *Erwinia amylovora*. *J. Plant Pathol.* **2020**, DOI: 10.1007/s42161-020-00635-x.

[53] Dsouza, F. P.; Dinesh, S.; Sharma, S. Understanding the intricacies of microbial biofilm formation and its endurance in chronic infections: a key to advancing biofilm-targeted therapeutic strategies. *Arch. Microbiol.* **2024**. *206*, 85. DOI: 10.1007/s00203-023-03802-7.

[54] Valentini, M.; Filloux, A. Biofilms and cyclic di-GMP (c-di-GMP) signaling: lessons from *Pseudomonas aeruginosa* and other bacteria. *J. Biol. Chem.* **2016**. *291*, 12547. DOI: 10.1074/jbc.R115.711507.

[55] Malinowski, R.; Singh, D.; Kasprzewska, A.; Blicharz, S.; Basińska-Barczak, A. Vascular tissue – boon or bane? How pathogens usurp long-distance transport in plants and the defence mechanisms deployed to counteract them. *New Phytol.* **2024**. *243*, 2075–2092. DOI: 10.1111/nph.20030.

[56] Roussin-Léveillée, C.; Lajeunesse, G.; St-Amand, M.; Veerapen, V. P.; Silva-Martins, G.; Nomura, K.; Brassard, S.; Bolaji, A.; He, S. Y.; Moffett, P. Evolutionarily conserved bacterial effectors hijack abscisic acid signaling to induce an aqueous environment in the apoplast. *Cell Host Microbe* **2022**. *30*, 489–501.e4. DOI: 10.1016/j.chom.2022.02.006.

[57] Pousti, M.; Pouyan Zarabadi, M.; Amirdehi, M. A.; Paquet-Mercier, F.; Greener, J. Microfluidic bioanalytical flow cells for biofilm studies: a review. *Analyst* **2019**. *144*, 68–86. DOI: 10.1039/C8AN01526K.

[58] Luneau, J. S.; Cerutti, A.; Roux, B.; Carrère, S.; Jardinaud, M.-F.; Gaillac, A.; Gris, C.; Lauber, E.; Berthomé, R.; Arlat, M.; Boulanger, A.; Noël, L. D. *Xanthomonas* transcriptome inside cauliflower hydathodes reveals bacterial virulence strategies and physiological adaptation at early infection stages. *Mol. Plant Pathol.* **2022**. *23*, 159–174. DOI: 10.1111/mpp.13117.

[59] Chu, L. T.; Laxman, D.; Abdelhamed, J.; Pirlo, R. K.; Fan, F.; Wagner, N.; Tran, T. M.; Bui, L. Development of a tomato xylem-mimicking microfluidic system to study *Ralstonia pseudosolanacearum* biofilm formation. *Front. Bioeng. Biotechnol.* **2024**. *12*, 1395959. DOI: 10.3389/fbioe.2024.1395959.

[60] Monteiro, M. P.; Hernandez-Montelongo, J.; Sahoo, P. K.; Hernández Montelongo, R.; de Oliveira, D. S.; Piazzeta, M. H.; García Sandoval, J. P.; de Souza, A. A.; Gobbi, A. L.; Cotta, M. A. Functionalized microchannels as xylem-mimicking environment: Quantifying *X. fastidiosa* cell adhesion. *Biophys. J.* **2021**. *120*, 1443–1453. DOI: 10.1016/j.bpj.2021.02.009.

[61] Meng, Y.; Li, Y.; Galvani, C. D.; Hao, G.; Turner, J. N.; Burr, T. J.; Hoch, H. C. Upstream migration of *Xylella fastidiosa* via pilus-driven twitching motility. *J. Bacteriol.* **2005**. *187*, 5560. DOI: 10.1128/JB.187.16.5560-5567.2005.

[62] De La Fuente, L.; Montanes, E.; Meng, Y.; Li, Y.; Burr, T. J.; Hoch, H. C.; Wu, M. Assessing adhesion forces of type I and type IV pili of *Xylella fastidiosa* bacteria by use of a microfluidic flow chamber. *Appl. Environ. Microbiol.* **2007**. *73*, 2690–2696. DOI: 10.1128/AEM.02649-06.

[63] Shen, Y.; Chern, M.-s.; Silva, F. G.; Ronald, P. Isolation of a *Xanthomonas oryzae* pv. *oryzae* flagellar operon region and molecular characterization of *flhF*. *Mol. Plant-Microbe Interact.* **2001**. *14*, 204–213. DOI: 10.1094/MPMI.2001.14.2.204.

[64] Feng, T.-Y.; Guo, T.-T. Bacterial leaf blight of rice plant VI: Chemotactic responses of *Xanthomonas oryzae* to water droplets exudated from water pores on the leaf of rice plants. *Bot. Bull. Acad. Sin.* **1975**. *16*, 126–136.

[65] Cogan, N. G.; Donahue, M. R.; Whidden, M.; De La Fuente, L. Pattern formation exhibited by biofilm formation within microfluidic chambers. *Biophysical Journal* **2013**. *104*, 1867–1874. DOI: 10.1016/j.bpj.2013.03.037.

[66] Tokárová, V.; Sudalaiyadum Perumal, A.; Nayak, M.; Shum, H.; Kašpar, O.; Rajendran, K.; Mohammadi, M.; Tremblay, C.; Gaffney, E. A.; Martel, S.; Nicolau, D. V.; Nicolau, D. V. Patterns of bacterial motility in microfluidics-confining environments. *Proc. Natl. Acad. Sci.* **2021**. *118*, e2013925118. DOI: 10.1073/pnas.2013925118.

[67] Elert, E. Rice by the numbers: A good grain. *Nature* **2014**. *514*, DOI: 10.1038/514S50a.

[68] Savary, S.; Willocquet, L.; Pethybridge, S. J.; Esker, P.; McRoberts, N.; Nelson, A. The global burden of pathogens and pests on major food crops. *Nat. Ecol. Evol.* **2019**. *3*, 430–439. DOI: 10.1038/s41559-018-0793-y.

[69] Oliva, R.; Ji, C.; Atienza-Grande, G.; Huguet-Tapia, J. C.; Perez-Quintero, A.; Li, T.; Eom, J.-S.; Li, C.; Nguyen, H.; Liu, B.; Auguy, F.; Sciallano, C.; Luu, V. T.; Dossa, G. S.; Cunnac, S.; Schmidt, S. M.; Slamet-Loedin, I. H.; Vera Cruz, C.; Szurek, B.; Frommer, W. B.; White, F. F.; Yang, B. Broad-spectrum resistance to bacterial blight in rice using genome editing. *Nat. Biotechnol.* **2019**. *37*, 1344–1350. DOI: 10.1038/s41587-019-0267-z.

[70] Li, K.; Wu, G.; Liao, Y.; Zeng, Q.; Wang, H.; Liu, F. RpoN1 and RpoN2 play different regulatory roles in virulence traits, flagellar biosynthesis, and basal metabolism in *Xanthomonas campestris*. *Mol. Plant Pathol.* **2020**. *21*, 907–922. DOI: 10.1111/mpp.12938.

[71] Yang, F.; Xue, D.; Tian, F.; Hutchins, W.; Yang, C.-H.; He, C. Identification of c-di-GMP signaling components in *Xanthomonas oryzae* and their orthologs in *Xanthomonads* involved in regulation of bacterial virulence expression. *Front. Microbiol.* **2019**. *10*, DOI: 10.3389/fmicb.2019.01402.

[72] Lu, X.-H.; An, S.-Q.; Tang, D.-J.; McCarthy, Y.; Tang, J.-L.; Dow, J. M.; Ryan, R. P. RsmA regulates biofilm formation in *Xanthomonas campestris* through a regulatory network involving cyclic di-GMP and the Clp transcription factor. *PLoS ONE* **2012**. *7*, DOI: 10.1371/journal.pone.0052646.

[73] Yu, C.; Nguyen, D.-P.; Yang, F.; Shi, J.; Wei, Y.; Tian, F.; Zhao, X.; Chen, H. Transcriptome analysis revealed overlapping and special regulatory roles of RpoN1 and RpoN2 in motility, virulence, and growth of *Xanthomonas oryzae pv. oryzae*. *Front. Microbiol.* **2021**. *12*, DOI: 10.3389/fmicb.2021.653354.

[74] De La Fuente, L.; Merfa, M. V.; Cobine, P. A.; Coleman, J. J. Pathogen adaptation to the xylem environment. *Annu. Rev. Phytopathol.* **2022**. *60*, 163–186. DOI: 10.1146/annurev-phyto-021021-041716.

[75] Rooney, L. M.; Amos, W. B.; Hoskisson, P. A.; McConnell, G. Intra-colony channels in *E. coli* function as a nutrient uptake system. *ISME J.* **2020**. *14*, 2461–2473. DOI: 10.1038/s41396-020-0700-9.

[76] Hamilton, C. D.; Steidl, O. R.; MacIntyre, A. M.; Hendrich, C. G.; Allen, C. *Ralstonia solanacearum* depends on catabolism of myo-inositol, sucrose, and trehalose for virulence in an infection stage–dependent manner. *Mol. Plant-Microbe Interact.* **2021**. *34*, 669–679. DOI: 10.1094/MPMI-10-20-0298-R.

[77] Jacobs, J. M.; Babujee, L.; Meng, F.; Milling, A.; Allen, C. The *in planta* transcriptome of *Ralstonia solanacearum*: conserved physiological and virulence strategies during bacterial wilt of tomato. *mBio* **2012**. *3*, DOI: 10.1128/mBio.00114-12.

[78] Noda, T.; Kaku, H. Growth of *Xanthomonas oryzae pv. oryzae in planta* and in guttation fluid of rice. *Jpn. J. Phytopathol.* **1999**. *65*, 9–14. DOI: 10.3186/jjphytopath.65.9.

[79] Fuhrer, T.; Fischer, E.; Sauer, U. Experimental identification and quantification of glucose metabolism in seven bacterial species. *J. Bacteriol.* **2005**. *187*, 1581–1590. DOI: 10.1128/JB.187.5.1581-1590.2005.

[80] Koduru, L.; Kim, H. Y.; Lakshmanan, M.; Mohanty, B.; Lee, Y. Q.; Lee, C. H.; Lee, D.-Y. Genome-scale metabolic reconstruction and *in silico* analysis of the rice leaf blight pathogen, *Xanthomonas oryzae*. *Mol. Plant Pathol.* **2020**. *21*, 527–540. DOI: 10.1111/mpp.12914.

[81] Chandran, D. Co-option of developmentally regulated plant SWEET transporters for pathogen nutrition and abiotic stress tolerance. *IUBMB Life* **2015**. *67*, 461–471. DOI: 10.1002/iub.1394.

[82] Zhou, J.; Peng, Z.; Long, J.; Sosso, D.; Liu, B.; Eom, J.-S.; Huang, S.; Liu, S.; Vera Cruz, C.; Frommer, W. B.; White, F. F.; Yang, B. Gene targeting by the TAL effector PthXo2 reveals cryptic resistance gene for bacterial blight of rice. *Plant J.* **2015**. *82*, 632–643. DOI: 10.1111/tpj.12838.

[83] Eom, J.-S.; Luo, D.; Atienza-Grande, G.; Yang, J.; Ji, C.; Thi Luu, V.; Huguet-Tapia, J. C.; Char, S. N.; Liu, B.; Nguyen, H.; Schmidt, S. M.; Szurek, B.; Vera Cruz, C.; White, F. F.; Oliva, R.; Yang, B.; Frommer, W. B. Diagnostic kit for rice blight resistance. *Nat. Biotechnol.* **2019**. *37*, 1372–1379. DOI: 10.1038/s41587-019-0268-y.

[84] Cohn, M.; Bart, R. S.; Shybut, M.; Dahlbeck, D.; Gomez, M.; Morbitzer, R.; Hou, B.-H.; Frommer, W. B.; Lahaye, T.; Staskawicz, B. J. *Xanthomonas axonopodis* virulence is promoted by a transcription activator-like effector–mediated induction of a *SWEET sugar transporter* in cassava. *Mol. Plant-Microbe Interact.* **2014**. *27*, 1186–1198. DOI: 10.1094/MPMI-06-14-0161-R.

[85] Ausubel, F. M. Current protocols in molecular biology. *Wiley* **1987**.

[86] Jayakody, L. N.; Johnson, C. W.; Whitham, J. M.; Giannone, R. J.; Black, B. A.; Cleveland, N. S.; Klingeman, D. M.; Michener, W. E.; Olstad, J. L.; Vardon, D. R.; Brown, R. C.; Brown, S. D.; Hettich, R. L.; Guss, A. M.; Beckham, G. T. Correction: Thermochemical wastewater valorization via enhanced microbial toxicity tolerance. *Energy Environ. Sci.* **2021**. *14*, 6678–6678. DOI: 10.1039/D1EE90066H.

[87] Livak, K. J.; Schmittgen, T. D. Analysis of relative gene expression data using real-time quantitative PCR and the 2(-Delta Delta C(T)) Method. *Methods* **2001**. *25*, 402–408. DOI: 10.1006/meth.2001.1262.

[88] Kauffman, H. E.; Reddy, A. P. K.; Hsieh, S. P. Y.; Merca, S. D.; Kauffman, H. E.; Reddy, A. P. K.; Hsieh, S. P. Y.; Merca, S. D. An improved technique for evaluating resistance of rice varieties to *Xanthomonas oryzae*. *Plant Dis. Rep.* **1973**. *57*, 537–541.

[89] Lemoine, F.; Correia, D.; Lefort, V.; Doppelt-Azeroual, O.; Mareuil, F.; Cohen-Boulakia, S.; Gascuel, O. NGPhylogeny.fr: new generation phylogenetic services for non-specialists. *Nucleic Acids Res.* **2019**. *47*, W260–W265. DOI: 10.1093/nar/gkz303.

[90] Alberto, F.; Jordi, E.; Henrissat, B.; Czjzek, M. Crystal structure of inactivated *Thermotoga maritima* invertase in complex with the trisaccharide substrate raffinose. *Biochem. J.* **2006**. *395*, 457–462. DOI: 10.1042/BJ20051936.

[91] Kim, M.-I.; Kim, H.-S.; Jung, J.; Rhee, S. Crystal structures and mutagenesis of sucrose hydrolase from *Xanthomonas axonopodis pv. glycines*: Insight into the exclusively hydrolytic amylosucrase fold. *J. Mol. Biol.* **2008**. *380*, 636–647. DOI: 10.1016/j.jmb.2008.05.046.

[92] Kroll, A.; Rousset, Y.; Hu, X.-P.; Liebrand, N. A.; Lercher, M. J. Turnover number predictions for kinetically uncharacterized enzymes using machine and deep learning. *Nat. Commun.* **2023**. *14*, 4139. DOI: 10.1038/s41467-023-39840-4.

[93] Paysan-Lafosse, T.; Blum, M.; Chuguransky, S.; Grego, T.; Pinto, B. L.; Salazar, G. A.; Bileschi, M. L.; Bork, P.; Bridge, A.; Colwell, L.; Gough, J.; Haft, D. H.; Letunić, I.; Marchler-Bauer, A.; Mi, H.; Natale, D. A.; Orengo, C. A.; Pandurangan, A. P.; Rivoire, C.; Sigrist, C. J. A.; Sillitoe, I.; Thanki, N.; Thomas, P. D.; Tosatto, S. C. E.; Wu, C. H.; Bateman, A. InterPro in 2022. *Nucleic Acids Res.* **2023**. *51*, 418–427. DOI: 10.1093/nar/gkac993.

[94] Novichkov, P. S.; Kazakov, A. E.; Ravcheev, D. A.; Leyn, S. A.; Kovaleva, G. Y.; Sutormin, R. A.; Kazanov, M. D.; Riehl, W.; Arkin, A. P.; Dubchak, I.; Rodionov, D. A. RegPrecise 3.0 – A resource for genome-scale exploration of transcriptional regulation in bacteria. *BMC Genomics* **2013**. *14*, 745. DOI: 10.1186/1471-2164-14-745.

[95] Bordes, P.; Wigneshweraraj, S. R.; Zhang, X.; Buck, M. Sigma54-dependent transcription activator phage shock protein F of *Escherichia coli*: a fragmentation approach to identify sequences that contribute to self-association. *Biochem. J.* **2004**. *378*, 735–744. DOI: 10.1042/BJ20031464.

[96] Taylor, M.; Butler, R.; Chambers, S.; Casimiro, M.; Badii, F.; Merrick, M. The RpoN-box motif of the RNA polymerase sigma factor sigma N plays a role in promoter recognition. *Mol. Microbiol.* **1996**. *22*, 1045–1054. DOI: 10.1046/j.1365-2958.1996.01547.x.

[97] Schülein, K.; Schmid, K.; Benzl, R. The sugar-specific outer membrane channel ScrY contains functional characteristics of general diffusion pores and substrate-specific porins. *Mol. Microbiol.* **1991**. *5*, 2233–2241. DOI: 10.1111/j.1365-2958.1991.tb02153.x.

[98] Pollet, R. M.; Foley, M. H.; Kumar, S. S.; Elmore, A.; Jabara, N. T.; Venkatesh, S.; Vasconcelos Pereira, G.; Martens, E. C.; Koropatkin, N. M. Multiple TonB homologs are important for carbohydrate utilization by *Bacteroides thetaiotaomicron*. *J. Bacteriol.* **2023**. *205*, 218–223. DOI: 10.1128/jb.00218-23.

[99] Nirody, J. A.; Sun, Y.-R.; Lo, C.-J. The biophysicist's guide to the bacterial flagellar motor. *Adv. Phys.: X* **2017**. *2*, 324–343. DOI: 10.1080/23746149.2017.1289120.

[100] Davies, G. J.; Wilson, K. S.; Henrissat, B. Nomenclature for sugar-binding subsites in glycosyl hydrolases. *Biochem. J.* **1997**. *321*, 557–559. DOI: 10.1042/bj3210557.

[101] Ke, Y.; Hui, S.; Meng, Y. *Xanthomonas oryzae pv. oryzae* inoculation and growth rate on Rice by leaf clipping method. *bio-protocol* **2017**, DOI: doi.org/10.21769/BioProtoc.2568.

[102] Sun, L.; Yang, D.-l.; Kong, Y.; Chen, Y.; Li, X.-Z.; Zeng, L.-J.; Li, Q.; Wang, E.-T.; He, Z.-H. Sugar homeostasis mediated by cell wall invertase GRAIN INCOMPLETE FILLING 1 (GIF1) plays a role in pre-existing and induced defence in rice. *Mol. Plant Pathol.* **2014**. *15*, 161–173. DOI: 10.1111/mpp.12078.

[103] Kim, J.-S.; Yoon, S.-J.; Park, Y.-J.; Kim, S.-Y.; Ryu, C.-M. Crossing the kingdom border: Human diseases caused by plant pathogens. *Environ. Microbiol.* **2020**. *22*, 2485–2495. DOI: 10.1111/1462-2920.15028.

[104] Cox, K. L.; Meng, F.; Wilkins, K. E.; Li, F.; Wang, P.; Booher, N. J.; Carpenter, S. C. D.; Chen, L.-Q.; Zheng, H.; Gao, X.; Zheng, Y.; Fei, Z.; Yu, J. Z.; Isakeit, T.; Wheeler, T.; Frommer, W. B.; He, P.; Bogdanove, A. J.; Shan, L. TAL effector driven induction of a *SWEET* gene confers susceptibility to bacterial blight of cotton. *Nat. Commun.* **2017**. *8*, 15588. DOI: 10.1038/ncomms15588.

[105] Anderson, J. C.; Wan, Y.; Kim, Y.-M.; Pasa-Tolic, L.; Metz, T. O.; Peck, S. C. Decreased abundance of type III secretion system-inducing signals in Arabidopsis *mkp1* enhances resistance against *Pseudomonas syringae*. *Proc. Natl. Acad. Sci. U.S.A.* **2014**. *111*, 6846–6851. DOI: 10.1073/pnas.1403248111.

[106] Anderson, J. C. Ill communication: Host metabolites as virulence-regulating signals for plant-pathogenic bacteria. *Annu. Rev. Phytopathol.* **2023**. *61*, 49–71. DOI: 10.1146/annurev-phyto-021621-114026.

[107] Jha, G.; Rajeshwari, R.; Sonti, R. V. Functional interplay between two *Xanthomonas oryzae pv. oryzae* secretion systems in modulating virulence on Rice. *Mol. Plant-Microbe Interact.* **2007**. *20*, 31–40. DOI: 10.1094/MPMI-20-0031.

[108] Alvarez-Martinez, C. E.; Sgro, G. G.; Araujo, G. G.; Paiva, M. R. N.; Matsuyama, B. Y.; Guzzo, C. R.; Andrade, M. O.; Farah, C. S. Secrete or perish: The role of secretion systems in *Xanthomonas* biology. *Comput. Struct. Biotechnol. J.* **2021**. *19*, 279–302. DOI: 10.1016/j.csbj.2020.12.020.

[109] Sinha, D.; Gupta, M. K.; Patel, H. K.; Ranjan, A.; Sonti, R. V. Cell wall degrading enzyme induced Rice innate immune responses are suppressed by the type 3 secretion system effectors XopN, XopQ, XopX and XopZ of *Xanthomonas oryzae pv. oryzae*. *PLoS ONE* **2013**. *8*, e75867. DOI: 10.1371/journal.pone.0075867.

[110] Büttner, D.; He, S. Y. Type III protein secretion in plant pathogenic bacteria. *Plant Physiol.* **2009**. *150*, 1656–1664. DOI: 10.1104/pp.109.139089.

[111] Greig, D.; Travisano, M. The prisoner's dilemma and polymorphism in yeast *SUC* genes. *Proc. Natl. Acad. Sci. U.S.A.* **2004**. *271*, S25–S26. DOI: 10.1098/rsbl.2003.0083.

[112] Gore, J.; Youk, H.; van Oudenaarden, A. Snowdrift game dynamics and facultative cheating in yeast. *Nature* **2009**. *459*, 253–256. DOI: 10.1038/nature07921.

[113] Farnham, P. J.; Platt, T. Rho-independent termination: dyad symmetry in DNA causes RNA polymerase to pause during transcription *in vitro*. *Nucleic Acids Res* **1981**. *9*, 563–577. DOI: 10.1093/nar/9.3.563.

[114] Yanofsky, C.; Platt, T.; Crawford, I.; Nichols, B.; Christie, G.; Horowitz, H.; VanCleemput, M.; Wu, A. The complete nucleotide sequence of the tryptophan operon of *Escherichia coli*. *Nucleic Acids Res.* **1981**. *9*, 6647–6668. DOI: 10.1093/nar/9.24.6647.

[115] Studier, F. W. Protein production by auto-induction in high-density shaking cultures. *Protein Expression Purif.* **2005**. *41*, 207–234. DOI: 10.1016/j.pep.2005.01.016.

[116] Yu, N. Y.; Wagner, J. R.; Laird, M. R.; Melli, G.; Rey, S.; Lo, R.; Dao, P.; Sahinalp, S. C.; Ester, M.; Foster, L. J.; Brinkman, F. S. L. PSORTb 3.0: improved protein subcellular localization prediction with refined localization subcategories and predictive capabilities for all prokaryotes. *Bioinformatics* **2010**. *26*, 1608–1615. DOI: 10.1093/bioinformatics/btq249.

[117] Almagro Armenteros, J. J.; Tsirigos, K. D.; Sønderby, C. K.; Petersen, T. N.; Winther, O.; Brunak, S.; von Heijne, G.; Nielsen, H. SignalP 5.0 improves signal peptide predictions using deep neural networks. *Nat. Biotechnol.* **2019**. *37*, 420–423. DOI: 10.1038/s41587-019-0036-z.

[118] Zückert, W. R. Secretion of bacterial lipoproteins: Through the cytoplasmic membrane, the periplasm and beyond. *Biochim. Biophys. Acta. Mol. Cell. Res.* **2014**. *1843*, 1509–1516. DOI: 10.1016/j.bbamcr.2014.04.022.

[119] Lin, Y.; Liao, Y.-Y.; Huang, R.-X.; Li, A.-Z.; An, S.-Q.; Tang, J.-L.; Tang, D.-J. Extracellular amylase is required for full virulence and regulated by the global posttranscriptional regulator RsmA in *Xanthomonas campestris pv. campestris*. *Phyto* **2021**. *111*, DOI: 10.1094/PHYTO-08-20-0372-R.

[120] Ray, S. K.; Rajeshwari, R.; Sonti, R. V. Mutants of *Xanthomonas oryzae pv. oryzae* deficient in general secretory pathway are virulence deficient and unable to secrete xylanase. *Mol. Plant-Microbe Interact.* **2000**. *13*, 394–401. DOI: 10.1094/MPMI.2000.13.4.394.

[121] Carlson, M.; Botstein, D. Two differentially regulated mRNAs with different 5 ends encode secreted and intracellular forms of yeast invertase. *Cell* **1982**. *28*, 145–154. DOI: 10.1016/0092-8674(82)90384-1.

[122] Perlman, D.; Raney, P.; Halvorson, H. O. Cytoplasmic and secreted *Saccharomyces cerevisiae* invertase mRNAs encoded by one gene can be differentially or coordinately regulated. *Mol. Cell. Biol.* **1984**. *4*, 1682–1688.

[123] Crooks, G. E.; Hon, G.; Chandonia, J.-M.; Brenner, S. E. WebLogo: a sequence logo generator. *Genome Res.* **2004**. *14*, 1188–1190. DOI: 10.1101/gr.849004.

[124] Padan, E.; Bibi, E.; Ito, M.; Krulwich, T. A. Alkaline pH homeostasis in bacteria: New insights. *Biochim. Biophys. Acta. Biomem.* **2005**. *1717*, 67–88. DOI: 10.1016/j.bbamem.2005.09.010.

[125] Fukumorita, T.; Chino, M. Sugar, amino acid and inorganic contents in rice phloem sap. *Plant Cell Physiol.* **1982**. *23*, 273–283. DOI: 10.1093/oxfordjournals.pcp.a076347.

[126] Mitani, N.; Ma, J. F.; Iwashita, T. Identification of the silicon form in xylem sap of Rice (*Oryza sativa L.*) *Plant Cell Physiol.* **2005**. *46*, 279–283. DOI: 10.1093/pcp/pci018.

[127] Singh, S.; Datta, S.; Narayanan, K. B.; Rajnish, K. N. Bacterial exo polysaccharides in biofilms: role in antimicrobial resistance and treatments. *J. Genet. Eng. Biotechnol.* **2021**. *19*, 140. DOI: 10.1186/s43141-021-00242-y.

[128] Henkin, T. M. Posttranscriptional regulation in: *Encyclopedia of Microbiology*; Academic Press: Oxford, 2009.

[129] Chopra, P.; Bender, A. *A quantitative bgl operon model for E. coli requires BglF conformational change for sugar transport*. Springer: 2008, pp 1–22. DOI: 10.1007/978-3-540-88765-2_1.

[130] Wang, L.; Wessler, S. R. Role of mRNA secondary structure in translational repression of the Maize transcriptional activator *Lc*. *Plant Physiol.* **2001**. *125*, 1380–1387.

[131] Kozak, M. Downstream secondary structure facilitates recognition of initiator codons by eukaryotic ribosomes. *Proc. Natl. Acad. Sci. U.S.A.* **1990**. *87*, 8301–8305. DOI: 10.1073/pnas.87.21.8301.

[132] Giegé, P.; Heazlewood, J. L.; Roessner-Tunali, U.; Millar, A. H.; Fernie, A. R.; Leaver, C. J.; Sweetlove, L. J. Enzymes of glycolysis are functionally associated with the mitochondrion in Arabidopsis cells. *Plant Cell* **2003**. *15*, 2140–2151. DOI: 10.1105/tpc.012500.

[133] Plaxton, W. C. The organization and regulation of plant glycolysis. *Annu. Rev. Plant Physiol. Plant Mol. Biol.* **1996**. *47*, 185–214. DOI: 10.1146/annurev.arplant.47.1.185.

[134] Entian, K. D.; Barnett, J. A. Regulation of sugar utilization by *Saccharomyces cerevisiae*. *Trends Biochem. Sci* **1992**. *17*, DOI: 10.1016/0968-0004(92)90341-6.

[135] Carlson, M.; Taussig, R.; Kustu, S.; Botstein, D. The secreted form of invertase in *Saccharomyces cerevisiae* is synthesized from mRNA encoding a signal sequence. *Mol. Cell. Biol.* **1983**. *3*, 439–447. DOI: 10.1128/mcb.3.3.439-447.1983.

[136] West, S. A.; Diggle, S. P.; Buckling, A.; Gardner, A.; Griffin, A. S. The social lives of microbes. *Annu. Rev. Ecol. Evol. Syst.* **2007**. *38*, 53–77. DOI: 10.1146/annurev.ecolsys.38.091206.095740.

[137] Yu, C.; Chen, H.; Tian, F.; Yang, F.; Yuan, X.; Yang, C.-H.; He, C. A ten gene-containing genomic island determines flagellin glycosylation: implication for its regulatory role in motility and virulence of *Xanthomonas oryzae pv. oryzae*. *Mol. Plant Pathol.* **2018**. *19*, 579–592. DOI: 10.1111/mpp.12543.

[138] Witting, L.; Seiffarth, J.; Stute, B.; Schulze, T.; Hofer, J. M.; Nöh, K.; Eisenhut, M.; Weber, A. P. M.; Lieres, E. v.; Kohlheyer, D. A microfluidic system for the cultivation of cyanobacteria with precise light intensity and CO2 control: enabling growth data acquisition at single-cell resolution. *Lab Chip* **2025**. *25*, 319–329. DOI: 10.1039/D4LC00567H.

[139] Lewis, A. M.; Boose, E. R. Estimating volume flow rates through xylem conduits. *Am. J. Bot.* **1995**. *82*, 1112–1116. DOI: 10.1002/j.1537-2197.1995.tb11581.x.

[140] Jarrell, K. F.; McBride, M. J. The surprisingly diverse ways that prokaryotes move. *Nat. Rev. Microbiol.* **2008**. *6*, 466–476. DOI: 10.1038/nrmicro1900.

[141] Shen, Y.; Ronald, P. Molecular determinants of disease and resistance in interactions of *Xanthomonas oryzae pv. oryzae* and rice. *Microbes and Infection* **2002**. *4*, 1361–1367. DOI: 10.1016/S1286-4579(02)00004-7.

[142] Dai, X.; Wang, Y.; Yu, K.; Zhao, Y.; Xiong, L.; Wang, R.; Li, S. OsNPR1 enhances rice resistance to *Xanthomonas oryzae pv. oryzae* by upregulating rice defense genes and repressing bacteria virulence genes. *Int. J. Mol. Sci.* **2023**. *24*, 8687. DOI: 10.3390/ijms24108687.

[143] Westermann, A. J.; Gorski, S. A.; Vogel, J. Dual RNA-seq of pathogen and host. *Nat Rev Microbiol* **2012**. *10*, 618–630. DOI: 10.1038/nrmicro2852.

[144] Westermann, A. J.; Barquist, L.; Vogel, J. Resolving host–pathogen interactions by dual RNA-seq. *PLoS Pathog* **2017**. *13*, e1006033. DOI: 10.1371/journal.ppat.1006033.

[145] Liao, Z.-X.; Ni, Z.; Wei, X.-L.; Chen, L.; Li, J.-Y.; Yu, Y.-H.; Jiang, W.; Jiang, B.-L.; He, Y.-Q.; Huang, S. Dual RNA-seq of *Xanthomonas oryzae pv. oryzicola* infecting rice reveals novel insights into bacterial-plant interaction. *PLoS ONE* **2019**. *14*, e0215039. DOI: 10.1371/journal.pone.0215039.

[146] Schmidtke, C.; Findeiss, S.; Sharma, C. M.; Kuhfuss, J.; Hoffmann, S.; Vogel, J.; Stadler, P. F.; Bonas, U. Genome-wide transcriptome analysis of the plant pathogen Xanthomonas identifies sRNAs with putative virulence functions. *Nucleic Acids Res* **2012**. *40*, 2020–2031. DOI: 10.1093/nar/gkr904.

[147] Li, T.; Huang, S.; Zhou, J.; Yang, B. Designer TAL effectors induce disease susceptibility and resistance to *Xanthomonas oryzae pv. oryzae* in rice. *Mol. Plant* **2013**. *6*, 781–789. DOI: 10.1093/mp/sst034.

[148] Deuschle, K.; Okumoto, S.; Fehr, M.; Looger, L. L.; Kozhukh, L.; Frommer, W. B. Construction and optimization of a family of genetically encoded metabolite sensors by semirational protein engineering. *Protein Sci.* **2005**. *14*, 2304–2314. DOI: 10.1110/ps.051508105.

[149] Fehr, M.; Lalonde, S.; Lager, I.; Wolff, M. W.; Frommer, W. B. Imaging of the dynamics of glucose uptake in the cytosol of COS-7 cells by fluorescent nanosensors. *J. Biol. Chem.* **2003**. *278*, 19127–19133. DOI: 10.1074/jbc.M301333200.

[150] Fehr, M.; Frommer, W. B.; Lalonde, S. Visualization of maltose uptake in living yeast cells by fluorescent nanosensors. *Proc. Natl. Acad. Sci. U.S.A.* **2002**. *99*, 9846–9851. DOI: 10.1073/pnas.142089199.

[151] Lager, I.; Looger, L. L.; Hilpert, M.; Lalonde, S.; Frommer, W. B. Conversion of a putative *Agrobacterium* sugar-binding protein into a FRET sensor with high selectivity for sucrose. *J. Biol. Chem.* **2006**. *281*, 30875–30883. DOI: 10.1074/jbc.M605257200.

[152] Bermejo, C.; Haerizadeh, F.; Takanaga, H.; Chermak, D.; Frommer, W. B. Optical sensors for measuring dynamic changes of cytosolic metabolite levels in yeast. *Nat. Protoc.* **2011**. *6*, 1806–1817. DOI: 10.1038/nprot.2011.391.

[153] Chaudhuri, B.; Hörmann, F.; Frommer, W. B. Dynamic imaging of glucose flux impedance using FRET sensors in wild-type Arabidopsis plants. *J. Exp. Bot.* **2011**. *62*, 2411–2417. DOI: 10.1093/jxb/erq444.

[154] Chaudhuri, B.; Hörmann, F.; Lalonde, S.; Brady, S. M.; Orlando, D. A.; Benfey, P.; Frommer, W. B. Protonophore- and pH-insensitive glucose and sucrose accumulation detected by FRET nanosensors in Arabidopsis root tips. *Plant J.* **2008**. *56*, 948–962. DOI: 10.1111/j.1365-313X.2008.03652.x.

[155] Deuschle, K.; Chaudhuri, B.; Okumoto, S.; Lager, I.; Lalonde, S.; Frommer, W. B. Rapid metabolism of glucose detected with FRET glucose nanosensors in epidermal cells and intact roots of Arabidopsis RNA-silencing mutants. *Plant Cell* **2006**. *18*, 2314–2325. DOI: 10.1105/tpc.106.044073.

[156] Kaper, T.; Lager, I.; Looger, L. L.; Chermak, D.; Frommer, W. B. Fluorescence resonance energy transfer sensors for quantitative monitoring of pentose and disaccharide accumulation in bacteria. *Biotechnol. Biofuels* **2008**. *1*, 11. DOI: 10.1186/1754-6834-1-11.

[157] Bermejo, C.; Haerizadeh, F.; Sadoine, M. S. C.; Chermak, D.; Frommer, W. B. Differential regulation of glucose transport activity in yeast by specific cAMP signatures. *Biochemical Journal* **2013**. *452*, 489–497. DOI: 10.1042/BJ20121736.

[158] Bermejo, C.; Ewald, J. C.; Lanquar, V.; Jones, A. M.; Frommer, W. B. *In vivo* biochemistry: quantifying ion and metabolite levels in individual cells or cultures of yeast. *Biochem J.* **2011**. *438*, 1–10. DOI: 10.1042/BJ20110428.

[159] Takanaga, H.; Chaudhuri, B.; Frommer, W. B. GLUT1 and GLUT9 as major contributors to glucose influx in HepG2 cells identified by a high sensitivity intramolecular FRET glucose sensor. *Biochim. Biophys. Act.* **2008**. *1778*, 1091–1099. DOI: 10.1016/j.bbamem.2007.11.015.

[160] Baird, G. S.; Zacharias, D. A.; Tsien, R. Y. Circular permutation and receptor insertion within green fluorescent proteins. *Proc. Natl. Acad. Sci. U.S.A.* **1999**. *96*, 11241–11246. DOI: 10.1073/pnas.96.20.11241.

[161] Ast, C.; Foret, J.; Oltrogge, L. M.; De Michele, R.; Kleist, T. J.; Ho, C.-H.; Frommer, W. B. Ratiometric matryoshka biosensors from a nested cassette of green- and orange-emitting fluorescent proteins. *Nat. Commun.* **2017**. *8*, 431. DOI: 10.1038/s41467-017-00400-2.

[162] Ast, C.; De Michele, R.; Kumke, M. U.; Frommer, W. B. Single-fluorophore membrane transport activity sensors with dual-emission read-out. *eLife* **2015**. *4*, DOI: 10.7554/eLife.07113.

[163] Ejike, J. O.; Sadoine, M.; Shen, Y.; Ishikawa, Y.; Sunal, E.; Hänsch, S.; Hamacher, A. B.; Frommer, W. B.; Wudick, M. M.; Campbell, R. E.; Kleist, T. J. A monochromatically excitable green–red dual-fluorophore fusion incorporating a new large stokes shift fluorescent protein. *Biochemistry* **2024**. *63*, 171–180. DOI: 10.1021/acs.biochem.3c00451.

[164] Keller, J. P.; Marvin, J. S.; Lacin, H.; Lemon, W. C.; Shea, J.; Kim, S.; Lee, R. T.; Koyama, M.; Keller, P. J.; Looger, L. L. *In vivo* glucose imaging in multiple model organisms with an engineered single-wavelength sensor. *Cell Reports* **2021**. *35*, 109284. DOI: 10.1016/j.celrep.2021.109284.

[165] Cuneo, M. J.; Beese, L. S.; Hellinga, H. W. Structural analysis of semi-specific oligosaccharide recognition by a cellulose-binding protein of *Thermotoga maritima* reveals adaptations for functional diversification of the oligopeptide periplasmic binding protein fold. *J. Biol. Chem.* **2009**. *284*, 33217–33223. DOI: 10.1074/jbc.M109.041624.

[166] Peragine, A.; Yoshikawa, M.; Wu, G.; Albrecht, H. L.; Poethig, R. S. SGS3 and SGS2/SDE1/RDR6 are required for juvenile development and the production of trans-acting siRNAs in Arabidopsis. *Genes. Dev.* **2004**. *18*, 2368–2379. DOI: 10.1101/gad.1231804.

[167] Rowe, J. H.; Jones, A. M. Focus on biosensors: Looking through the lens of quantitative biology. *Quant. Plant Biol.* **2021**. *2*, e12. DOI: 10.1017/qpb.2021.10.

[168] De Michele, R.; Ast, C.; Loqué, D.; Ho, C.-H.; Andrade, S. L.; Lanquar, V.; Grossmann, G.; Gehne, S.; Kumke, M. U.; Frommer, W. B. Fluorescent sensors reporting the activity of ammonium transceptors in live cells. *elife* **2013**. *2*, e00800. DOI: 10.7554/eLife.00800.

[169] Barratt, D. H. P.; Derbyshire, P.; Findlay, K.; Pike, M.; Wellner, N.; Lunn, J.; Feil, R.; Simpson, C.; Maule, A. J.; Smith, A. M. Normal growth of Arabidopsis requires cytosolic invertase but not sucrose synthase. **2009**. *106*, 13124–13129. DOI: 10.1073/pnas.0900689106.

[170] Stadler, R.; Wright, K. M.; Lauterbach, C.; Amon, G.; Gahrtz, M.; Feuerstein, A.; Oparka, K. J.; Sauer, N. Expression of GFP-fusions in Arabidopsis companion cells reveals non-specific protein trafficking into sieve elements and identifies a novel post-phloem domain in roots. *Plant J.* **2005**. *41*, 319–331. DOI: 10.1111/j.1365-313X.2004.02298.x.

[171] Wright, K. M.; Oparka, K. J. Metabolic inhibitors induce symplastic movement of solutes from the transport phloem of Arabidopsis roots. *J. Exp. Bot.* **1997**.

[172] Zöllner, N. R.; Bezrutczyk, M.; Laureyns, R.; Nelissen, H.; Simon, R.; Frommer, W. B. An RNA *in situ* hybridization protocol optimized for monocot tissue. *STAR Protocols* **2021**. *2*, 100398. DOI: 10.1016/j.xpro.2021.100398.

[173] Bezrutczyk, M.; Zöllner, N. R.; Kruse, C. P. S.; Hartwig, T.; Lautwein, T.; Köhrer, K.; Frommer, W. B.; Kim, J.-Y. Evidence for phloem loading via the abaxial bundle sheath cells in maize leaves. *Plant Cell* **2021**, koaa055. DOI: 10.1093/plcell/koaa055.

[174] Kim, J.-Y.; Symeonidi, E.; Pang, T. Y.; Denyer, T.; Weidauer, D.; Bezrutczyk, M.; Miras, M.; Zöllner, N.; Hartwig, T.; Wudick, M. M.; Lercher, M.; Chen, L.-Q.; Timmermans, M. C. P.; Frommer, W. B. Distinct identities of leaf phloem cells revealed by single cell transcriptomics. *The Plant Cell* **2021**, koaa060. DOI: 10.1093/plcell/koaa060.

Appendix

A. Supervision of B.Sc. and M.Sc. students

- Kajetan Linkert, B.Sc. (2022) Characterization of the infection of rice leaves by *Xanthomonas oryzae pv. oryzae*
- Alexa Ackermann and Sabrina Egli, Master-Module (2022) Fluorescent Biosensor Engineering: Principles & Strategies
- Sabrina Egli, Master-Internship (ITILS) (2023) Investigation of the effect of carbon sources on the growth of *Xoo* and *Xoc*
- Farah Nawaf, Master-Internship (ITILS) (2024) Swimming and swarming motility of *Xoo* in dependence on sugar availability
- Paula Semler, B.Sc. (2025) Characterization of the role of a sucrase from *Xanthomonas oryzae pv. oryzae* in sucrose utilization
- Seminar for *in silico* cloning in Master-Module (2023, 2024 and 2025)

B. Current publications and manuscripts

- A critical role of *sux* cistron-mediated sucrose uptake for virulence of the rice blight pathogen *Xanthomonas oryzae pv. oryzae*
  Nora R. Zöllner, Juying Long, Congfeng Song, Jacob Sharkey, Michael M. Wudick, Eliza P.I. Loo, Mayuri Sadoine, Violetta Applegate, Astrid Höppner, Sander H.J. Smits, Bing Yang and Wolf B. Frommer [41]
- Evidence for rapid hydrolysis of shoot-derived sucrose using an ultrasensitive ratiometric Matryoshka-type MGlucoMeter sensor
  Yuuma Ishikawa, **Nora R. Zöllner**, and Wolf B. Frommer, *in preparation*
- Ratiometric Matryoshka MsucMeter sensors for sucrose
  Athanasios Papadopoulos, Jens Reiners, **Nora R. Zöllner**, Laura Redzich, Mayuri Sadoine, Christoph G. W. Gertzen, Tom Berwanger, Kerstin Schipper, Manuel Anlauf, Stefanie Weidtkamp-Peters, Wolf B. Frommer, and Sander H. J. Smits, *in preparation*
- Sucrose uptake and metabolism in *Xanthomonas oryzae pv. oryzae* via dual-localized sucrose hydrolase
  Nora R. Zöllner, Jacob Sharkey and Wolf B. Frommer, *in preparation*
- An RNA *in situ* hybridization protocol optimized for monocot tissue
  Nora R. Zöllner, Margaret Bezrutczyk, Reinout Laureyns, Hilde Nelissen, Rüdiger Simon and Wolf B. Frommer [172]
- Evidence for phloem loading via the abaxial bundle sheath cells in maize leaves
  Margaret Bezrutczyk, **Nora R. Zöllner**, Colin P. S. Kruse, Thomas Hartwig, Tobias Lautwein, Karl Köhrer, Wolf B. Frommer and Ji-Yun Kim [173]
- Distinct identities of leaf phloem cells revealed by single cell transcriptomics
  Ji-Yun Kim, Efthymia Symeonidi, Tin Yau Pang, Tom Denyer, Diana Weidauer, Margaret Bezrutczyk, Manuel Miras, **Nora Zöllner**, Thomas Hartwig, Michael M. Wudick, Martin Lercher, Li-Qing Chen, Marja C.P. Timmermans and Wolf B. Frommer [174]

C. Eidesstattliche Erklärung

Ich versichere an Eides Statt, dass die Dissertation von mir selbständig und ohne unzulässige fremde Hilfe unter Beachtung der "Grundsätze zur Sicherung guter wissenschaftlicher Praxis an der Heinrich-Heine-Universität Düsseldorf" erstellt worden ist.